October 2018

PREPARATION, MECHANICS and STRUCTURE of SPHERE PACKINGS Near the RANDOM LOOSE PACKING LIMIT

Greg Robert Farrell
University of Massachusetts Amherst

PREPARATION, MECHANICS AND STRUCTURE OF SPHERE PACKINGS NEAR THE RANDOM LOOSE PACKING LIMIT

A Dissertation Presented

by

GREG ROBERT FARRELL

Submitted to the Graduate School of the
University of Massachusetts Amherst in partial fulfillment
of the requirements for the degree of

DOCTOR OF PHILOSOPHY

September, 2018

Physics

PREPARATION, MECHANICS AND STRUCTURE OF SPHERE PACKINGS NEAR THE RANDOM LOOSE PACKING LIMIT

A Dissertation Presented

by

GREG ROBERT FARRELL

Approved as to style and content by:

Narayanan Menon, Chair

Benny Davidovitch, Member

Anthony Dinsmore, Member

Gregory Grason, Member

Narayanan Menon, Department Chair
Physics

DEDICATION

To my father who, gazing at the stars, loved to pose questions to a wondering child. Herein may you find answers to a few questions you may have asked had we been looking down at the sand and not up at the sky.

ACKNOWLEDGMENTS

The groundwork for experiments described in Chapter 2 was performed by Michael Martini as part of a senior research paper at Amherst High School. We acknowledge funding from the NSF through NSF-DMR 0606216, 0907245, 120778 and 1507650 and the use of facilities funded by NSF-MRSEC 0820506.

ABSTRACT

PREPARATION, MECHANICS AND STRUCTURE OF SPHERE PACKINGS NEAR THE RANDOM LOOSE PACKING LIMIT

SEPTEMBER, 2018

GREG ROBERT FARRELL

B.S., BRANDEIS UNIVERSITY

Ph.D., UNIVERSITY OF MASSACHUSETTS AMHERST

Directed by: Professor Narayanan Menon

Packings of monodisperse, hard spheres serve as an important model system in the understanding of granular materials which are ubiquitous in nature and industry from sedimented river beds, to construction aggregates, to pharmaceuticals. Unlike frictionless hard spheres which are only stable at densities near the random close packing volume fraction, packings of real spheres form stable packings over a range of volume fractions. We report experimental investigations of sedimented packings of noncohesive polymethyl-methacrylate spheres over a range of volume fractions near the lower limit of this range of volume fractions.

We create packings by slow sedimentation in a viscous fluid and find that a limiting low volume fraction is achieved when the Stokes' number drops below ten. This threshold value is consistent with the vanishing of the interparticle restitution coefficient. We observe that the lower limit of packing achieved depends on the type of sphere used. We develop a new *in situ* measurement of the effective interparticle

friction coefficient and find that lower limiting volume fractions are obtained with higher static friction particles. Thus a random loose packing limit (RLP) in which non-cohesive spheres are stabilized by frictional contacts can be achieved by gentle sedimentation and yields volume fractions distinct from random close packing.

We also report experiments on the mechanical response of these sedimented sphere packings. We observe that the yield-stress scales with identical cube-root power-laws of strain-rate and age. We introduce a modification of the Maxwell model of viscoelasticity that accounts for this exponent as well as for mechanical responses that we observe under constant strain and those observed elsewhere under constant stress.

We investigate the internal 3-dimensional structure of sedimented packings using refractive index matching and laser-sheet illumination. Despite these sedimented packings having been deposited in gravity, we find that the structure is isotropic and homogeneous in the bulk. We find spatial autocorrelations and cross-correlations to be short ranged and that the radial distribution function is largely determined by local structure. We report distributions of local volume and crystalline order parameters and find that the distributions of order parameters are not predicted solely by hard-sphere constraints.

TABLE OF CONTENTS

LIST OF TABLES

Table **Page**

LIST OF FIGURES

Figure **Page**

CHAPTER 1

INTRODUCTION

1.1 Overview

Packings of monodisperse, hard spheres serve as an important model system in the understanding of granular matter, which is ubiquitous in nature and industry. Like construction aggregates that must be laboriously compacted to prevent the gradual settling of anything that is constructed on top of them, real spherical grains form stable packings over a large range of volume fractions and often adopt long-lived loose-packed states as their initial configuration. In fact most experiments probing the dense end of this disordered sphere-packing spectrum must employ a shaking or kneading procedure to compact the initial loose-packed states toward the densest disordered state named random close packing (RCP) by J. D. Bernal [9] which has volume fraction $\phi_{\mathrm{RCP}} \approx 0.64$ [83]. Only more recently has the lower bound or "random loose packing limit" (RLP) of this range been probed [67]. At the time of publication of the work in Chapter 2, doubts existed regarding the existence of an RLP limit distinct from RCP in the absence of cohesive forces [34] and experiments had yet to isolate the role of friction.

In this dissertation we study loose packings mechanically stabilized by direct interparticle contacts. In Chapter 2 we describe an experimental protocol to prepare sphere packings in the loose packing limit and establish the dependence of that state on the value of the interparticle friction coefficient. Then in Chapters 3 and 4 we experimentally probe the boundaries of solidity in this material and the mechanics of the material after the solid structure has failed, proposing a simple rheological model

that describes many of the features of the mechanical response. Finally, in Chapter 5 we investigate the three-dimensional structure of the RLP state and lightly compacted packings. We find the structure to be homogeneous and isotropic, spatial correlations to be short ranged, and that much of the longer ranged structure in the radial distribution function is determined by local structure. In the remainder of this introductory chapter, we consider the failure of standard equilibrium statistical mechanics in describing granular systems in general, provide an introduction to the literature on frictional hard-sphere packings and discuss the general argument concerning isostaticity of loose packing. Finally, we provide an overview of the findings of our research.

1.2 Inapplicability of Equilibrium Statistical Mechanics

The foundations of the statistical mechanics of equilibrium thermodymanic systems do not apply to granular systems. In thermodynamic equilibrium, detailed balance and ergodicity ensure that time averages equal ensemble averages and, at least away from phase-transitions, these in turn equal spatial averages. Further, Liouville's theorem requires conservation of energy to justify the use of phase space, $\int dp\, dq$, as the flat measure of the probabilities over ensembles. Being dissipative and composed of particles too large and with barriers too great to be driven by temperature, granular systems do not satisfy any of these assumptions. The failure of phase-space as a flat measure, for example, has been demonstrated by the non-uniform sampling and the existence of valid states that are rarely or never seen in simulations of small systems [38, 2, 90, 95, 38, 22, 40, 39, 45].

A consequence of the inability of temperature to drive evolution in granular systems is that the statistics of fluctuations are not constrained in the way they are for equilibrium systems. This can make large, non-Gaussian fluctuations possible. However, if phenomena can be surprisingly long ranged in granular matter, the opposite

is also true and it will be a theme in Chapter 5 that many measures of structure are short ranged and that much of the longer ranged structure that does exist is a direct consequence of structure at very short ranges.

1.3 Sphere Packings

Packing density or "volume fraction," ϕ, is defined as the solid volume, V_{sphere}, divided by the total volume, V_{total}, in which the packing is confined:

$$\phi = V_{\text{sphere}} \,/\, V_{\text{total}} \ . \tag{1.3.1}$$

For non-cohesive spheres, confinement is an essential requirement for the solidity of the packing: packings of elastic spheres possess bulk shear moduli only when the packing is under compression. They do not behave as solids under tension.

The densest possible periodic packings of circles and spheres have long been known to be the hexagonal (honeycomb) lattice in 2d and in 3d any of the close-packed lattices where 2d hexagonal lattices are shifted and stacked in the troughs of the previous layer in face centered cubic or hexagonal close packing patterns, or any combination of these two layerings. These have been proven in both two and three dimensions to be globally denser than any possible non-periodic packings [37, 42]. While in 2d these lattices also put each sphere in the densest possible local packing arrangement, the 3d dense lattices do not, so that close-packing has volume fraction ≈ 0.74, but local volume fraction can be as high as ≈ 0.78 (see [89] for an account of the history of packing problems).

The study of disordered packings of equal spheres dates to the 1960's when it was first recognized that real frictional spheres arrest in a range of "loose" volume fractions and must be kneaded or tapped [82, 56, 77] to reach the upper bound of the random close packing (RCP) limit, $\phi_{\text{RCP}} \approx 0.6366(5)$ [83]. This upper bound has

later been found by simulation to coincide with the unique volume fraction available to disordered packings of frictionless hard spheres, $\phi_c = 0.639(1)$ [64, 65]. Thus this RCP limit, $\phi_{\mathrm{RCP}} \approx 0.64$ appears to be independent of the detailed properties of the preparation protocol and of the spheres themselves.

In 1990 Onoda and Liniger demonstrated that a lower, "random loose packing" (RLP), limit to this volume fraction range of disordered sphere packings of $\phi_{\mathrm{RLP}} \approx 0.555$ [67] is obtained when sedimented packings are prepared in nearly density matched fluids. Doubts remained, however, about whether nearing the neutral buoyancy limit represented the slowing of dynamic parameters [97] or simply passage to a regime where gravitational forces are small enough to be supported by cohesive interparticle forces such as Van der Waals forces [34]. And while simulations had shown that sphere packings are not stable below RCP in the absence of friction [64], experiments isolating the role of friction in RLP had not been done. Our experiments described in Chapter 2 were intended to experimentally address the question of whether such a distinct RLP limit in fact exists for frictional but completely cohesionless spheres and, if so, what experimental parameters control whether the RLP state is reached.

1.4 Mechanical response

1.4.1 Solid Mechanics at RCP

A substantial body of work explores the remarkable mechanics near random close packing via simulation of frictionless elastic spheres [65, 27, 85, 78] (see [20] for a recent review). Spheres with purely repulsive pairwise interparticle potential of the form:

$$V(r_{i,j}) = \begin{cases} \epsilon/\alpha \left(1 - r_{i,j}/\sigma_{i,j}\right)^{\alpha} & , \quad r_{i,j} < \sigma_{i,j} \\ 0 & , \quad r_{i,j} \geq \sigma_{i,j} \end{cases} \tag{1.4.1}$$

are found to exhibit power-law scalings of the pressure, p, bulk modulus, B, and shear modulus, G, as functions of their confinement above the jamming volume fraction, $\Delta\phi = \phi - \phi_c$:

$$p \propto (\phi - \phi_c)^{\alpha-1} \tag{1.4.2}$$

$$B \propto (\phi - \phi_c)^{\alpha-2} \tag{1.4.3}$$

$$G \propto (\phi - \phi_c)^{\alpha-3/2} \ . \tag{1.4.4}$$

all involving the exponent, α, of the interparticle potential. These scalings possess the interesting property that the shear modulus scales differently than the bulk modulus with the ratio $G/B \sim \sqrt{\phi - \phi_c}$ going to zero at small compression [65]. These results come from simulations without friction or dynamics so it is an open question whether they will hold in loose packings of real spheres that are stabilized by frictional contacts and in which dynamics may play a role.

Even if these scalings translate to loose packings of real spheres, it is unclear over what range to expect elastic behavior. The range of the harmonic approximation from which these moduli were extracted in simulation is narrow [78], however, there may be a larger range where systems under cyclic shear enter reversible loops of states [79]. So how these simulation results translate to a real elastic regime is unclear.

It is conceivable that an elastic regime bounded by a true yield stress may not exist in these materials. There are many reports of creep flow at small stresses in real granular materials [43, 62, 7] meaning that the yield stress may not be experimentally accessible. Yield stresses that strengthen with age [55, 50, 17] have also been reported, suggesting that granular packings may not be entirely static.

Little is known about the solid mechanics of loose packings near RLP. Simulations have measured the bulk modulus at ϕ_{RLP}, but not the shear modulus [85]. Experi-

ments have observed logarithmic creep under constant-stress conditions [62] raising doubts that a true yield stress exists in loose sphere packings.

1.4.2 Steady State Flow

A commonly observed phenomenology in yield stress fluids is that there is a critical stress, σ_c, above which shear stress follows a power-law dependence on strain-rate, $\dot{\gamma}$, behaving as a "Herschel-Bulkley fluid:"

$$\sigma_{\text{steady}} = \sigma_c \cdot (1 + (\dot{\gamma}\,\tau)^n) \ . \tag{1.4.5}$$

In granular fluids the exponent, n, has been observed to range from 1/2 to 1 and as low as 0.3 in experiments and simulations [44, 7, 94, 52, 14, 26, 73]. Reports on the stability of granular flows above σ_c vary. Very slow steady flows have been observed as σ_c is approached from above [80, 60, 72], however, there are also indications of instabilities near σ_c [29, 25, 51].

The few investigations of steady state flows in loose packings report finding rate-independent stress scaling [80, 60]. Whether Herschel-Bulkley scaling occurs in loose-sphere packings at higher strain-rates is unknown.

1.5 Structure

1.5.1 Contacts

Perched at the intersection of mechanics and geometric structure, is the average number of contacts per sphere or "coordination number," Z: one of the most studied properties of granular packings. Frictionless simulations of elastic spheres observe a scaling of the coordination number, Z, for packings under confinement [65],

$$Z - Z_c \propto (\phi - \phi_c)^{1/2} \tag{1.5.1}$$

where $Z_c = 6$ is the coordination number in the limit of zero confinement and $\phi_c \approx \phi_{\mathrm{RCP}} \approx 0.64$.

The coordination number in the limit of zero confinement, $Zc = 6$, matches the prediction of the "Isostatic Conjecture" [1]. Treating stability of a packing of hard-spheres as a constraint satisfaction problem, the number of forces must balance the number of constraints [1]. This sets the minimum number of bonds needed for a packing to avoid having unstable modes. The conjecture is that, in the limit of zero confining pressure, the loosest possible disordered packings exist precisely at this lower bound [1]. The intuition is that introducing extra contacts would also tend to increase the packing fraction. For d-dimensional spheres, the isostatic argument predicts $Z_{\mathrm{iso}} = d + 1$ for highly frictional spheres and $Z_{\mathrm{iso}} = 2\,d$ for frictionless spheres [35].

The isostatic conjecture matches the range of coordination numbers seen in simulations of sphere packings: 4 for high friction to 6 for zero friction [1, 33, 85] [1] but it falls well below the number of contacts measured in experimental sphere packings which range from about 5.5 to 7.0 [10, 84, 58, 5] and it is an open question whether this discrepancy is due to the difficulty in distinguishing contacts from the large number of near misses or whether real packings of frictional spheres tend to have more than the minimum number of contacts necessary for stability.

1.5.2 Near Misses

The scaling of coordination number seen in Eq. 1.5.1 is also noteworthy in that it predicts that the coordination number will increase with the square-root of confinement. This coincides with the exponent of the power-law divergence of near-contacts first seen in the pair correlation function in simulations by Silbert *et al.*[86],

[1] Counting arguments can be difficult to apply even to obtain the lower bound of Z. The isostaticity argument for ellipses over-predicts the minimum number of contacts necessary to stabilize packings when the ellipses are nearly circular [33].

$$g(r) \propto (1 - r/d)^{-1/2} \quad \text{for } d < r \lesssim 1.4\, d \tag{1.5.2}$$

These two square-root compression scalings seem to be linked: one can explain the growth in the excess contact number in terms of these near-misses becoming contacts as density is increased [65], however, the 1/2-power scaling in the pair-correlation function is not itself understood. This divergence of near misses is also significant because it may explain the higher coordination numbers measured in experiments versus those obtained from isostaticity and simulation.

1.6 Summary of results

In this dissertation we describe experiments exploring the loose end of the range of the volume fractions available to disordered packings of hard, frictional but non-cohesive polymethyl methacrylate spheres formed by sedimentation. Chapter 2 is concerned with the existence of a lower, "random loose packing" (RLP) limit in such a system and the role of dynamics and other parameters in the preparation of packings near this RLP limit. We show that loose-packed states with volume fraction below that of random close packing are possible for frictional but non-cohesive spheres and demonstrate that the dynamics of their formation, as characterized by the Stokes' number, determines whether the packing arrests in the loosest possible state. The volume fraction of packings created by sequential sedimentation is found to abruptly go to a random loose packing (RLP) limit as Stokes' number drops below ≈ 10, consistent with the vanishing of the interparticle restitution coefficient. To quantify the friction-dependence of this RLP limit, we introduce a new experimental method of measuring the interparticle friction coefficient in an environment very similar to that of the packing and find that lower RLP volume fractions are obtained with higher static friction particles.

In the chapters that follow, we experimentally probe the boundaries of solidity in this material and the mechanics of the material after the solid structure has failed, proposing a simple rheological model that describes failure which we then expand to include other features of the mechanical response. In Chapter 3 we present data on the mechanical response of similar packings to applied shear conducted near the loose packing limit. At very small shear strains, we find the apparent strength or "yield stress" of the material to display approximately cube-root power-law strain-rate scaling with an unexpected symmetry between the functional dependence on age of the packing and the strain-rate. We observe that a modification of the Maxwell model of viscoelasticity describes both the value of the exponent and the symmetry between age and rate. In the following chapter, we present shear-response data beyond the apparent yield point where we catalog a number of new features of the mechanical response and observe that beyond the yield-point the symmetry between strain-rate and age disappears. We observe that the scaling of many of these features can be described in a unified way by identifying the previous model as an expansion of the evolution of the viscous term in the Maxwell model in two variables: the applied stress, σ, and an emergent internal timescale, τ.

In Chapter 5 we study the structure of this system via three-dimensional imaging. We present data supporting the assumptions of homogeneity and isotropy made in the analysis of the mechanical results in the previous chapters and quantify wall-effects, finding them to unexpectedly suppress volume fraction over a short range. We observe no evidence of crystallization near the walls. We present data on average radial structure, distributions of volume fraction, and structural parameters defined locally. Using the Ornstein-Zernicke equation [68] we demonstrate that much of the radial distribution function, $g(r)$, is a consequence of the sharp features at the radial distance of one sphere diameter. We measure spatial auto-correlations and cross-correlations between local scalars and find these measures of structure to be

quite short-ranged. To test the hypothesis that the local structure is random subject to the number of neighbors and hard-sphere constrains, we compare measured distributions of Steinhardt-Nelson order parameters to those obtained by Monte-Carlo simulation of the nearest-neighbors of a single sphere. We find that the distributions of crystalline order parameters do not match the data indicating the presence of non-trivial structure in the arrangement of neighbors.

CHAPTER 2

THE RANDOM LOOSE PACKING LIMIT

2.1 Introduction

This chapter describes a completed project published in *Soft Matter* [36] and borrows heavily from that paper. The early experimental design on the volume fraction measurements in this project was done by coauthor Michael Martini.

Since the early studies of random close packing, it has been observed that stable disordered packings of cohesionless, frictional, spheres exist over a broad range of volume fractions [82, 56, 77, 83] via a number of different packing protocols. $\phi \in [0.57, 0.64]$ have been achieved by pouring in air followed by kneading [10] or tapping [82], $\phi \approx 0.58$ by pouring around a stick then slowly removing the stick [5], $\phi \in [0.56, 0.625]$ by fluidization in air followed by tapping [62], $\phi \in [0.575, 0.628]$ by fluidization in water [60], and $\phi \in [0.555, 0.60]$ [67] and $[0.54, 0.59]$ [36] by sedimentation in fluid. Loose packings have also been generated by dilating denser packed states via flow [75] or tapping [63].

An upper limit on the volume fraction of such disordered sphere packings was established early on, that of the "random close packed" (RCP) state with $\phi_{RCP} \approx 0.64$ [83]—the highest volume fraction consistently achieved in experiments with disordered packings of frictional spheres. This volume fraction $\phi_c \approx 0.64$ also corresponds to the lowest volume fraction seen in simulations of jammed packings of frictionless spheres [65].

The apparent robustness of the value of ϕ_{RCP} has motivated attempts to understand RCP in purely geometric terms [46] or in terms of the statistical mechanics of

hard spheres or soft spheres at zero temperature [90, 38, 49]. [1] In this chapter we experimentally explore the *lower* bound on volume fractions of mechanically stable packings of frictional, noncohesive, identical, hard spheres. Specifically, our questions are: does a loose packing limit exist for frictional but cohesionless spheres? Will this loose packing limit depend on the properties of the particle and the preparation protocol or, like the RCP limit, will it be robust to changes in these variables, and possibly admit descriptions in terms of the statistical mechanics of hard spheres [9]?

In the first systematic study of loose packings, Onoda and Liniger (1990) sedimented glass spheres in fluids of varying densities ρ_f, approaching the density ρ_s of the sphere [67]. They found that the packing fraction approached an asymptotic state which they refer to as "random loose packed" (RLP) with $\phi_{RLP} = 0.555$, in the limit of vanishing gravitational acceleration in the fluid, $g_f \equiv g\,(1 - \rho_f/\rho_s) \to 0$. However, the limit $g_f \to 0$ conflates two different physical effects, both of which may plausibly lead to lower volume fractions. The first effect involves the dynamics of assembling the packing: as $g_f \to 0$, falling spheres reach the packing with less inertia to explore the surface and rearrange their neighbors. This can trap the particles in higher-energy, fluffier packings in perhaps the same way that dynamic variables such as damping and restitution coefficients are tuned in simulations to create loose packings [97, 87]. A second, distinct, effect concerns the statics of the structure: as neutral buoyancy is approached, more fragile packings may become stable since the gravitational load borne by the packing vanishes relative to weak cohesive forces. Indeed, simulations [34] by Dong *et al.* argue that attractive van der Waals forces are important in stabilizing the packings of Onoda and Liniger at small g_f. Since arbitrarily low packing fractions can be attained when attractive interparticle forces

[1] At present there is a growing consensus that ϕ_J is not uniquely defined for frictionless systems [21, 90] (see [19] and references therein). It seems likely that the highest volume fractions available to frictional spheres may not be sharply defined either.

are dominant [92], this interpretation argues against the uniqueness of Onoda and Liniger's RLP state and questions the ability to experimentally access an RLP limit for cohesionless spheres.

A key goal of our experiments is to peel apart the distinct effects of fluid properties on the statics and dynamics. We accomplish this by independently controlling the viscosity and density of the fluid, allowing us to test whether the loose volume fractions achieved in the limit of small static weights are the same as those achieved by slow deposition at relatively large density mismatches. We find that the RLP state does appear unique in this sense and that the approach collapses against the Stokes number, St, with an abrupt transition to the RLP limit at $St \approx 10$ which we believe is associated with the vanishing of the restitution coefficient.

We conclude, then, that the RLP state for cohensionless, hard spheres, is well defined with respect to the parameters of sedimentation. We ask whether the RLP state is also unique with respect to the properties of the solid particles. Loose volume fractions have long shown signs of dependence on the material of the spheres [82, 77] with the relevant material property conjectured to be surface roughness [83, 67] which is experimentally found to correlate with angle of repose [48].

These differences in surface properties are generally modeled by a coefficient of friction. Simulations of frictional spheres find the RLP limit to be a systematically decreasing function of friction [97, 86, 22, 87, 85] albeit with unexpectedly large values ($\mu \approx 1.$) needed to reproduce values seen experimentally [67, 48].

In this chapter we describe a new experimental apparatus to measure friction coefficients between spherical beads in the fluid environment of the packing experiments. We describe the measured friction distributions and find that the mean of the distribution is quite large in this range of normal forces. Plotting the asymptotic RLP packing fractions of different sets of beads against the means of these static friction distributions, we present the first experimental determination of the range

Table 2.1: Fluids used in hour-glass sedimentation experiments (Table taken from our Soft Matter publication Ref [36], reproduced by permission of The Royal Society of Chemistry). The symbols match those used in all figures. Mixture ratios reflect contents before degassing. Density and viscosity were measured after degassing. *lit. [54]. †our measurement. ‡lit. at 20C [54]. §MSDS.

fluid	density/$(g\,cm^{-3})$	viscosity/$(mPa\,s)$	symbol
n-pentane (Fisher Sci)	0.626‡	0.23*	◀
n-heptane (Fisher Sci)	0.684‡	0.41*	▷
water (Millipore)	1.00‡	1.03*	▽
n-dodecane (Fisher Sci)	0.75	1.53*	▲
∼71/29 n-dodecane/light mineral oil mixture	0.78†	3.02†	○
∼50/50 n-dodecane/light mineral oil mixture	0.80†	5.96†	□
∼48/52 n-dodecane/light mineral oil mixture	0.82†	11.5†	♦
light mineral oil (Fisher Sci)	0.83§	46.0†	◇
high temperature silicone oil (Acros Organics)	1.05§	117.†	●
0.01M NaCl in ∼70/30 propylene glycol/glycerol	1.09†	125.†	▶
heavy mineral oil (Fisher Sci)	0.83§	157.†	◁
Fluka 08577 Density and Viscosity Standard	0.87§	1270.§	▼

of packing fractions available to disordered, frictional hard-spheres as a function of friction coefficient.

2.2 Experimental Methods

2.2.1 Measurement of Volume Fraction

We prepared mechanically stable packings of monodisperse spheres immersed in fluids, in an hour-glass shaped apparatus (Fig. 2.1) placed on a vibration-isolation table. Using a variety of fluids (Table 2.1) and spheres (Table 2.2) we formed packings under a wide range of viscosity and buoyancy conditions allowing distinctions to be drawn between the relative merits of different parameters controlling the approach to the RLP limit.

Packings were prepared by inverting the hour-glass shaped cell and allowing particles to settle through the fluid under gravity. The hour-glass geometry consists of two conical sections with a cone angle of 60° and base diameter of 24 sphere-diameters ($d = 2\,r$) connected by a cylindrical neck of $4.2\,d$ in diameter, which is only as wide as necessary to avoid jamming by arch formation in the neck. The narrow neck allows the passage of only a few particles at a time. (We have also deposited spheres singly

Table 2.2: Properties of sets of spheres (Table taken from our Soft Matter publication Ref [36], reproduced by permission of The Royal Society of Chemistry). We measured particle diameter using a technique similar to Scott's[83], measuring the length of ~ 100 spheres in a groove. Density was calculated from this diameter and the weight of these spheres. To quantify polydispersity and sphericity, we measured the diameter of individual spheres with a machinist's micrometer accurate to $2.5\mu m$, along five or more directions. "Asphericity" is the relative deviation from sphericity calculated as the standard deviation of these diameter measurements relative to the mean. "Polydispersity" is the standard deviation of the average diameters of a set of 20 spheres relative to the mean. "RMS roughness" gives the root-mean-square deviation from sphericity of profilometer traces taken of the sphere's surface(see Fig. 2.2). $\bar{\mu_s}$ and σ_{μ_s} are the mean and width of the distribution of static friction coefficient of gently contacting spheres in fluid (see Fig. 2.7).

sphere material	diameter/cm	density/$(g\,cm^{-3})$	polydispersity	asphericity	RMS roughness/μm	$\bar{\mu_s}$	σ_{μ_s}
PTFE	0.3205(4)	2.1389(9)	$0.21 \pm 0.06\%$	$0.14 \pm 0.06\%$	1.1 ± 0.6	0.540(3)	0.10
aluminum	0.3191(3)	2.775(3)	$\leq 0.04\%$	$\leq 0.04\%$	0.32 ± 0.14	0.62(6)	0.16
steel	0.3179(4)	7.774(7)	$0.14 \pm 0.05\%$	$\leq 0.04\%$	0.10 ± 0.02	0.66(14)	0.15
smooth acrylic	0.3174(3)	1.1800(9)	$0.15 \pm 0.06\%$	$0.06 \pm 0.04\%$	0.7 ± 0.3	0.88(3)	0.10
etched acrylic	0.3092(3)	1.1741(9)	$0.16 \pm 0.07\%$	$0.08 \pm 0.05\%$	2.6 ± 0.1	0.96(3)	0.10

by a mechanical dropper, with very similar results to those reported here.) The packing grows as a conical pile at the angle of repose ($\approx 23 - 26\,^\circ$), which is much smaller than the cone angle of the container, thus eliminating any empty pockets near the walls. The conical cell was chosen to minimize the weight supported by the sloping walls of the container. No crystalline order was observed near the bottom or side walls.

Measurements of the volume fraction of the packing are performed when the top surface of the packing just enters the neck of the cell. The total volume of the packing is the volume of the cone plus the small contribution from the spheres that are in the neck. The latter is determined from an image of the topography of the top surface of the particles (inset Fig. 2.1). All volume fractions reported in this dissertation are subject to the same systematic error in the range $\delta\phi \in [-0.002, 0.000]$ due to uncertainties in these volumes and in the volume of the hour glass.

The particles used in our experiments are commercially available spheres of acrylic (PMMA), Teflon (PTFE), steel, and aluminum with nominal diameter $d \approx 3.18\,\mathrm{mm}$ (see

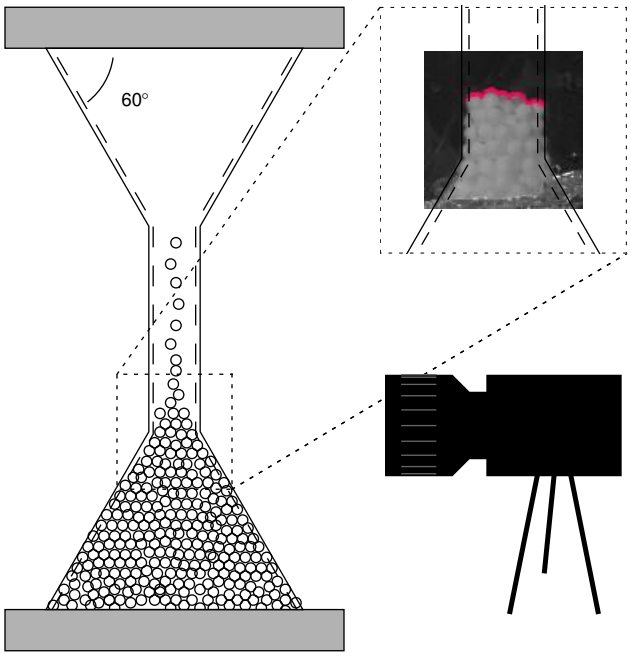

Figure 2.1: Hour-glass shaped sedimentation apparatus taken from our Soft Matter publication Ref [36], reproduced by permission of The Royal Society of Chemistry. Top right: Image of the topography of the top surface of the particles. Since the volume is estimated from a single projection, there is a small systematic positive bias in measuring the volume of the packing leading to a small negative bias in the packing fraction of $-0.002 \lesssim \delta\phi < 0$.

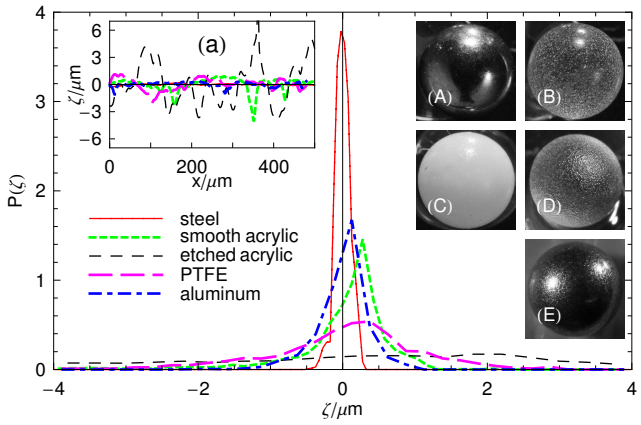

Figure 2.2: Histograms of roughness ζ of spherical particles as measured with a Dektak3 profilometer taken from our Soft Matter publication Ref [36], reproduced by permission of The Royal Society of Chemistry. Inset (a): Select profilometer traces ζ as a function of distance along the surface x (the gross curvature of the sphere has been subtracted). Images of spherical particles: (A) steel, (B) smooth acrylic, (C) PTFE, (D) solvent-etched acrylic, (E) aluminum.

Table 2.2, Fig. 2.2). We also use acrylic spheres which were roughened by timed etches in acetone. All sets of spheres are very monodisperse and highly spherical with, at worst a deviation from sphericity of $\sim 10^{-3}d$, a surface roughness of the same order, and a polydispersity of double this magnitude. These spheres are much larger than those used by Onoda and Liniger ($0.25 \pm 0.02\,mm$, glass). The advantages of using large spheres are evident: attractive van der Waals forces are smaller compared to other forces in the problem and the particles are of extremely high sphericity and monodispersity and more easily characterized. Thus these experiments represent a better approximation to the idealized packing of hard, monodisperse spheres than previous experiments.

Apart from van der Waals attraction, experimental results on the low packing fraction limit are sensitive to other attractive forces of electrostatic and capillary origin. In setting up the apparatus, great care was taken to degas fluids and to introduce the fluid to the spheres slowly to avoid entraining air bubbles which form attractive bridges between poorly wetted surfaces, especially rough ones. Pumping a vacuum on heated, stirred fluids for hours was often insufficient to avoid the appearance of attractive forces between spheres in non-wetting fluids, a phenomenon that has recently been associated with the existence of long-lived [6, 13] nanobubbles capable of exerting forces comparable to gravity for PMMA spheres in closely density matched fluids [70]. To avoid this phenomenon, we have used well-wetting fluids when possible and avoided close density matches in poorly-wetting fluids so that the contribution of attractive forces is in all cases negligible. Where charging effects were suspected, we repeated measurements with salts added to screen coulomb interactions.

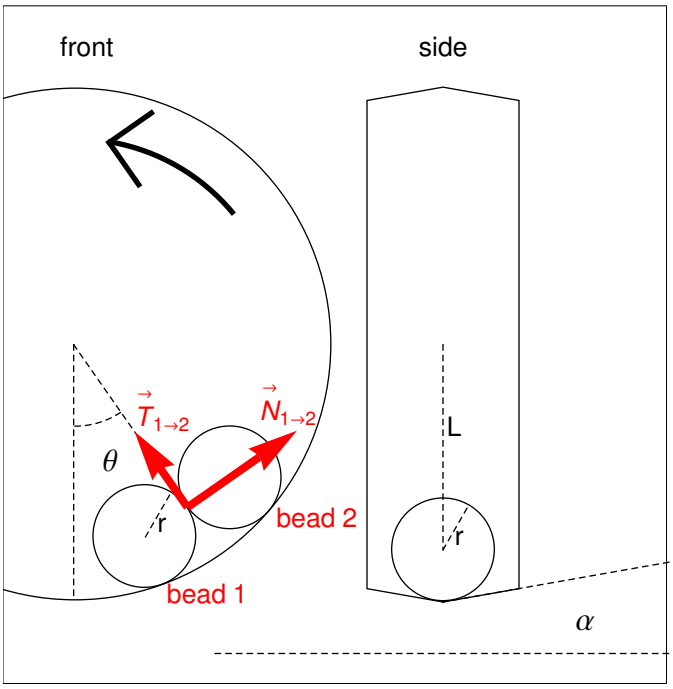

Figure 2.3: Geometry of the apparatus used in the friction measurement (scale: bead radius $r = 1.59\,mm$).

2.2.2 Measurement of Friction Coefficient

The coefficient of static friction, μ_s, is measured by a new technique sketched in Fig. 2.3 [2]. Two spherical beads of radius r sit inside a shallow v-groove of angle α in a vertical circular track. The entire apparatus is immersed in fluid. If there were only one bead present, it would roll under gravity and settle at the lowest point on the cylinder at $\theta = 0$. With two beads present, the friction between beads is able to provide a torque to oppose gravity. Thus the cylinder can be rotated about its axis without the beads rolling.

Let the cylinder rotate so that the point of contact of the beads is at an angular position θ with the beads numbered 1 and 2 as in Fig. 2.3. Even in the case where

[2] In our setup, $L = 6.35 \pm 0.03\,mm$, $r = 1.59 \pm 0.03\,mm$ and $\alpha = 10.0 \pm 0.5°$. L is the distance from the center of the track to the centers of the spheres whereas the radius of the track at contact with the beads is $L + s$.

the beads roll without slipping against the wall of the cylinder, the beads are stable for some $\theta > 0$ because there exists a normal force $\vec{N}_{1\to 2}(\theta)$ of bead 1 on bead 2 as well as a tangential force $\vec{T}_{1\to 2}(\theta)$ caused by static friction between beads. One can see from the diagram in Fig. 2.3 that this tangential force is in the correct direction to exert a torque preventing bead 2 from rolling. Similarly, there is an equal and opposite torque supplied by bead 2 on bead 1 preventing it too from rolling so long as the Coulomb inequality is not exceeded: $|\vec{T}_{1,2}(\theta)|/|\vec{N}_{1,2}(\theta)| \leq \mu_s$. We determine μ_s by looking for the maximal angle, θ_{max}, at which this inequality holds. The result is (see Appendix A for calculation):

$$\mu_s = \frac{L^2/r^2 - 1}{L/s + 1} \tan(\theta_{max}) \tag{2.2.1}$$

where $s = r\cos(\alpha)$.

In obtaining this result, it is assumed that drag coming from fluid viscosity is negligible as is static rolling resistance between the beads and the cylinder wall. Both of these assumptions can be tested experimentally. At slow rotation frequency, ω, the drag of the fluid is expected to scale with ω, thus the drag force can be made small by rotating the cylinder slowly. The impact of static rolling resistance can be checked by comparing torques associated with θ_{max} for one bead, where there is only rolling and fluid resistance, with the torque associated with θ_{max} in the two-bead case. The factors under experimental control likely to impact rolling resistance include the hardness of the beads and cylinder; and the angle, α, of the v-groove in the cylinder.

Whereas simulation work to date on loose, frictional sphere packings has used a simple Coulomb friction model with a uniform coefficient of friction, μ, our early results measuring the coefficient of friction suggests that this model may be too idealized to describe real granular materials. In our experiments which use very high quality grains (see Fig. 2.2 and Table 2.2), the friction coefficient is found to be neither constant between pairs of beads nor constant spatially over the surface of

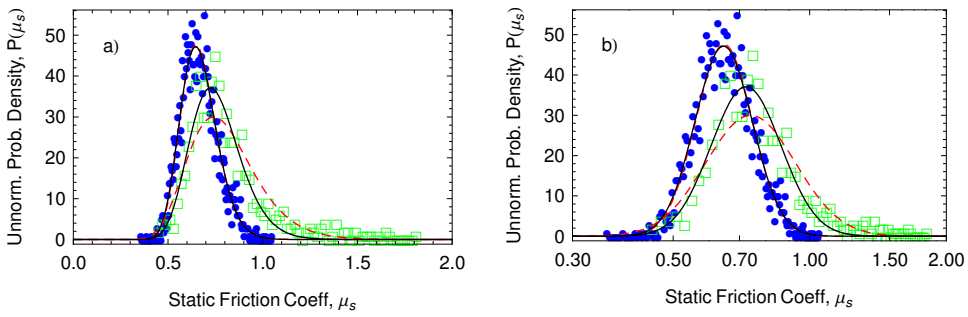

Figure 2.4: Unnormalized distributions of static friction coefficient as measured via the maximum angle of stability of single pairs of steel (filled blue circles) and acrylic (open green squares) spherical beads. Plot a) has linear axes; plot b) has a logarithmic horizontal axis. Solid black and dashed red lines are fits to the log-normal distribution calculated via the moments of the transformed distributions and nonlinear least–squares fitting respectively.

a single bead, the distribution of static friction being wide with large mean and a heavy tail. An example of the broad shapes of the static friction distribution is given in Fig. 2.4. The distributions are found to be approximately log-normal for the steel beads but with a much heavier large-μ tail for acrylic beads.

We note that the distribution of friction coefficient likely reflects a biased sampling. In the friction measurement apparatus, the point of contact between the spheres is the point of arrest of the spheres themselves and it seems likely that if μ_s is spatially uneven across the bead surfaces, that the beads would be more likely to arrest at a point of higher than average friction coefficient than at one of lower than average friction coefficient [3]. Thus spatially nonuniform friction coefficients may not be well characterized by the mean of their distribution if they can be modelled by a single friction parameter at all.

[3]It is interesting to speculate that a similar bias towards arresting at points of higher than average or even outlying friction coefficient may also be occurring in the packing itself. It may be that the friction coefficients at the points of contact in real granular systems are much higher than the average value for the grains themselves.

2.3 Results and Discussion

2.3.1 Dimensional Analysis

Onoda and Liniger in 1990 [67] and Jerkins *et al.* in 2008 [48] find that a loose packing limit can be reached in sedimented and fluidized systems in the limit of low static load on the packings. Onoda and Liniger express this as the limit, $\Delta g = g_f/g \to 0$, where, g_f, is the gravitational acceleration experienced by the beads in the fluid and g is the acceleration of gravity. This is confusing, however, because g does not appear to be an important acceleration scale in the problem. What acceleration scale, then, should g_f be compared to?

In our experiment, we eliminate interparticle force scales so the balancing force must be the viscous drag of the fluid. There appear to be five parameters in the problem: r and ρ_s the radius and density of the spheres; ρ_f, η the density and dynamic viscosity of the fluid; and $g_f = g\,(1 - \rho_f/\rho_s)$, the buoyancy-reduced gravitational acceleration experienced by particles in the fluid. These five parameters involve three independent units (length, time, and mass), so we expect to construct two independent dimensionless combinations. Following the conventional definitions [57] of Reynolds' number, $Re = 2\,\rho_f\,V\,r\,/\eta$, and Stokes number, $St = 2/9\,\rho_s\,V\,r\,/\eta$, where $V = 2/9\,r^2\,g_f\,\rho_s\,/\eta$ is the terminal velocity of a particle falling at low Reynolds number. Convenient choices of the two independent parameters are the Stoke's flow limits of the Reynolds number, $Re \to R$, and the Stokes number, $St \to S$:

$$R = 4/9\,r^3\,\rho_s\,\rho_f\,g_f\,/\eta^2 \tag{2.3.1a}$$

$$S = 4/81\,r^3\,\rho_s^2\,g_f\,/\eta^2\ . \tag{2.3.1b}$$

or equivalently either of these and their ratio $S/R \sim \rho_s/\rho_f$.

In principle, $R \to 0$ and $S \to 0$ could tune different RLP limits, however, in practice as these differ only by the ratio of densities, ρ_s/ρ_f, it is difficult to make

just one of these small [4]. Both of these parameters have standard interpretations. The Reynolds number is the ratio of intertial to viscous force scales in the flow, so it is plausible that the Reynold's number affects the state of the packing in a way independent of S. The Stokes number, S, however, has clear implications for the dynamics of the sedimenting particles. In the small-Re limit, it is a measure of the kinetic energy of a falling particle relative to the gravitational potential energy over the particle's radius. It is also a measure of the damping length of a falling particle relative to the particle's diameter. Thus the Stokes number seems to quantify both the ability of a sedimenting particle to knock the packing out of a potential energy minimimum and also the distance which it has to explore before settling into a new local energy minimum. We shall see, however, that there is another role of Stokes number, that of controlling the value of the restitution coefficient between spheres, that appears to be more important than either of these in controlling the passage to the RLP limit.

2.3.2 Random Loose Packing Limit

We display in Fig. 2.5 the major result of this chapter. For spheres of a given material, the packing fraction decreases as sedimentation is done more gently. When plotted against the dimensionless group S, the volume fraction approaches an asymptotic limiting low volume fraction which we may interpret as ϕ_{RLP}. We note the limiting ϕ_{RLP} is different for spheres of different materials. The asymptotic limit is directly available from the data, and unlike in previous measurements need not be obtained by extrapolation (for which there is no reliable theoretical guideline). Each data point is taken with a different liquid, and not with a chemical series or a dilution series; the smooth approach to this limit thus suggests that the macroscopic parame-

[4]Large density mismatches might be possible with hollow particles or perhaps with fine particles in air.

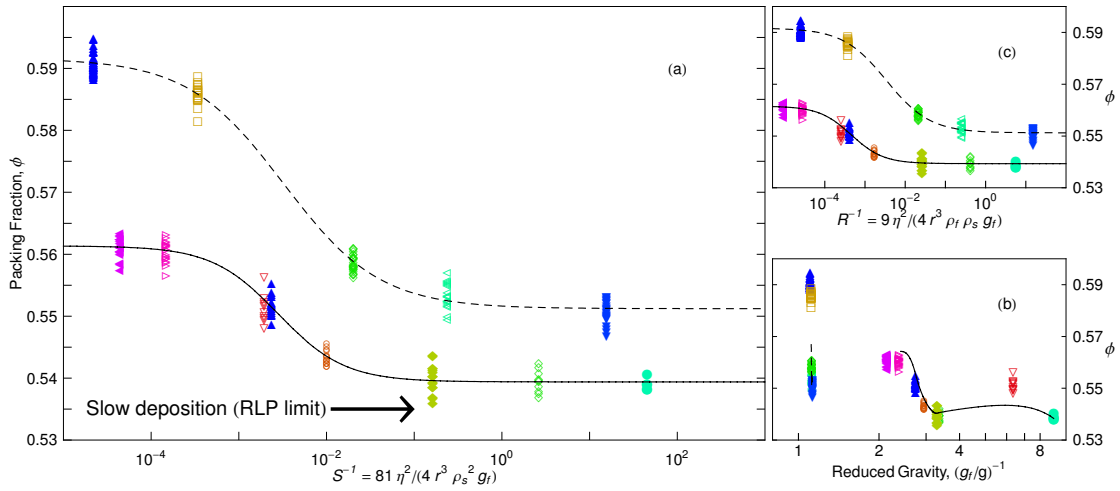

Figure 2.5: Packing fraction, ϕ, vs. the dimensionless parameters S, R, and g_f/g (taken from our Soft Matter publication Ref [36], reproduced by permission of The Royal Society of Chemistry). The data points represent individual packings; the spread in the data is much larger than the random error on each data point. For a particle falling at low Reynolds number, S is the Stokes number and R is the Reynolds number itself. g_f is the buoyancy-reduced gravitational acceleration felt by a particle in the fluid. (Onoda and Liniger's $\Delta g \equiv g_f/g$ [67].) In all three graphs the solid line connects data for smooth acrylic spheres and the dashed line is for steel spheres.

ters of the fluid and sphere are sufficient to fully characterize the preparation process, and that any microscopic interparticle interactions mediated by the fluid have been successfully suppressed.

Furthermore, Fig. 2.5(b) shows that the degree of density matching, quantified by $g_f/g = 1 - \rho_f/\rho_s$ (Onoda and Liniger's Δg), is not an appropriate parameter to define the RLP limit of this packing protocol. Low packing fractions can be achieved without density matching, by sedimenting in sufficiently viscous fluids. For a fluid of a given viscosity, RLP can of course be approached by varying g_f/g, as the work of Onoda and Liniger and Jerkins *et al.* suggest. The role of g_f/g is however, not in reducing the static load on the packing structure, but purely in slowing down the dynamics of the packing process.

Fig. 2.5(c) shows that the volume fraction ϕ also smoothly approaches ϕ_{RLP} when plotted against the dimensionless group R. Since R and S differ only by a factor of the density contrast ρ_f/ρ_s, and available fluids fall within a narrow range of densities ($\rho_f \in [\approx 0.8\,\mathrm{g/cm^3}, \approx 1.2\,\mathrm{g/cm^3}]$), it difficult to choose on the basis of the smoothness of individual curves. A wider range of solid densities is available making the comparison of the asymptotic approaches between beads of different materials useful. In Fig. 2.5, trends for acrylic beads (solid line) and steel (dashed line) approach their asymptotic limits at different values of R but at similar values of S. This, in addition to the physical intuition that Stokes number should control the dynamics of the sedimentation, leading us to prefer S as the best candidate for the relevant control parameter. The Stokes number, after all, has also been identified as the parameter controlling the behavior of avalanches in fluid-immersed piles [25]—a system of direct relevance to the formation of packings, collapses and avalanches no doubt playing a role in the formation of packings.

One interesting observation that came out of the avalanche study [25], however, was that the interpretations we have given for Stokes number as damping distance

and kinetic energy are likely not the leading physical effects. Indeed, looking more closely at Fig. 2.5(a) we see some surprises. The $\phi(S)$ does not reach it's asymptotic limit ϕ_{RLP} slowly for $S << 1$ but rather abruptly near $S \approx 10$ where there should still be plenty of energy present to rearrange the packing or allow a bouncing particle to find a minimal energy position. Instead, the rapid approach of the asymptotic limit at moderately large S seems to coincide with the that of measurements of the restitution coefficient for collisions of fluid — immersed spheres on a flat surface [41] which show that the Stokes number St — and not Reynolds number Re — is the relevant dimensionless parameter that defines the onset of bounce-free collisions [28]. There is good quantitative agreement between the scale of St where bouncing ceases and where ϕ_{RLP} is attained (Fig. 2.6). Thus control of restitution coefficient appears to be the most important role played by the Stokes number in the passage to the RLP limit and it is unclear how important its role as a nondimensional rate of packing formation is.

We now return to the observation that the two curves in Fig. 2.5 corresponding to steel and acrylic spheres approach different values of ϕ_{RLP} of 0.551 and 0.540 respectively. With the mass density of the materials already accounted for, the only relevant differences are those of the contact mechanics of the spheres. In particular, the coefficient of static friction, μ_s, between spheres is different. In Fig. 2.7 we plot the ϕ_{RLP} value against the mean of the friction distribution. Besides confirming the expected trend of higher friction yielding looser packings, our measurements (see also Table 2.2) show that the values of μ_s are larger than those normally quoted for the same materials at human-scale normal loads.

Unlike the high density limit ϕ_{RCP}, the loosest stable packing density, ϕ_{RLP}, has been shown in simulation to depend on the friction coefficient between particles [97, 86, 87, 85]. Ours is the first experiment, however, to measure the coefficient of friction between spherical grains in an environment similar to that in the packing, providing

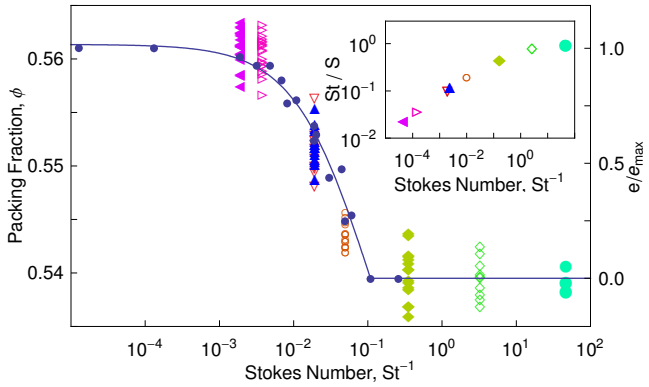

Figure 2.6: The main plot shows the packing fraction, ϕ, of acrylic spheres (left vertical axis, symbols match Fig. 2.5) versus Stokes number, St (Figure taken from our Soft Matter publication Ref [36], reproduced by permission of The Royal Society of Chemistry). We compare the trend with the data of Gondret *et al.*(from Fig. 6, Ref. [41]), plotted here in dark circles against the right vertical axis) for the St-dependence of the restitution coefficient e, scaled by its maximal value e_{max}. The data are for collisions of a Teflon sphere in a fluid, however, data for different materials collapse on the same curve. To make the comparison with Ref. [41], we inferred the value of St in our experiments from measured values (Table 2.2) and a standard drag curve [57]. This correction is shown in the inset; as expected the correction is small when St is small.

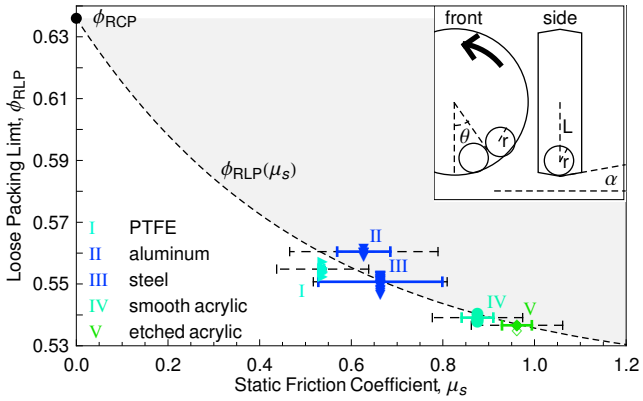

Figure 2.7: Limiting low packing fraction, ϕ_{RLP}, plotted versus μ_s, the mean static friction coefficient (Figure taken from our Soft Matter publication Ref. [36], reproduced by permission of The Royal Society of Chemistry). The dashed error bars indicate the width in the distribution of μ_s, and the solid error bars are uncertainty in the mean of μ_s. The shaded area represents the region of stable, disordered packings. The lower bound (dashed curve) is a guide to the eye. The inset shows a drawing of the geometry used in the friction measurement (scale: bead radius $r = 1.59\,mm$).

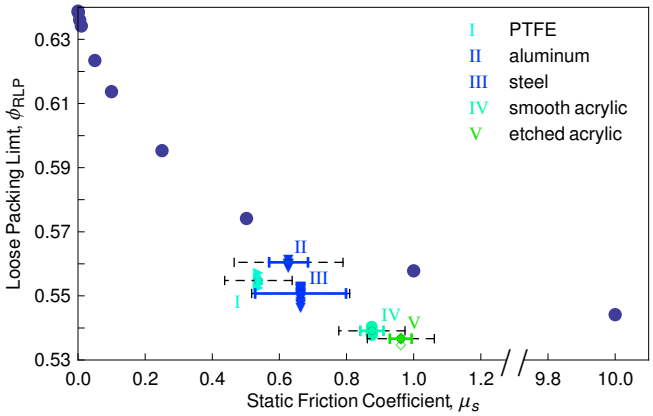

Figure 2.8: Limiting low packing fraction, ϕ_{RLP}, plotted versus μ_s, the mean static friction coefficient. Data labeled by Roman numerals are our experimental results [36] were ϕ_{RLP} is plotted against the mean of the frictional distribution (same as in Fig. 2.7). The solid black circles are from Silbert's simulations [85]. Note that there is a break in the horizontal axis allowing the inclusion of Silbert's highest μ data point.

the first experimental test [36] of the of the "jamming phase diagram" [87, 85] for frictional spheres at zero temperature, shear, and pressure.

Our data thus suggest a resolution of the puzzle that friction coefficients in simulated models [97, 86, 87, 85] need to be surprisingly large in order to achieve the volume fractions around $\phi \approx 0.555$ seen in experiments [67, 48]: namely that intergrain friction actually is large.

2.3.3 Since Publication

In the time since the 2010 publication in *Soft Matter* [36], the results in this chapter have generated interest and some have been generalized. Our finding that the density of the packing can be tuned by controlling the Stokes number of the sedimentating particles has, for example, been generalized to take into account the effect of the volume fraction on the settling rate in sedimenting colloidal fluids [53]. It is not yet clear, however, whether this result is applicable to the non-Brownian spheres we studied.

Much of the interest in our paper has regarded the mapping out of the volume fraction range available to frictional sphere packings. Prior work had suggested a friction dependence of the volume fraction of loose states [56, 77] and simulations had suggested that loose packings cannot exist without friction [64]. The particles in prior experiments, however, had generally been relatively small ($\sim 100\,\mu$m), polydisperse (5 to 10%), with uncharacterized surface features and friction coefficients quoted from the bulk material, if at all. We attempted to address these weaknesses by using large, high quality spherical particles, reporting surface profiles and attempting an *in situ* measurement of interparticle friction coefficient. With these results, we demonstrated a general trend of decreasing ϕ_{RLP} with increasing friction coefficient, μ. Consistent with our friction findings, Utermann et al. subsequently developed [91] an experimental technique to alter the surface profile of glass spheres and found a positive relationship between the vertical roughness scale and the angle of repose and a negative relationship with ϕ.

Parallel and subsequent subsequent simulation work on frictional hard sphere packings suggest similar $\phi_{\mathrm{RLP}}(\mu)$ trends, however, offset to slighly higher volume fraction. Fig. 2.8 shows that our experimental $\phi_{\mathrm{RLP}}(\mu)$-curve appears to be shifted downward about 0.02 in a volume fraction versus the simulation of Silbert (2010) [85] published alongside ours in *Soft Matter*. Subsequent simulation and theory [23, 24] have found similar trends. The cause of this offset is unknown but may be due to the finite size of our experiment which is especially likely given our finding in Chapter 5 that volume fraction is suppressed near smooth walls. The discrepancy, however, may also be due to differences between protocols in the experiment and simulation, or the simplistic model of friction used in the simulations.

Other interest in the results of this chapter includes Prof. Schröter's (2017) [81] use of our Fig. 2.2 showing the roughness of our spheres to support his viewpoint that more detailed models of the grains themselves are needed to understand real

granular materials [81]. Prof. Castellanos (2012) [18] theorizes that adding a static coefficient of rolling friction to the frictional hard-sphere model may explain both the high friction values and relatively low values of ϕ_{RLP} seen in our experiment as compared to the simulations.

CHAPTER 3

MECHANICS OF YIELDING NEAR RANDOM LOOSE PACKING

3.1 Introduction

This chapter describes a completed project that has been submitted for publication in *Physical Review Letters* and borrows heavily from that paper.

In this chapter we describe experiments investigating the rheology and yielding behavior of loose sphere packings created by the sedimentation process at low Stokes number described in the previous chapter. We find that the shear yield stress exhibits an approximately cube-root power-law dependence on both the age of the packing and the strain rate over a sufficient distance to distinguish this from other functional forms. Since no lower cutoff of this power-law scaling is seen, this result establishes an upper bound for reversible elastic response in loose packings. Further, we find the yield stress to be insensitive to both the volume fraction of the packing and the viscosity of the interstitial fluid.

We modify a recent model of viscoelastic rheology used by Nguyen et al. [62] to describe logarithmic creep in a loose sphere packing and find that this new model accounts for the scaling of the yield stress while also retaining its prediction of creep under constant-stress loading, thus unifying under a single, simple rheological model the phenomenology observed by us under constant strain-rate loading with that observed by Nguyen *et al.* under constant-stress loading.

3.2 Failure and Rheology in Loose Granular Matter

Loose packings of grains are ubiquitous in environments from sedimented river beds, to industrial processing of powders, to the soils of low-gravity planets. Loose packings can be created by sedimenting gently [67, 36], fluidizing packings [62, 66, 60], and dilating dense packings by tapping [63, 82]. For monodisperse spheres, these protocols lead to a range in volume fraction from $\phi \approx 0.54$ to 0.64 [67, 48, 87, 85, 36, 62, 60]. Recent experiments and simulations [36, 85] show evidence for a friction-dependent lower bound—the random loose packing (RLP) limit [67]—to the volume fractions that can be achieved for disordered packings of noncohesive spheres. This contrasts with the upper bound of achievable volume fractions—random close packing (RCP) [11]—which appears to be independent of friction [83, 85].

Thus spherical grains can pack over a large, friction-dependent range of volume fractions leading to a practical need to understand the mechanics of these solids. A substantial body of work explores the remarkable mechanics near random close packing [65, 27, 85, 78] (see [20] for a recent review). The loose packing limit, however, remains relatively less explored. The goal of our experiments is to investigate mechanical response and yielding at small shear strains near the loose packing limit.

A simple picture of failure in loose granular solids is that there is a single critical stress, σ_c, about which a transition occurs from solid to liquid behavior. For stresses above σ_c, rheological studies are often described by a Herschel-Bulkley dependence of stress, σ, on strain rate, $\dot{\gamma}$, for steady state flows:

$$\sigma_{\text{steady}} = \sigma_c \cdot (1 + (\dot{\gamma}\,\tau)^n) \ , \tag{3.2.1}$$

with the rate-exponent, n, ranging from 1/2 to 1 and as low as 0.3 in experiments and simulations [44, 7, 94, 52, 14, 26, 73]. Very slow steady flows have been observed as σ_c is approached from above [80, 60, 72], however, there are also indications of instabilities near σ_c [29, 25, 51]. As with Coulomb friction, these observations lead

us to differentiate between the "static yield stress," σ_y, required to initiate flow, and a smaller "dynamic yield stress" required to maintain flow.

The identification of σ_y as a true yield stress, however, is complicated by observations of creep flow for $\sigma < \sigma_y$ [43, 62, 7] and strengthening with age [55, 50, 17]. In an attempt to incorporate the phenomena of creep flow and aging into a rheological description of loose granular solids, Nguyen et al. extend the Maxwell model of viscoelasticity via an evolving viscosity variable, η (they write it in terms of fluidity, $f = G/\eta$):

$$\dot{\gamma} = \frac{\dot{\sigma}}{G} + \frac{\sigma}{\eta} \tag{3.2.2a}$$

$$\frac{\dot{\eta}}{G} = a - r\left(\frac{\dot{\gamma}\,\eta}{G}\right)^2, \tag{3.2.2b}$$

with aging and rejuvenation tuned by positive dimensionless constants a and r [62]. Equ. 3.2.2 reproduces logarithmic creep observed under constant applied stress [62] but remains untested under the complementary protocol of controlled strain.

In this chapter we describe constant strain-rate rheological measurements of loose packings prepared in a range of loose volume fractions and in different fluids. We present experimental evidence that the "static" shear yield stress, σ_y, undergoes power-law strengthening with age and with strain rate and does so symmetrically in these variables without sensitivity to either the volume fraction or the viscosity of the interstitial fluid. We do not observe a cutoff of this scaling at low strain rate and thus find no evidence for a reversible elastic regime. Finally, we show that when the rheological model of Equ. 3.2.2 is modified so that $\dot{\eta}$ depends on stress history rather than strain history, it successfully accounts for the yield-stress scalings presented here while retaining the creep predictions of Equ. 3.2.2. Thus the new model offers a unified description of the response of loose granular solids under constant strain-rate and constant-stress conditions.

3.3 Methods

3.3.1 Experimental Setup

We create loose packings of polymethyl methacrylate (PMMA) spheres (McMaster-Carr) of diameter, $d = 1.588\,\mathrm{mm}$, and density, $\rho_s = 1.18\,\mathrm{g/cm^3}$, chosen for their high sphericity and low polydispersity [36]. The particles are at all times immersed in a fluid with viscosity, $\eta_f = 110\,\mathrm{mPa \cdot s}$, and density, $\rho_f = 1.021(1)\,\mathrm{g/cm^3}$ composed of high-temperature silicone oil (Acros Organic) and mineral oil (Fisher Scientific) mixed in an 82.5:17.5 mass ratio. Some data were also taken with a lower viscosity fluid mixture with viscosity, $\eta_f = 5.37(4)\,\mathrm{mPa \cdot s}$, and density, $\rho_f = 0.799(1)\,\mathrm{g/cm^3}$, composed of mineral oil and n-dodecane in a 45:55 mass ratio. Both fluids strongly wet PMMA, and attractive forces arising from entrapped air are minimized by pumping the fluids after mixing to remove any dissolved gases. To minimize triboelectric charging, all parts of the sample cell are also made of PMMA. Van der Waals forces are negligible compared to the weight of the particles.

The spheres are enclosed in a container with a square cross-section of inner dimension $2\,W$ and a height of $184\,d$ (Fig. 3.1). A shear plane roughened by a disordered monolayer of beads melted to each side, is suspended in the center with an 8 mm gap between its edges and the side walls. The shear plane is supported from above by a load cell (Honeywell Sensotec AL311AP,4A whose bridge impedance is measured with a SR830 lock-in amplifier) and moved vertically with a step size of $0.254\,\mu\mathrm{m}$ by a servo motor (NI MID-7654 Servo Drive). The spheres rest on a base that is porous to the fluid, but not the particles. The container is filled with spheres to $160\,d$ leaving fluid above the top of the packing so that particles never breach the surface of the fluid.

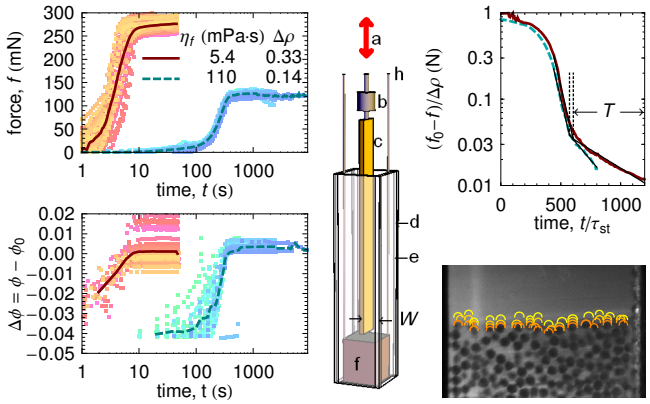

Figure 3.1: Experimental setup and preparation of the packing. Within a transparent, square cross-sectioned box, a roughened "shear plane" (c) is suspended from a motion stage (a) in the center of the container, in line with a force transducer (b). The sphere packing rests on a porous base (f) which is raised and lowered 2 cm via thin rods (h) to allow the spheres to settle. The distance from the shear plane to the boundary is the system width, W. The left column shows the force exerted on the shear plane and the change in volume fraction as the packing is formed. The approach to the long-time steady-state force, f_0, collapses (top-right), when the force is scaled with the relative buoyant weight of the particles, $\Delta\rho = 1 - \rho_f/\rho_s$, and time is scaled with the Stokes' timescale, $\tau_{\rm st} = 18\,\eta_f/(g\,d\,\rho_s\,\Delta\rho)$, of particles falling under gravity though a fluid of viscosity, η_f. A crossover to a slower relaxation appears to occur at $\sim 600\,\tau_{\rm st}$ corresponding to 430 s for $\eta_f = 110\,\mathrm{mPa}\cdot\mathrm{s}$ and 9.6 s for $\eta_f = 5.4\,\mathrm{mPa}\cdot\mathrm{s}$. The crossover provides a way to estimate the beginning of the aging time, T, of a freshly sedimented packing. The image shows surface profiles of a slice of the top of the packing moving downward while being compacted by a large upward motion of the shear plane (the yellow lines are sampled every 45 s, $\dot\gamma = v/W = 8.8\times10^{-5}$/s, $W = 18\,d$, $\eta_f = 110\,\mathrm{mPa}\cdot\mathrm{s}$).

3.3.2 Packing Preparation Protocols

Loose packings are prepared by sedimentation of the spheres at low enough Stokes' number ($S_t \approx 4 \times 10^{-3}$ for $\eta_f = 110\,\mathrm{mPa \cdot s}$ and $S_t \approx 4$ for $\eta_f = 5.4\,\mathrm{mPa \cdot s}$) to ensure they will form loose packings [36]. 3D imaging measurements (see Fig. 5.10 in Chapter 5) put the volume fraction after sedimentation at $\phi_0 \approx 0.565(5)$ which places it near the RLP limit for frictional spheres [85, 36]. Denser packings ($\Delta\phi = 0.00$ to 0.05) are created by inducing compaction with large, rapid oscillations of the shear plane.

As shown in Fig. 3.1, forces on the shear plane during sedimentation display an early relaxation phase at a timescale consistent with the viscous flow of interstitial fluid out of the compacting packing [16] then enter a phase of slower relaxation which we believe is associated with aging of the solid packing itself. In general when the age of the packing needs to be known, it is set by briefly fluidizing the packing with an upward motion of the shear plane of $\Delta z = 10^{-2}\,d$ (causes negligible compaction) then pausing for an "aging" or "waiting time," T. After the waiting time is complete, the static shear stress, Σ_0, is noted and upward motion of the shear plane is initiated at constant strain rate, $\dot{\gamma} = v/W$, while the shear stress, Σ, is recorded. $\sigma = \Sigma - \Sigma_0$ is taken to be the response to the imposed strain, γ.

Loose packings are prepared by sedimentation of the spheres first by raising the porous bottom 2 cm which lifts the spheres with it, then rapidly dropping the bottom and allowing the particles to settle at low Stokes' number, $S_t \approx 4 \times 10^{-3}$, which ensures they will form loose packings [36]. This process creates a packing in a volume fraction near ϕ_{RLP} which we refer to as ϕ_0.

Denser packings are created by subsequently inducing compaction with large, rapid oscillations of the shear plane (see Fig. 3.2). After achieving the desired increase in volume fraction ($\Delta\phi = 0.00$ to 0.05), a single, sharp upward motion of the shear plane, $\Delta z = 10^{-2}\,d$ (where d is the bead diameter), is applied to fluidize the packing

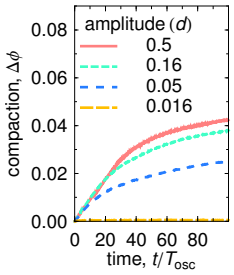

Figure 3.2: Compaction triggered by sinusoidal oscillation with period, $T = 6.6\,\mathrm{s}$. Larger amplitudes caused faster compaction although curves at the two lowest amplitudes nearly overlay. The inset image shows a slice of the top of the packing during compaction while the shear plane is drawn upward at constant velocity ($v/W = 8.8 \times 10^{-5}/\mathrm{s}$). Light-colored lines show previous surface profiles sampled every 45 seconds. While the roughened plane (visible on the right of the inset image) moves upward at constant velocity, the motion of the free surface is predominately a downward translation thus it is right to think of this phase of the packing's response as compaction rather than shear. Also telling in this picture is the decoupling of the motion of the roughened plane from that of the free surface. In this example the surface is moving downward at about four-times the (absolute) velocity with which the roughened plane is being dragged upwards.

with negligible change in the volume fraction. Large fast motions like this of the shear plane induce compaction rather than shear in the packing as evidenced by the relatively uniform downward motion of the surface of the packing in the bottom-right of Fig. 3.1 in response to rapid upward motion of the shear plane.

Thus we report measurements of yield stresses for packings that have been prepared and aged according to three slightly different protocols. Except for the open-squares, all the data in Fig. 3.5 was prepared by allowing a packing 600 s to sediment then briefly fluidizing the packing by moving the shear plane upward a distance $0.01\,d$, then waiting a variable length of time called the "waiting time," T, then commencing shear at rate $\dot{\gamma}$. In this protocol we associate the waiting time, T, with the age of the packing and makes it possible to set relatively short packing ages.

The first data series in Fig. 3.6 was prepared by lifting and dropping the packing and waiting a period of 600 s for sedimentation and aging to occur after which we applied the constant strain rate. Higher levels of compaction reported in the main

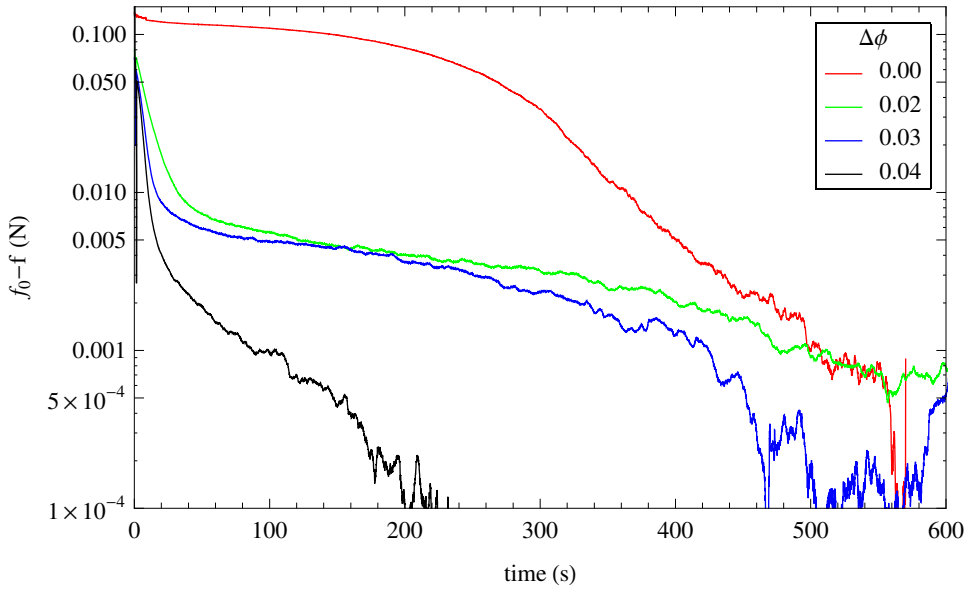

Figure 3.3: Average approach of force, f, to steady-state force, f_0. The $\Delta\phi = 0.00$ curve shows force as the packing sediments. The higher volume fractions show the relaxation of the force following sinusoidal compaction imposed at amplitude $d/2$ and period 6.64 s for 15, 30, and 90-cycles. As in the top-right of Fig. 3.1, the force displays an elbow where the timescale of relaxation shifts from the time expected from the viscous flow of fluid through the pores of the packing and a longer timescale which we hypothesize comes from a viscosity, η, of the packing itself.

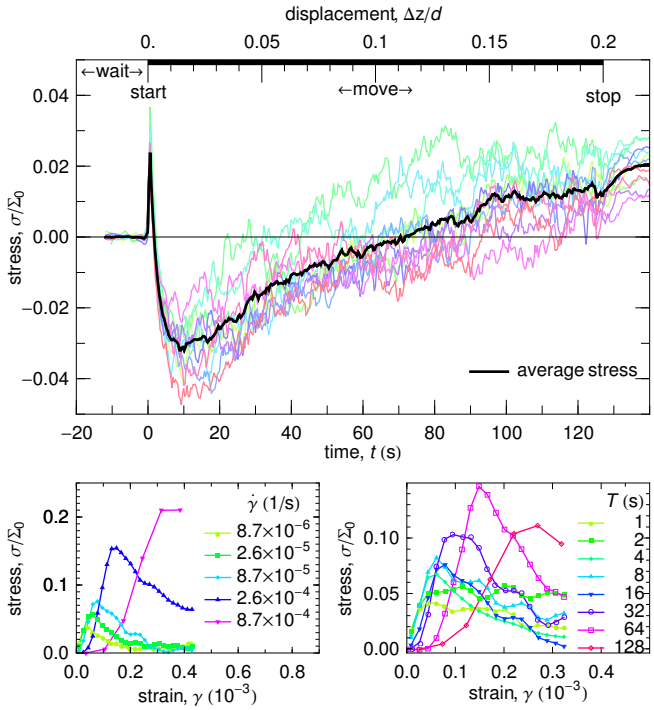

Figure 3.4: Response of the sedimented packing to constant velocity motion of the shear plane. Top panel: the upper horizontal axis shows the constant-strain-rate protocol, with the imposed strain rate jumping from zero to $\dot{\gamma} = v/W = 8.7 \times 10^{-5}/\mathrm{s}$ at time, $t = 0$, and stopping at a displacement of $z = 0.2\,d$. The light lines are individual shear stress responses (system width, $W = 18\,d$). Yielding is characterized by a sharp stress peak at small strain. The bottom panels show run-averaged stresses near yielding at fixed waiting time, $T = 16\,\mathrm{s}$ (bottom left), and at fixed strain rate, $\dot{\gamma} = 8.7 \times 10^{-5}/\mathrm{s}$ (bottom right).

panel of Fig. 4 correspond to the same sedimentation processes followed by an applied rapid sinusoidal perturbation intended to fluidize and compact the packing. After the perturbation ended, the packing was allowed 600 s to settle and age before commencing the constant strain rate test. Because sedimentation takes longer than settling after compaction, these two protocols translate into different wait times which we can estimate from the location of the elbow in Fig. 3.3. In Fig. 3.6 where we are only trying to show strain rate scaling, no estimation of the age was needed.

3.4 Results and Discussion

In Fig. 3.4 (top panel) we show an example of the stress response to a small strain rate at the lowest volume fraction, ϕ_0. The stress increases as soon as the strain is initiated but then peaks and falls sharply beyond a very small strain of order 10^{-5} to 10^{-3} in the experimental regime studied. Because strains are so small, resolution is limited in determining the shape of the stress-strain relation before this peak, however, the relation appears to become nonlinear when the peak is large. The peak value of σ in Fig. 3.4 is taken to be the yield stress, σ_y, and is the main focus of this dissertation. Furthermore the yield stress, σ_y, is a function of the applied strain rate, $\dot{\gamma}$, and of the waiting time, T, as shown in Fig. 3.4 (lower panels).

One of our principal results is that the yield stress, σ_y, collapses onto a master curve displaying power-law scaling over six decades in $\dot{\gamma}\,T$, as shown in the main panel of Fig. 3.5. The data collapse includes data for two different widths of cell, W, and two different fluids. The yield stress collapses even though the fluids differ in viscosity by a factor of 20. Thus the yield stress arises from solid stresses in the packing; the surrounding fluid is irrelevant in this small strain regime except for its contribution to the buoyant weight accounted for in the static load, Σ_0. As shown in Fig. 3.5, a least squares fit on logarithmic axes to

$$\sigma_y/\Sigma_0 = C \cdot (\dot{\gamma}\,T)^n \tag{3.4.1}$$

gives parameter estimates of, $n = 0.30(1)$, and $\log_e C = -0.6(1)$. No lower cutoff is observed, suggesting that a quasistatic reversible elastic regime is not experimentally accessible.

In the main panel of Fig. 3.6, we show that the strain-rate scaling of σ_y is preserved when the volume fraction, ϕ, is varied away from the loosest packing. Increasing volume fraction by $\Delta\phi$ above ϕ_0 results in identical scaling of the yield stress with the exponent fit to $n = 0.33(1)$. The absence of volume fraction dependence in the

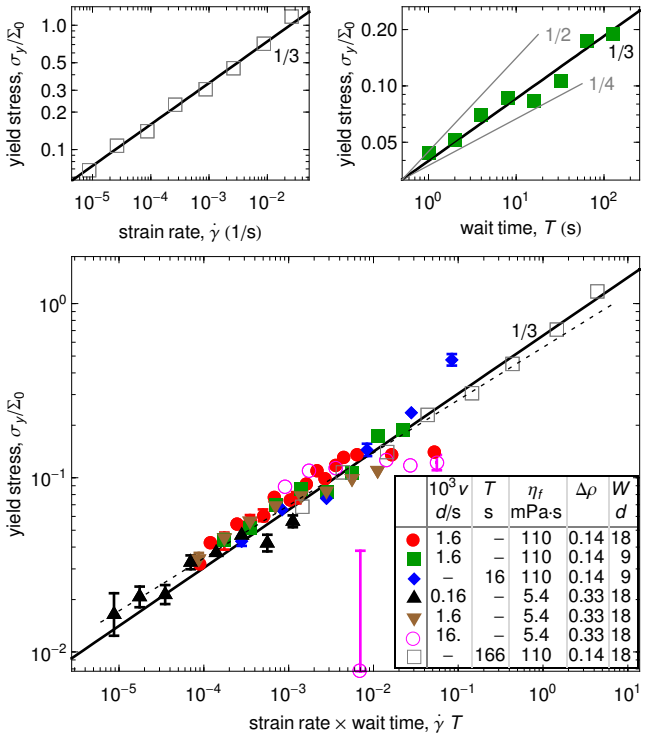

Figure 3.5: Power law scaling of the shear yield stress. The top panel shows examples of the scaling of the yield stress against strain rate and wait time, both displaying exponents near 1/3. The primary subfigure shows yield stress from experiments across a variety of rates, v, fluid viscosities, η_f, density mismatches, $\Delta\rho = 1 - \rho_f/\rho_s$, and system widths, W, collapsed onto a master curve against the dimensionless product of strain rate and wait time. The wait time represents the age of the packing and is set by a pause of duration, T, following a brief fluidization except in the open squares where it is calculated from the end of sedimentation (see top-right Fig. 3.1). This master curve exhibits a power-law dependence over a six-decade span with exponent fit by least squares to 0.30(1) (dashed line, excludes the single outlier). Error bars display the statistical error in the median.

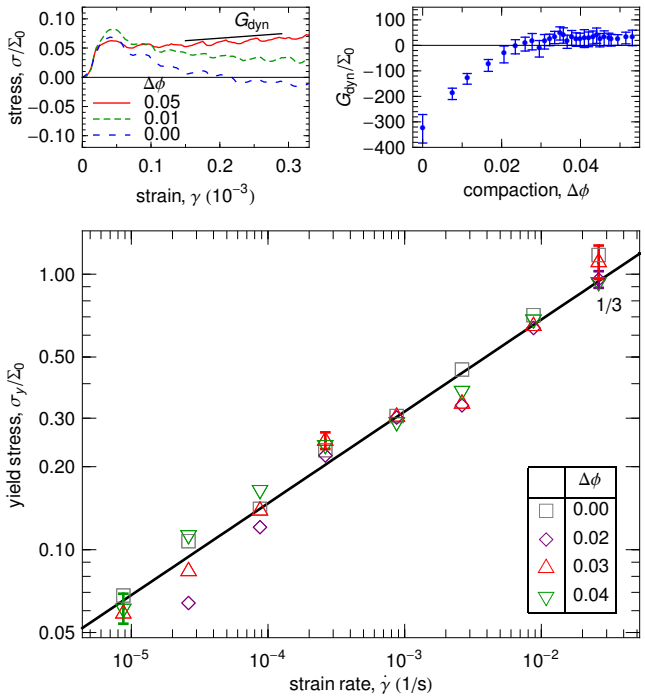

Figure 3.6: Power law scaling of the yield stress at varying degrees of compaction, $\Delta\phi$. The top panel displays the stress response for different levels of compaction ($\dot{\gamma} = 8.7 \times 10^{-5}/\mathrm{s}$, $T = 4\,\mathrm{s}$, $W = 18\,d$, $\eta_f = 110\,\mathrm{mPa}\cdot\mathrm{s}$). The response below the yield stress varies little with compaction while the dynamic slope immediately post-yield, G_{dyn}, increases, ultimately changing sign. The main figure shows that the power-law scaling of the yield stress with strain rate of freshly sedimented and compacted packings is unchanged by the degree of compaction. A least squares fit gives an exponent of 0.33(1), consistent with $\sigma_y \propto \dot{\gamma}^{1/3}$.

stress-strain response up to and including the yield stress demonstrates a lack of sensitivity of the solid near RLP to variations in volume fraction. This stands in contrast with solid mechanics near RCP where elastic moduli, for instance, display critical scaling with the distance to ϕ_{RCP} [65]. The insensitivity to volume fraction near RLP, however, appears to be confined to the solid regime. After yielding has occurred, volume fraction dependence reappears in the dynamic modulus, G_{dyn} (top-right Fig. 3.6).

To place into context our result of cube-root scaling of the yield stress with $\dot{\gamma}\,T$, we note that age and rate dependence have been observed in static yield stresses and static friction coefficients in granular systems. However, logarithmic or much smaller exponents are typically reported [55, 69, 50, 17]. The relatively large exponent of 1/3 and the symmetry between age and rate are new observations near the RLP limit, with the only comparable rate-scaling having been reported in a colloidal paste [31]. Aging of interparticle contacts are a possible source of age and rate-strengthening, but the logarithmic (and occasionally small-power-law) forms of friction and plasticity reported for PMMA are much slower than the cube-root scaling of Equ. 3.4.1 [96, 12, 8, 15, 76].

Figs. 3.7 and 3.8 show examples of the difference between the reported age and rate-scalings of the static friction coefficient [15] and the yield stress of PMMA [12] and the scaling we are describing for the yield stress. In both cases the data appear at least as linear on log-log axes as on log-linear axes (as published) indicating that the 2 to 3 decades of the independent variable are not sufficient to distinguish logarithmic from power law behavior for such small exponents. We include the larger exponent of 1/3 to make clear how much larger it is in practice than these exponents and also that a 3-decade range in the independent variable is more than sufficient to distinguish a relatively large exponent like 1/3 from a logarithm.

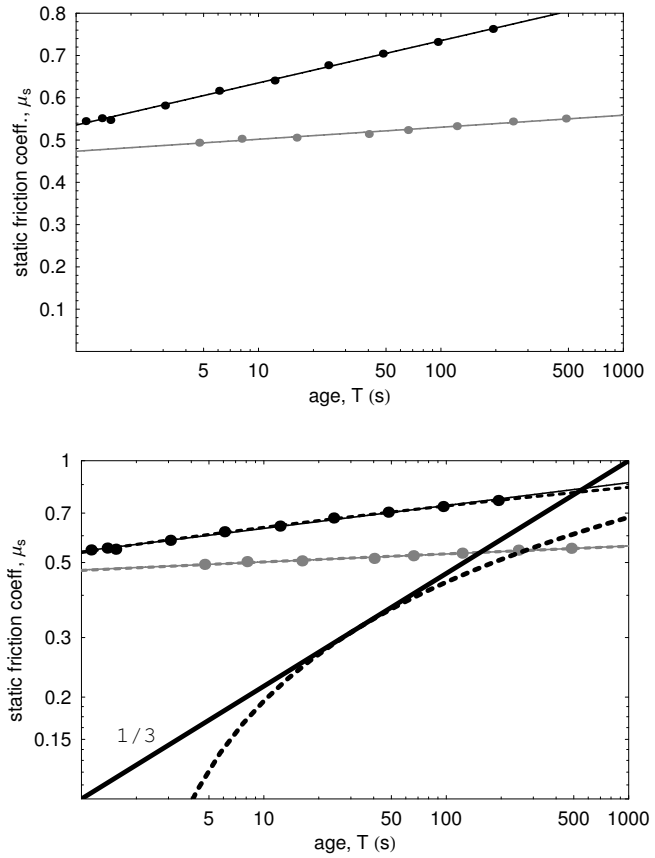

Figure 3.7: Data from Ref. [15] Fig. 4(a) showing the increase in static friction coefficient of PMMA with contact time, T. Gray markers are at 293 K, black markers at 345 K. The upper figure plots the data as it is plotted in Ref. [15] which highlights the logarithmic age dependence of the friction coefficient. The lower figure replots the data on log-log axes as one would to highlight power law scaling. This lower figure displays solid lines showing the best power-law fit and dashed lines showing the best semilog fit. That these power-law and semilog fits nearly overlay demonstrates that a 4-decade span in the independent variable is insufficient to distriguish power-law from semilog behavior given such small exponents (best fits are 0.028(2) and 0.099(2)). To demonstrate how different the above behavior is from the $\approx 1/3$-power law forms seen in our dissertation, we've drawn a dark line with slope 1/3. The dashed curved line tangent to it is the logarithm that best approximates a power law of 1/3 over this span.

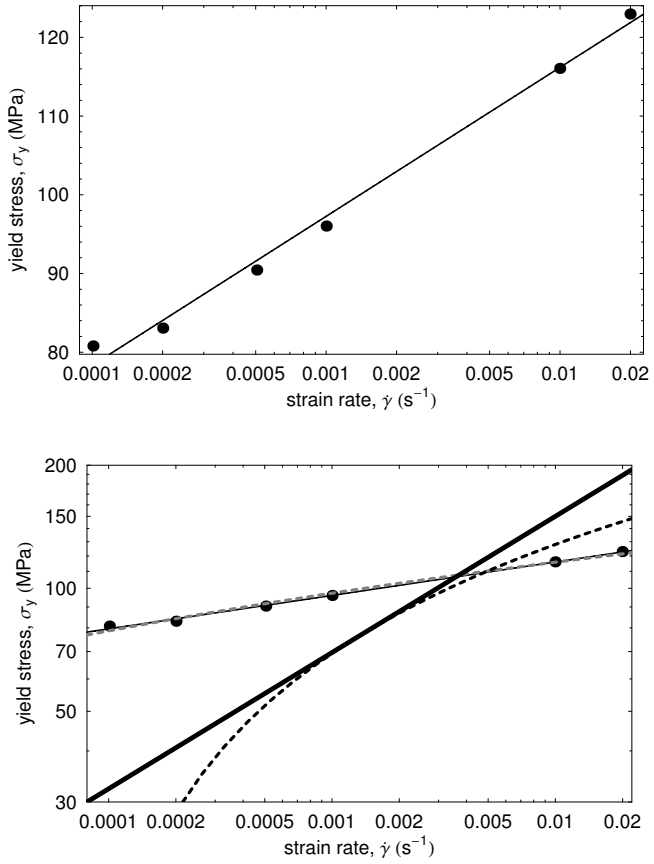

Figure 3.8: Data from Ref. [12] Fig. 4(a) showing the increase in yield stress of PMMA with strain rate, $\dot{\gamma}$. The upper figure replots the data with strain rate on a logarithmic scale highlighting that these data are fit well by a logarithmic form. The lower figure plots the data as it appeared in Ref. [12] on log-log axes as one would to highlight power law scaling. The black straight-line fit through the data has slope 0.082(2). The dashed gray line which is the best semi-log fit to the data is also shown and it's curvature is barely discernible, again suggesting the futility of distinguishing between logarithmic and power law forms for this particular data series. To show how different these forms are from the $\approx 1/3$-power law seen in our dissertation, I've drawn a dark line with slope 1/3. The dashed curved line tangent to it is the logarithm that best approximates a power law of 1/3 over this span.

A simple way to express the difference between the exponents expected for rate scaling and those presented here is with the magnitude of change expected. The yield stress of PMMA is consistent with power law scaling [12], with exponent 0.082, however, over the span of rates in Fig. 3.8, the yield stress of PMMA increases by about 60% while the yield stress of our loose packings scaling with an exponent of 1/3 would vary by almost 7-fold over the same span. If contact aging is important, it would appear that it must be amplified by the network of granular contacts.

3.5 Extended Maxwell Model of Viscoelasticity

The Maxwell model of viscoelasticity provides a simple way of describing the rheology of materials that exhibit an elastic response at short timescales yet creep over long timescales. In its 1-dimensional form, the Maxwell model consists simply of a viscous damping element, $\sigma_\eta = \eta \cdot \dot{\gamma}$, in series with a elastic spring, $\sigma_G = G \cdot \gamma$, where G is the shear modulus of the material at high frequency, and η is the dynamic viscosity at low frequency. Because the elements are in series, stresses are equal in both elements, $\sigma = \sigma_G = \sigma_\eta$, and strains add, $\gamma = \gamma_G + \gamma_\eta$, thus the model evolves according to the following differential equation:

$$\dot{\gamma} = \frac{\dot{\sigma}}{G} + \frac{\sigma}{\eta} \, . \tag{3.5.1}$$

This model is a promising starting point for describing the mixed fluid and solid nature of loose packings, however it contains no aging mechanism, predicts linear growth rather than the logarithmic [62] creep of the strain, and is unable to describe the cube-root yield-stress scaling presented in this chapter.

Some prior attempts to model the rheology of loose granular materials have sought to extend the Maxwell model of viscoelastic flow by allowing the viscous element, η, to evolve in time [30, 31, 62]. Nguyen et al. were able to describe the logarithmic

creep that they observed under constant stress conditions with a model where the evolution of η depends on strain history [62]:

$$\dot{\gamma} = \frac{\dot{\sigma}}{G} + \frac{\sigma}{\eta} \tag{3.5.2a}$$

$$\frac{\dot{\eta}}{G} = a - r\left(\frac{\dot{\gamma}\,\eta}{G}\right)^2 \quad . \tag{3.5.2b}$$

In this model aging and rejuvenation are tuned by positive dimensionless constants a and r. The aging, a-term leads to linear growth in η when the material is at rest. Thus the initial viscosity, $\eta(0)$, at time, $t = 0$, arises from integrating Eq. 3.5.2b over the aging or waiting period of duration, T, during which $\dot{\gamma} = 0$,

$$\int_{-T}^{0} \dot{\eta}/G\, dt = \int_{-T}^{0} \left(a - r\left(\frac{\dot{\gamma}\,\eta}{G}\right)^2\right) dt \tag{3.5.3a}$$

$$\eta(0) = a\,G\,T + \eta(-T) \approx a\,G\,T \tag{3.5.3b}$$

where the last approximation assumes that the system was well fluidized at the start of the aging period and thus that $\eta(-T)$ is negligible. The rejuvenating, r-term fluidizes the packing during periods of large shear when the second order term in strain rate is significant. A lower order rejuvenation term does not appear in the expansion of $\dot{\eta}$ consistent with the notion that evolution of the viscosity should be a function of the magnitude and not the direction of strain.

Constant stress solutions of Eq. 3.5.2,

$$\eta(t) = a\,G\,\left(T + \left(1 - \frac{r}{a}\,(\sigma/G)^2\right)\,t\right) \tag{3.5.4a}$$

$$\gamma(t) = \frac{1}{a}\,\left(\frac{\sigma/G}{1 - \frac{r}{a}\,(\sigma/G)^2}\right)\,\log\left[1 + \frac{t}{T}\,\left(1 - \frac{r}{a}\,(\sigma/G)^2\right)\right] \tag{3.5.4b}$$

display the logarithmic creep that Nguyen et al. observed experimentally [62]. Constant strain-rate solutions are less interesting in this model, however, as evolution of

viscosity decouples from the evolution of the stress when $\dot{\gamma}$ is constant:

$$\frac{\dot{\eta}}{G} = a - r\left(\frac{\dot{\gamma}\,\eta}{G}\right)^2 \tag{3.5.5}$$

with solution,

$$\eta(t) = \sqrt{\frac{a}{r}}\,\frac{G}{\dot{\gamma}}\,\coth\left(\sqrt{\frac{a}{r}}\,\dot{\gamma}\,t + \coth^{-1}(\sqrt{\frac{a}{r}}\,\dot{\gamma}\,T)\right)\ . \tag{3.5.6}$$

This model, then, is less interesting at constant stress than it was at constant strain rate and it doesn't yield phenomena resembling the cube-root yield stress scaling of Eq. 3.4.1 as shown numerically in Fig. B.1.

We propose a different modification of the Maxwell model where we expand $\dot{\eta}$ to the lowest order in applied stress, σ, consistent with symmetry:

$$\dot{\gamma} = \frac{\dot{\sigma}}{G} + \frac{\sigma}{\eta} \tag{3.5.7a}$$

$$\frac{\dot{\eta}}{G} = a - r\left(\frac{\sigma}{G}\right)^2, \tag{3.5.7b}$$

where positive dimensionless constants a and r set the strengths of aging and rejuvenation. This new model turns out to be equivalent to Nguyen et al.'s model (Eq. 3.2.2) when stress is held constant because at constant σ, Eq. 3.5.7a, reduces to $\sigma/G = \dot{\gamma}\,\eta/G$—the difference in the r-terms in the models. This new model thus admits the same logarithmic creep solution (Eq. 3.5.6) and is therefore consistent with Nguyen et al.'s experimental findings and analysis at constant stress.

It is possible to calculate approximate scalings of the yield stress in this new model. The following provides a quick sketch of the calculation to show how the cube-root scaling emerges. Section B.1.1 in the Appendix includes an explicit power-series solution which provides a justification for the approximations used here.

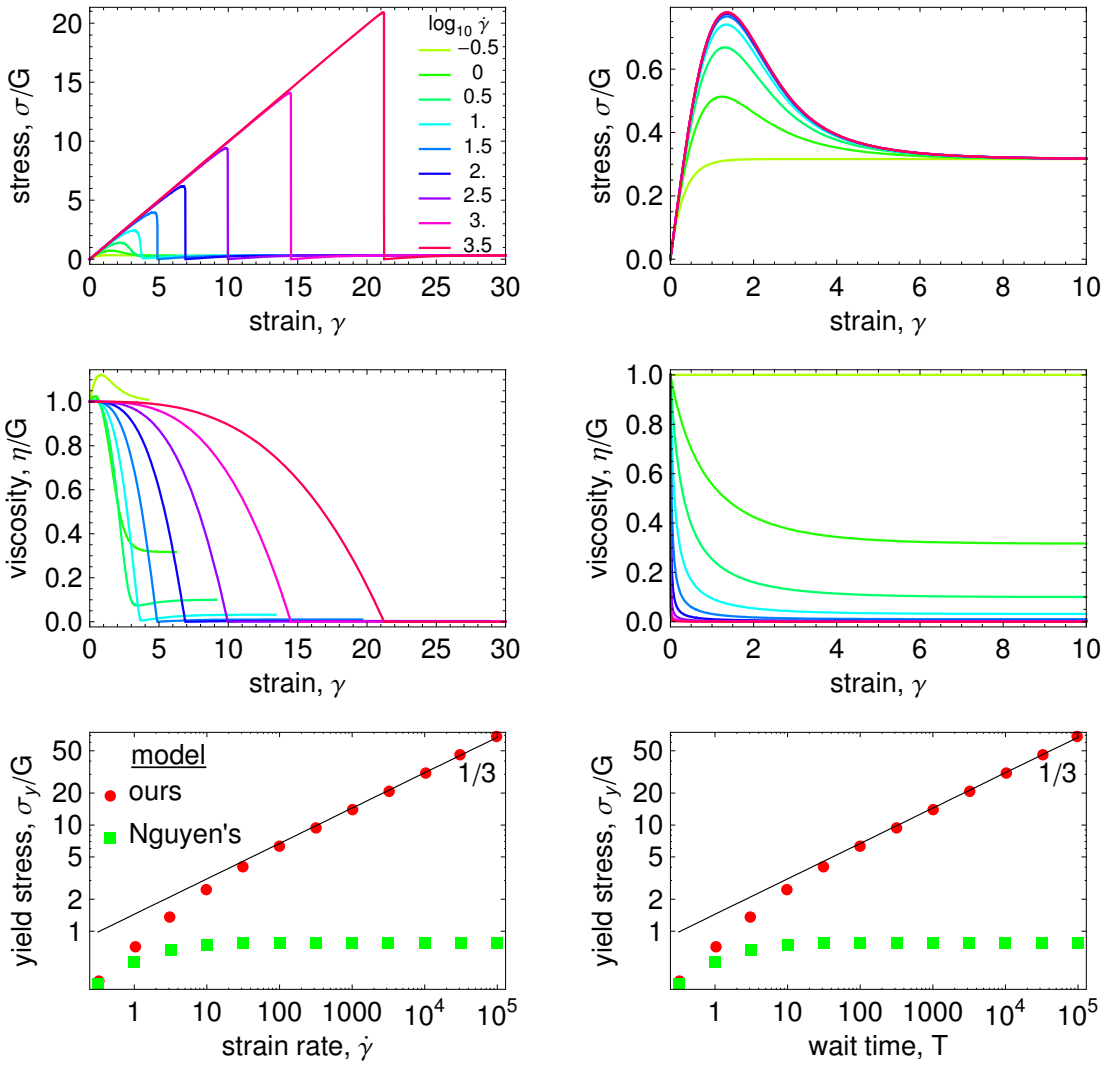

Figure 3.9: Numerical solutions for our model (left column) and Nguyen et al.'s model [62] (right column). The top four figures show numerical solutions for different rates, $\dot{\gamma}$ and the bottom row shows numerical solutions for the scaling of the height of the stress maxima, σ_y, versus strain rate, $\dot{\gamma}$, for our model (red circles) and Nguyen et al.'s model (green squares). The values of the fixed parameters are $a = 0.1$, $r = G = 1$, $T = \dot{\gamma} = 10$, $d = 1 \times 10^{-6}$. The extreme similarity between the rate and age-scaling subfigures is not a mistake: in constant strain rate solutions of both models, the shape of stress-strain curves depend only on the product of $\dot{\gamma}T$. Our model matches the approximate scaling of Eq. 3.4.1 (black lines) when $\dot{\gamma}T$ is large.

We see from numerics (Fig. 3.9), that when a constant strain rate is first applied solutions for $\sigma(t)$ rise from zero, peak then fall. In this limit where the peaks are large, we see that the response is initially quite linear with a sharp sawtooth-shaped peak. If the aging parameter, $a \sim 1$ (which it appears to be from the ≈ -1 exponent in relaxation, Sect. 4.3.3), we will show that in the limit where $\sqrt{r}\,\dot{\gamma}\,T$ is large, that the cube-root scaling of the height of this peak, σ_y, emerges.

The simple sawtooth shape of σ in the large peak limit suggests a scheme for calculating the approximate scaling of the stress maxima. Approximating stress as linear in time, we obtain an approximate solution for $\eta(t)$ then solve for the time, t_y, when these solutions satisfy the relation implied by Equ. 3.5.7a evaluated at peak stress.

The initial stress-response is linear,

$$\sigma(t) \approx G\,\dot{\gamma}\,t\ . \tag{3.5.8}$$

Solving Eq. 3.5.7b using the linear approximation of σ gives

$$\dot{\eta}/G \approx a - r\,t^2\,\dot{\gamma}^2 \tag{3.5.9a}$$

$$\eta(t)/G \approx a\,(t+T) - \frac{1}{3}\,r\,t^3\,\dot{\gamma}^2 \tag{3.5.9b}$$

where we have used initial condition $\eta(0) = G\,a\,T$ (Eq. 3.5.3b) as aging is the same in the new model.

We now look at behavior at the stress peak. At the time, t_y, of peak stress $\dot{\sigma}(t_y) = 0$ so the Maxwell model (Eq. 3.5.7a) gives

$$\sigma(t_y) = \dot{\gamma}\,\eta(t_y)\ . \tag{3.5.10}$$

As the linear behavior appears to extend right up to the peak in the limit where peaks are large, we attempt to estimate t_y by plugging the small-t approximate solutions

of $\sigma(t)$ (Eq. 3.5.8) and $\eta(t)$ (Eq. 3.5.9b) into this relation which is valid at the peak, yielding

$$T = \left(3\,(1-a)\,t_y + r\,\dot{\gamma}^2\,t_y^3\right)/(3\,a)\ . \tag{3.5.11}$$

As the power-series solution Appendix B.1.1 makes clear, the small parameter in these expansions is t_y/T so using the scaling we are about to derive and assuming $a \sim 1$, it can be shown that the first order term in t_y is small compared to the other two terms (note that the power-series calculation also explains why we are justified in approximating $\sigma(t)$ to first order in t while we calculate $\eta(t)$ to third order). Neglecting the first order term in t_y, the cube-root strain-rate and age scalings follow.

$$t_y \approx \left(\frac{3\,a\,T}{r\,\dot{\gamma}^2}\right)^{1/3} \tag{3.5.12a}$$

$$\gamma_y \approx \left(\frac{3\,a\,T\,\dot{\gamma}}{r}\right)^{1/3} \tag{3.5.12b}$$

$$\sigma_y \approx G\,\left(\frac{3\,a\,T\,\dot{\gamma}}{r}\right)^{1/3}\ . \tag{3.5.12c}$$

Thus this natural extension of the Maxwell model produces the cube-root power-law scalings seen in the experiment and may be relevant to other systems [31, 74]. Eliminating $\dot{\gamma}$, we see that these cube-root strain-rate scalings are equivalent to reciprocal-square-root scaling with yield time:

$$\sigma_y \approx G\,\left(\frac{3\,a\,T}{r\,t_y}\right)^{1/2} \tag{3.5.13a}$$

$$\gamma_y \approx \left(\frac{3\,a\,T}{r\,t_y}\right)^{1/2}\ . \tag{3.5.13b}$$

The Maxwell model can be generalized to the case where the elastic element follows an arbitrary power-law potential (see Sect. B.1.2),

$$U(\gamma) = \frac{1}{\alpha}\,G\,|\gamma|^{\alpha}\ , \tag{3.5.14}$$

In this case the Maxwell model of Eq. 3.5.7a becomes

$$\dot{\gamma} = \mathrm{sgn}(\dot{\sigma}) \left(\frac{|\dot{\sigma}|}{(\alpha - 1)\, G\, t^{\alpha - 2}} \right)^{\frac{1}{\alpha - 1}} + \frac{\sigma}{\eta} \tag{3.5.15}$$

and a very similar scaling argument (see Sect. B.1.3) gives the scaling:

$$t_y \approx \left(\frac{a\,(2\,\alpha - 1)\,T}{r\,\dot{\gamma}^{2\,(\alpha - 1)}} \right)^{\frac{1}{2\,\alpha - 1}} \tag{3.5.16a}$$

$$\gamma_y \approx \left(\frac{a\,(2\,\alpha - 1)\,\dot{\gamma}\,T}{r} \right)^{\frac{1}{2\,\alpha - 1}} \tag{3.5.16b}$$

$$\sigma_y \approx G \left(\frac{a\,(2\,\alpha - 1)\,\dot{\gamma}\,T}{r} \right)^{\frac{\alpha - 1}{2\,\alpha - 1}} \quad . \tag{3.5.16c}$$

These scalings reduce to the cube-root power law when the potential is harmonic and give σ_y depending on $\dot{\gamma}\,T$ to exponents of 3/8 for Hertzian, 2/5 for cubic and 3/7 for quartic potentials suggesting that higher-order elasticity terms may well explain exponents from ~ 0.33 to ~ 0.43.

Interestingly, the reciprocal square root scaling of yield stress with yield time (see Equ. 3.5.13a),

$$\sigma_y \approx G \left(\frac{(2\,\alpha - 1)\,a\,T}{r\,t_y} \right)^{\frac{1}{2}} \tag{3.5.17a}$$

$$\gamma_y \approx \left(\frac{(2\,\alpha - 1)\,a\,T}{r\,t_y} \right)^{\frac{1}{2(\alpha - 1)}} \quad , \tag{3.5.17b}$$

is independent of the degree, α, of the potential.

The model of Eq. 3.5.7 unifies the seemingly unrelated responses observed to constant-strain-rate (Eq. 3.4.1) and constant-stress loading [62]. It explains the initial solid-like response to constant strain-rate loading because aging can render η large enough to give approximately linear response until $\sigma = \sigma_y(\dot{\gamma},\, T)$ and rejuvenation triggers an abrupt transition from a large-η solid-like response to a small-η liquid-like

flow. It also explains creep flow in response to very small constant-stress loading, because the range of this approximately-linear regime vanishes as $\dot{\gamma}$ goes to zero, leaving nothing but a viscous response to small stresses applied over long timescales.

If it is generally true that $C \sim 1$ as in Eq. 3.4.1, then the only stress scale that contributes to the solidity of the packing is the external load, in this case the gravitational pressure, p. That no new intrinsic timescale needs to be introduced in Eq. 3.5.7 is consistent with the symmetry of the yield-stress scaling with strain rate and age and suggests that the mechanisms of aging and rejuvenation may be interdependent. Together with Eq. 3.5.12c, the observation that $C \sim 1$ implies such a constraint: $(a/r)^{1/3} \sim p/G$. This relationship could provide a clue as to the grain-level causes for the macroscopic phenomenology of aging and rejuvenation.

CHAPTER 4

RHEOLOGY AT LARGER STRAINS

4.1 Introduction

The previous two Chapters deal with experimental protocols for the formation of loose packings and the mechanics of those states up to the point of initial failure. In the present chapter, we investigate mechanical behavior when the material is subjected to larger strains.

The expected response to steady-state shear may be the Herschel-Bulkely (H-B) stress-scaling reported in many related systems [44, 7, 94, 52, 14, 26, 73],

$$\sigma_{\text{H-B}} = \sigma_c \left(1 + (\dot{\gamma}/\tau_{\text{H-B}})^n\right) . \tag{4.1.1}$$

However experiments poking [80] and shearing [60] loose-packed fluidized beds of glass spheres have described a rate-independent steady-state shear regime.

With regard to statics, simulations have measured the bulk modulus at ϕ_{RLP} [85] and experiments have reported logarithmic creep under constant-stress conditions [62]. Our experiments described in Chapter 3 were the first to look at the response of loose packings to the startup of constant strain rate shear. They show that the yield strength scales as the cube-root of strain rate and the age of the material.

The rate-scaling of the yield stress and the existence of creep at small loads, both imply that loose sphere packings lack a true static yield stress and thus are not fully solid. Nguyen et al. suggest that the mixed solid–fluid nature of sphere packings near RLP may be captured by a generalization of the Maxwell fluid model of a elastic solid

in series with an evolving viscous element. In the previous chapter, we showed that a modification of their model reconciles their observation of logarithmic creep with our observation of cube-root scaling of the yield stress:

$$\dot{\gamma} = \frac{\dot{\sigma}}{G} + \frac{\sigma}{\eta} \tag{4.1.2a}$$

$$\frac{\dot{\eta}}{G} = a - r\left(\frac{\sigma}{G}\right)^2, \tag{4.1.2b}$$

This model, however, cannot describe steady-state flows like Herschel-Bulkley (Eq. 4.1.1) that possess strain-rate dependencies. Because it includes no timescales beyond those imposed by the initial viscosity and the strain rate, there is no timescale that can dimensionally balance $\dot{\gamma}$ when the initial viscosity is no longer relevant. Thus a new timescale must be introduced into the model if it is to describe any $\dot{\gamma}$-dependence of shear response at long times.

In this chapter, we report experiments on loose sphere packings observing mechanical phenomena that occur after the yielding event. We track several features of the stress response to the onset of constant rate shear strain including the shape of the growth of stress beyond the yield point and the timescale of a sharp stress collapse immediately after the yield point. We find that this last behavior occurs only at volume fractions near ϕ_{RLP}. We also study relaxation at fixed strain of the material after it has been subjected to strains well beyond the yielding.

In these phenomena we see evidence of a new timescale, τ, that manifests first as the timescale of stress decline after the yielding event and later as the prefactor in power-law growth of stress at scales beyond the initial yielding event. We also see evidence of this timescale in the initial conditions of stress relaxation at constant strain. This timescale itself is found to depend on the applied strain rate and to scale differently in systems with low and high viscosity interstitial fluids.

We show that a simple generalization of Eq. 4.1.2 where the evolution of the viscous element, η, of a Maxwell fluid is expanded to lowest order in stress and the emergent timescale, τ, describes the initial shapes of these features and provides a framework for relating their strain-rate dependencies. We also demonstrate that this simple theoretical approach misses phenomena such as pronounced upward swelling of stress after a brief decline during relaxation at volume fractions near RLP as well as a shift in baseline stress causing the system to relax to higher than original stress levels.

4.2 Methods

The apparatus and protocols used in this chapter are the same as in Chapter 3. In many cases the data traces presented in that chapter are the small strain piece of longer traces presented here.

4.3 Results

4.3.1 Post-yield Stress Drop At Volume Fractions near RLP

At the lowest volume fraction, $\phi \approx 0.565$, there is a dramatic drop in the stress immediately following the yielding event that is not seen at the three higher volume fractions (Fig. 4.1). The post-yield drop feature at the lowest volume fraction is shown in Fig. 4.2 with the origin of time shifted to correspond with the yield time. The initial shape of the stress drop is an exponential decay with a timescale that depends on strain rate. In the high viscosity interstitial fluid, early behavior collapses cleanly when time is scaled by a timescale, $\tau \sim \dot{\gamma}^{-1/2}$ (the least-squares fit of the exponent is $-0.54(5)$). Similar $\dot{\gamma}$-scaling but with a smaller prefactor is seen when the system size is halved consistent with the timescale being proportional to the system width and, as the other dimensions are not varied, consistent with the timescale being proportional to the system size. However, when the system is prepared with a lower viscosity

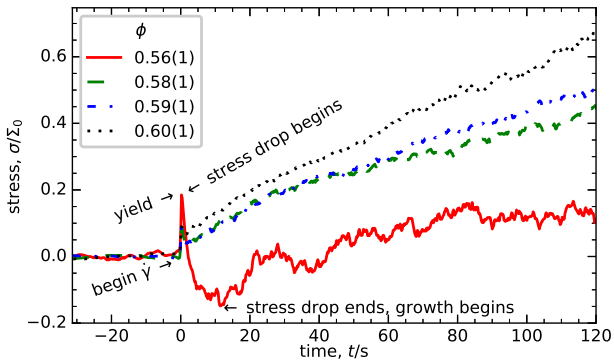

Figure 4.1: Examples of stress response to startup shear: ($\dot{\gamma} = 8.7 \times 10^{-5}$/s, $W = 18\,d$, $\eta_f = 110\,\mathrm{mPa}\cdot\mathrm{s}$, $T = 166\,\mathrm{s}$). At the lowest volume fractions, the stress response of the packing to an applied steady strain-rate shear displays the following features: 1) a sharp initial ("yield stress") peak (see Chapter 4.2), 2) an abrupt drop or "collapse" in stress immediately post-yield (see Fig. 4.2), and 3) the recovery of the stress after it bottoms out (see Fig. 4.3) The post-yield drop is less pronounced at volume fractions even 0.02 above ϕ_{RLP}.

interstitial fluid, the scaling is markedly different with stress at small times collapsing when the time axis is scaled against $\tau \sim \dot{\gamma}^{-1}$. The lower-viscosity system nearly follows a single stress-strain curve, $t/\tau \sim t/\dot{\gamma}^{-1} = \gamma$. That changing the viscosity of interstitial fluid changed the exponent and not the prefactor of the timescale is surprising. We do not understand either the role of the viscosity of the interstitial fluid nor what dimensionally balances the square-root strain-rate timescale in the higher-viscosity system.

No dependence on age is seen breaking the symmetry between age and strain-rate seen in behavior up to the yield stress (Chapter 3).

4.3.2 Stress Growth

Fig. 4.1 shows examples of the stress response to prolonged steady strains well beyond the yield point. At volume fractions near RLP there is a pronounced drop in stress immediately post yield after which the stress bottoms out and slowly grows

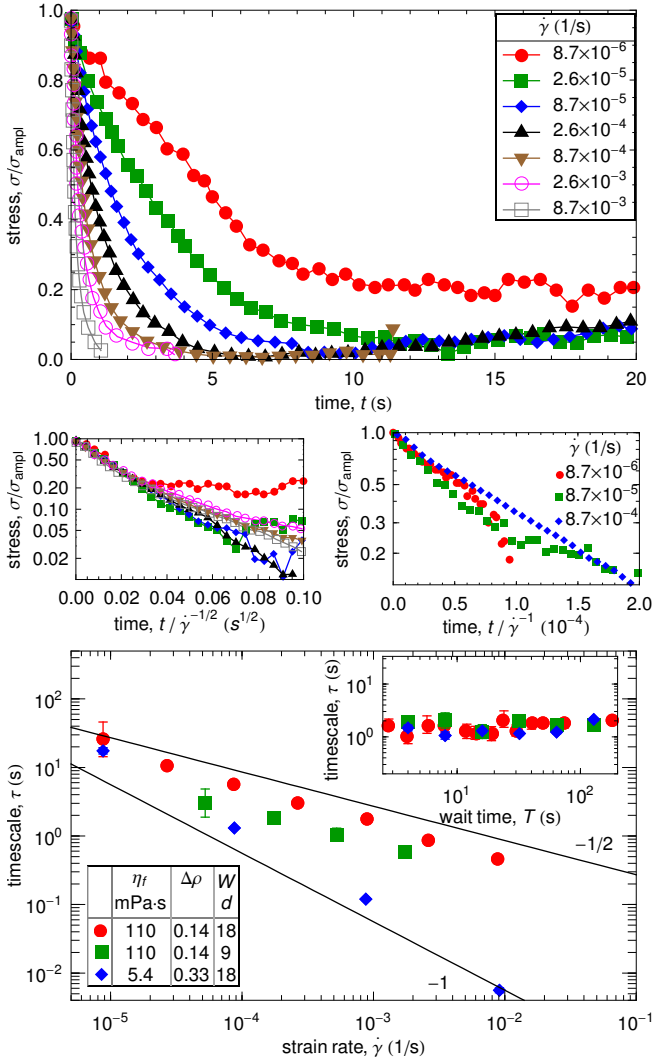

Figure 4.2: Drop in stress immediately following the yield event and associated timescales at the lowest volume fraction ($\phi \approx 0.565(5)$). The top figure shows the drop in stress after the yielding event with the time zeroed at yield time and stress scaled by the amplitude of the drop in stress (corresponds to red dots in lower figure). Middle-left: these same data collapse against the timescale, $\tau \sim \dot\gamma^{-1/2}$. Middle-right: repeated in a thinner fluid (blue diamonds in lower figure), the timescale scales differently, closer to $\tau \sim \dot\gamma^{-1}$. The bottom figure plots the timescales from exponential fits to the first half-decade in stress for the above data sets and an additional dataset run at half of the system width (green squares). The inset shows that these timescales do not dependent on wait time ($\dot\gamma = 8.7 \times 10^{-5}$ /s for $W = 18\,d$ and $\dot\gamma = 1.7 \times 10^{-4}$ /s for $W = 9\,d$).

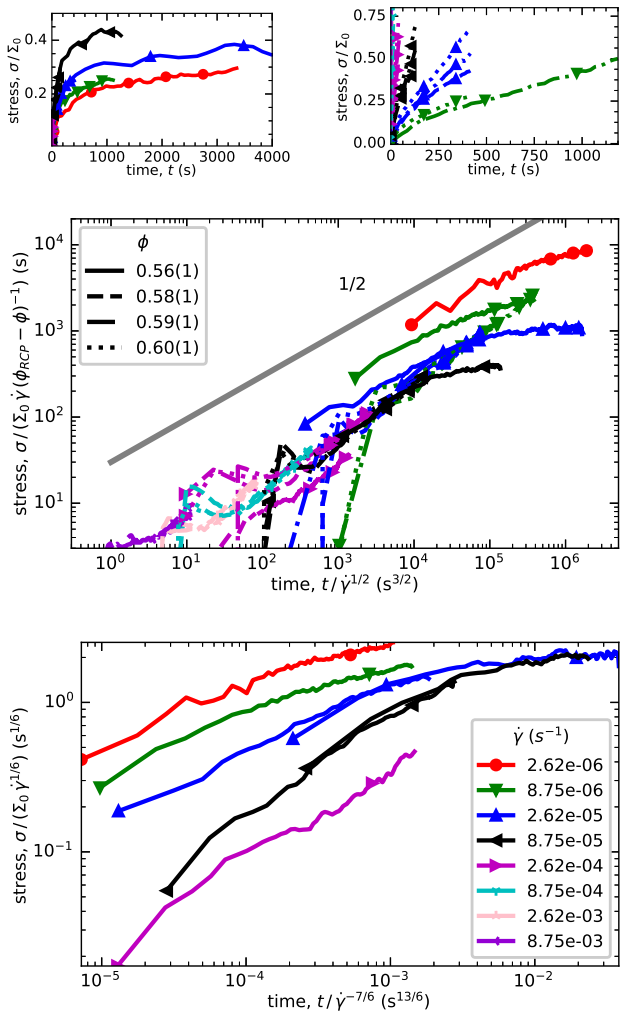

Figure 4.3: Growth of stress post-yield: The top panel shows the growth of stress at the lowest volume fraction, $\phi \approx 0.565(5)$, (left) and higher volume fractions (right) ($W = 18\,d$, $\eta_f = 110\,\mathrm{mPa}\cdot\mathrm{s}$). The lowest volume fraction exhibits a sharp drop in stress immediately post-yield (see Fig. 4.1) so the origin is set at the stress minimum. The origin is not moved for other volume fractions. Middle: axes are scaled as our model predicts for early growth of the stress. Note that the time-axis is *multiplied* by the same $\tau \sim \dot{\gamma}^{-1/2}$ that emerged as the timescale in post-yield stress drop. The normalization of the stress by the distance from RCP is purely empirical. The data mostly collapse onto a master curve with slope close to the predicted square-root although the slowest traces at the lowest volume fraction (solid lines) which show evidence of beginning to plateau do not collapse. Bottom: Data for the lowest volume fraction, plotted with axes scaled as predicted approaching the long-term steady-state. This appears to collapse at long times the traces that failed to collapse under the growth scaling. Both legends apply to the all sub-plots in this figure.

upward again. At volume fractions even 0.02 above ϕ_{RLP}, this drop is much less pronounced.

Plotted on log-axes in Fig. 4.3, on larger scales than the early "yield stress" peak, the stress appears to grow initially as a power-law in time, $\sigma \sim t^n$ with exponent $n \approx 1/2$, consistent with the square-root prediction of our model in Sect. 4.4.2.3. These data traces being relatively straight lines on log-log axes especially at the higher volume fractions, there is necessarily an interdependence in the scalings used to collapse the horizontal and vertical axes (power-law data with exponent 1/2 that collapse against $\sigma/\dot{\gamma}^m$, $t/\dot{\gamma}^n$ will also collapse against $\sigma/\dot{\gamma}^{m+k}$, $t/\dot{\gamma}^{n+2\,k}$ for any k). This being noted, in Fig. 4.3 we have scaled the axes to test consistency with the predictions of rheological model, Eq. 4.4.5, which we will lay out in Sect. 4.4.2.3. During the early power-law growth phase, this entails scaling time by $\dot{\gamma}^{1/2}$, *multiplying* time by the timescale, $\tau \sim \dot{\gamma}^{-1/2}$, that we had previously *divided* by when collapsing the data during the post-yield drop in stress. This difference in the roles of τ speaks to different physics of the two phenomena: the stress-drop occurs over a characteristic timescale, τ, while growth appears to be scaleless with τ entering as a unit of time.

The choice of scalings for the lowest volume fraction data are complicated by differing predictions for the early power-law growth of stress and the approach to a long-time, steady-state. The middle figure in Fig. 4.2 shows that stress at all volume fractions and strain rates except for the traces at the lowest volume fraction which are beginning to plateau collapse well when scaled for growth. These same lowest volume fraction traces, however, show promise of collapsing (bottom Fig. 4.2) under the scaling predicted approaching steady-state. Unfortunately we do not have longer traces at the lowest values of strain rate.

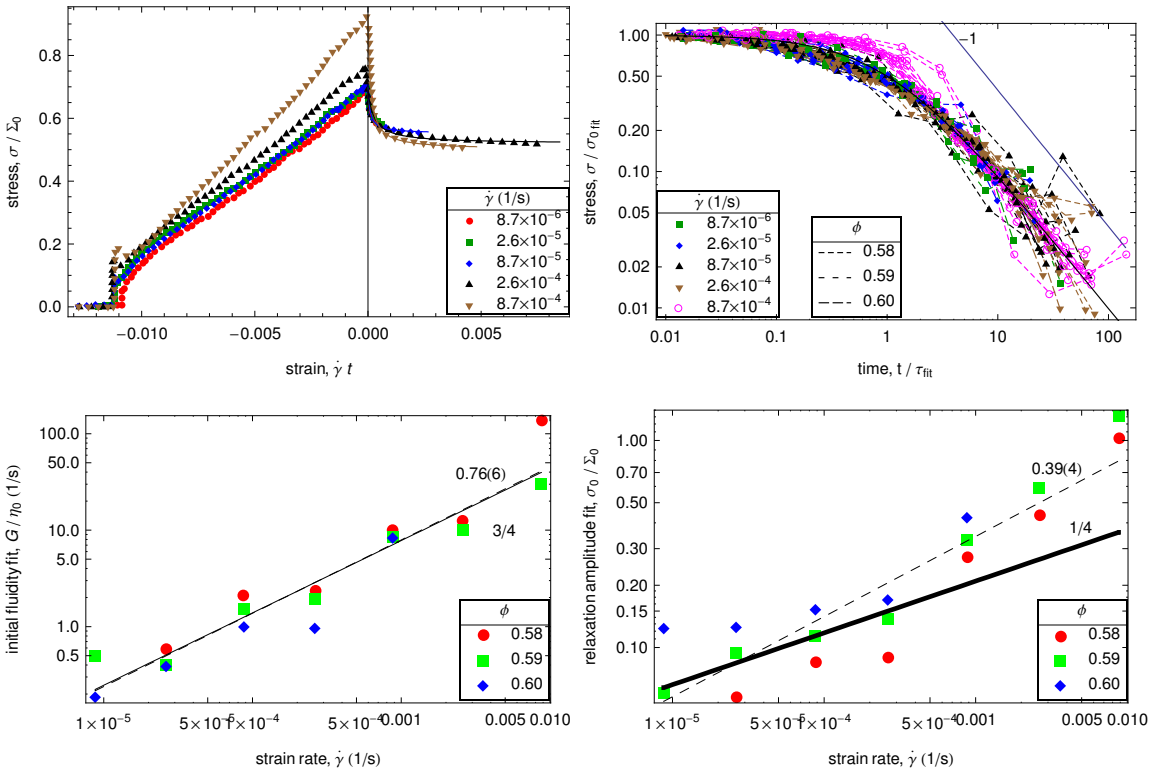

Figure 4.4: Relaxation at constant strain for $\phi \approx 0.58, 0.59, 0.60$. Top panel: stress-strain curves with the origin of time zeroed at the cessation of applied strain ($W = 18\,d$, $\eta_f = 110\,\mathrm{mPa}\cdot\mathrm{s}$). The top left shows examples of relaxation at $\phi \approx 0.60$ which are representative of volume fractions $\phi \approx 0.58$ to 0.60. The stress relaxes monotonically downward toward a new stress baseline that is not a function of $\dot{\gamma}$. Solid lines are least-squares fits to $\sigma = \sigma_0\,(1 + G\,t/\eta_0)^{-1} - \sigma_\infty$. Top right: When time and stress are scaled by the fit parameters, of initial stress, σ_0, and initial timescale, $\tau_{\mathrm{fit}} = \eta_0/G$, the stress relaxation curves collapse onto master curve, $(1+t)^{-\alpha}$, with exponent $\alpha \approx 1$. Bottom panel: The fit values themselves scale with strain rate. The initial timescale, $\tau_{\mathrm{fit}} = \eta_0/G$ scaling $\sim \dot{\gamma}^{-3/4}$ (left) and $\sigma_0 \sim \dot{\gamma}^{1/4}$ (right) for small $\dot{\gamma}$ where the σ_0 is also small. The exponents are consistent with the scalings of stress growth at higher volume fractions presented in Fig. 4.3 and the solution for stress-relaxation at small σ in Sect. 4.4.2.4.

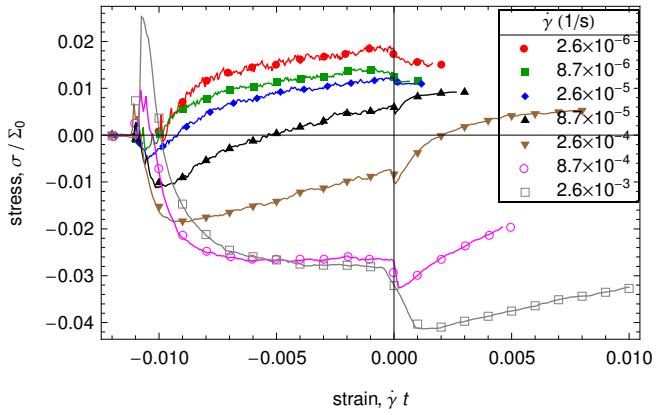

Figure 4.5: Stress relaxation near RLP: Relaxation is qualitatively different at the lowest volume fraction, $\phi \approx 0.565$, with the stress swelling upward after an initial drop. A constant strain rate, $\dot\gamma$, applies a total strain $\Delta\gamma = 0.2\,d/W \approx 0.011$, terminating at $t = 0$, after which $\dot\gamma = 0$ and the stress relaxes ($W = 18\,d$, $\eta_f = 110\,\mathrm{mPa}\cdot\mathrm{s}$). The size of the post-yield collapse in stress varies so much with strain rate that while the lower strain rate curves were growing, even plateauing when the applied strain ceases, the highest strain rates are still decreasing when the period of relaxation begins. Thus the relaxation curves which begin at $t = 0$ represent relaxation from disparate array of initial conditions.

4.3.3 Relaxation

Another interesting quantity is the evolution of stress under the condition of fixed strain. We observe that when our constant-strain rate measurements are completed having applied a fixed strain, $\Delta\gamma$, that the stress relaxes.

At volume fractions above RLP ($\phi \approx 0.58$ to 0.60) this relaxation resembles that of a simple Maxwell fluid with stress tending monotonically downward (Fig. 4.4) only the relaxation is much slower than an exponential decay and the asymptotic value is higher than the initial stress baseline. We find that this relaxation is well fit by the functional form, $\sigma = \sigma_0\,(1 + a\,G\,t/\eta_0)^{-1/a} + \sigma_\infty$, an equation that arises as a small-stress solution to the extended Maxwell model as outlined in Sect. 4.4.2.4. The data suggest that a is very nearly one and the fit parameters which amount to the initial stress, σ_0, and the initial relaxation timescale, η_0/G, themselves scale with $\dot\gamma$ as see in the stress growth phase.

Relaxation is qualitatively different at the lowest volume fraction, $\phi \approx 0.565$, with the stress swelling upward after a brief initial drop (Fig. 4.5). Analysis of this phenomenon in the present data is complicated by the presence of a pronounced post-yield collapse in stress at low volume fractions (Fig. 4.2). Because the scale of the post-yield collapse phenomenon varies hugely with strain rate, in these data the initial conditions from which the stress is relaxing themselves come from multiple regimes. At the slowest strain rates, relaxation follows the power-law growth phase, even the beginnings of a steady-state plateauing of stress, while at the highest strain rates relaxation begins before the post-yield drop is complete. Thus it is difficult to say whether the strain rate dependence comes from the initial conditions or from an internal timescale with a memory of the prior strain rate. What is clear is that the behavior at volume fractions near RLP is different from the monotonically downward stress relaxation seen at volume fractions 0.02 to 0.05 above ϕ_{RLP}.

4.4 Discussion

4.4.1 Summary of Experimental Results

To summarize our experimental findings, we report measurements of the mechanical response of loose packings of real, frictional but noncohesive spheres when subjected to constant strain-rate shear strains beyond the yield strain. At the lowest volume fractions studied, $\phi \approx 0.565(5)$, near RLP, we observe a sharp drop in stress immediately following the yielding event. We find the initial shape of the this post-yield stress drop to follow the form of an exponential decay with amplitude scaling with the height of the yield-stress peak, $\sigma_y \sim (\dot{\gamma} T)^{1/3}$, consistent with previous findings (Chapter 3). The characteristic timescale of this decay, is a new timescale, τ, that is a power-law function of the strain-rate without any dependence on age, T. Thus the post-yield stress drop does not obey the symmetry seen in stress-strain curves between $\dot{\gamma}$ and T seen up to the yielding event. For our standard high-viscosity fluid,

the timescale appears to be a fractional power in strain rate, $\tau \sim \dot{\gamma}^{-1/2}$. Curious about what physical timescale balances this square-root, we repeated the experiment in a smaller system and found the same $\tau \sim \dot{\gamma}^{-1/2}$ scaling but with a smaller prefactor, consistent with τ growing proportionally with system size. We also repeated the experiment with a less viscous interstitial fluid and to our surprise found not a different prefactor but a different exponent: $\tau \sim \dot{\gamma}^{-1}$. What balances the square-root in the timescale and the role of the interstitial fluid in setting the $\dot{\gamma}$-exponent remains a mystery.

After the drop in stress post-yield, the stress is found to follow approximately square-root-time growth from its minimum with curves at different strain rates collapsing when the time axis is multiplied by the previously encountered timescale, τ. Thus the $\tau \sim \dot{\gamma}^{-1/2}$ that had emerged as the characteristic timescale of an exponential decay in stress serves as a prefactor in the power-law growth of stress when it rebounds. The higher volume fractions studied, $\phi \approx 0.58$ to 0.60 do not display a pronounced post-yield drop in stress, however, when it follows a power-law, stress growth at all volume fractions collapses onto a single master curve when scaled as predicted for growth. Traces that roll over collapse when scaled as predicted for the approach to a steady-steady shear (see Sect. 4.4.2.3).

In addition to the phenomena studied which look at features that emerge in the stress-response under constant applied strain rates, we also looked at stress relaxation that occurs afterwards at fixed strain. When the applied strain-rate ceases while stress is growing at these higher volume fractions, we see power-relaxation with exponent ≈ -1 with initial timescales and stress amplitudes scaling as seen during the power-law growth phase. The stress does not appear to relax back to its original unstrained value however. The behavior of stress relaxation at fixed strain is more complicated near RLP, where a brief initial drop in stress is followed by a larger upward swell in stress which often rises above the yield-stress peak. Unfortunately the initial

conditions in the present data set vary too much to test for the presence of the same τ in these data.

4.4.2 Extended Maxwell Viscoelastic Model

To motivate the rheological model that we will use to relate the strain-rate scalings of the various features of the stress response let us return to Nguyen et al.'s simple extension of the Maxwell model of viscoelasticity that we introduced in Chapter 3. They use G for the high-frequency (real) elastic shear modulus and have the fluidity, f, evolve subject to the strain history [62]:

$$\dot{\sigma} = -f\,\sigma + G \tag{4.4.1a}$$

$$\dot{f} = -a\,f + r\dot{\gamma}^2\ . \tag{4.4.1b}$$

The first line is the familiar Maxwell model of viscoelasticity [59]. The second is their contribution where positive dimensionless constants a and r set the strengths of aging and rejuvenation of the fluidity. Written instead in terms of the viscous series element, $\eta = G/f$, their model is:

$$\dot{\gamma} = \frac{\dot{\sigma}}{G} + \frac{\sigma}{\eta} \tag{4.4.2a}$$

$$\frac{\dot{\eta}}{G} = a - r\left(\frac{\dot{\gamma}\,\eta}{G}\right)^2\ . \tag{4.4.2b}$$

Nguyen et al.'s experiment had been performed entirely under the constant-stress conditions where $\dot{\sigma} = 0$ and hence Eq. 4.4.2a reduces to $\sigma = \dot{\gamma}\,\eta$. Their model is therefore equivalent to the following so long as stress is held constant:

$$\dot{\gamma} = \frac{\dot{\sigma}}{G} + \frac{\sigma}{\eta} \tag{4.4.3a}$$

$$\frac{\dot{\eta}}{G} = a - r\left(\frac{\sigma}{G}\right)^2. \tag{4.4.3b}$$

This is no minor modification, however, because the behavior of these models differ hugely in the general case where stress can change and we found Eq. 4.4.3 to be much more useful than Eq. 4.4.2 in describing the variable stress conditions of our experiments presented in Chapter 3.

One striking property of the Eq. 4.4.3 is the paucity of dimensionful parameters. Setting the elastic modulus to one, $G = 1$, the equations are simply:

$$\dot{\gamma} = \dot{\sigma} + \sigma/\eta, \dot{\eta} = a - r\,\sigma^2 \ . \tag{4.4.4}$$

The only unit left is time and there are only two independent timescales, $\dot{\gamma}^{-1}$ and η_0, which therefore can only enter the stress-strain relationship as a ratio. To the degree that Eq. 4.4.3 holds, the symmetry between age and strain-rate that was so surprising in the yield stress data is a direct consequence of the lack of any additional timescales and the linear relationship between the initial viscosity, η_0, and the age, T (since $\dot{\eta} \approx a \implies \eta_0 \sim T$). It seems unphysical for the influence of the age, T, to persist indefinitely: there must be some additional timescale, τ, missing from Eq. 4.4.4 over which the symmetry between $\dot{\gamma}$ and T will break down under steady shear.

Another striking property of Eq. 4.4.3 is that the second equation, $\dot{\eta} = a - r\,\sigma^2$ ($G = 1$), resembles an analytic expansion of $\dot{\eta}$ to the lowest order in σ consistent with symmetries. Since σ is tensorial and η is an isotropic scalar, σ^2 is the lowest non-zero order in such an expansion. At longer times we expect the influence of η_0 to wane and the symmetry between $\dot{\gamma}$ and T to break requiring the introduction of a new timescale, τ, against which to compare $\dot{\gamma}$. Adding first order terms in τ to the analytic expansion in σ, we have $\dot{\eta} \approx a - r\,\sigma^2 + g\,\tau/\eta - d\,\sigma\,\dot{\sigma}\,\tau$ where g and d are dimensionless constants tuning the strengths of the growth term which will be significant at small η and the damping term which will oppose sharp changes in σ.

The construction of these terms is highly constrained by the lack of dimensional scales, however, its not clear from first principles that the d-term is the next lowest order term in this expansion. Indeed, we fully expect that in certain conditions other terms that we have neglected may be important, however, the goal in this discussion is only to motivate this model. We shall see that the model with these four terms is sufficient to capture the relative rate-scalings of many of the phenomena we observe in our data. Putting the G's back, our extension of the Maxwell model is,

$$\dot{\gamma} = \frac{\dot{\sigma}}{G} + \frac{\sigma}{\eta} \tag{4.4.5a}$$

$$\frac{\dot{\eta}}{G} = a - r\left(\frac{\sigma}{G}\right)^2 + g\,\frac{G\,\tau}{\eta} - d\,\frac{\sigma\,\dot{\sigma}\,\tau}{G^2}\ . \tag{4.4.5b}$$

Having motivated the model, we now seek approximate solutions in various limiting cases of relevance to our experiments.

4.4.2.1 Previous results: yield-stress-scaling, creep, aging

When the growth and damping terms are negligible, Eq. 4.4.5 can be solved as in Chapter 3. At constant strain-rate it predicts the cube-root age and strain rate scaling of the "yield-stress" stress peak

$$t_y \approx \left(\frac{3\,a\,T}{r\,\dot{\gamma}^2}\right)^{1/3} \tag{4.4.6a}$$

$$\gamma_y \approx \left(\frac{3\,a\,T\,\dot{\gamma}}{r}\right)^{1/3} \tag{4.4.6b}$$

$$\sigma_y \approx G\left(\frac{3\,a\,T\,\dot{\gamma}}{r}\right)^{1/3}\ , \tag{4.4.6c}$$

valid when $\sqrt{r}\,\dot{\gamma}\,T >> 1$.

When solved at constant stress, it reproduces the logarithmic creep seen by Nguyen et al. [62],

$$\eta(t) = a\,G\,\left(T + \left(1 - \frac{r}{a}\,(\sigma/G)^2\right)\,t\right) \tag{4.4.7a}$$

$$\gamma(t) = \frac{1}{a}\,\left(\frac{\sigma/G}{1 - \frac{r}{a}\,(\sigma/G)^2}\right)\,\log\left[1 + \frac{t}{T}\,\left(1 - \frac{r}{a}\,(\sigma/G)^2\right)\right]\,. \tag{4.4.7b}$$

Both of these results depend upon knowing the initial viscosity, η_0, as a function of age, T. Before adding the g-term, to calculate the viscosity after an aging or "waiting" time of duration, T, which followed a highly fluidizing operation like sedimentation, we could simply integrate $\dot{\eta} \approx a$ over the aging time, assume the initial viscosity is negligible and obtain η_0,

$$\dot{\eta}/G \approx a \tag{4.4.8a}$$

$$\int_{-T}^{0} \dot{\eta}/G\,dt = \int_{-T}^{0} a\,dt \tag{4.4.8b}$$

$$\eta(0) = a\,G\,T + \eta(-T) \approx a\,G\,T \tag{4.4.8c}$$

assuming $\eta(-T) \approx 0$.

The growth term, $g\,G\,\tau/\eta$, complicates this simple picture by blowing up at $\eta = 0$. It is still possible to have a parameter regime where $\eta(-T)$ is small yet the g-term is also small compared to a, however, this is no longer necessarily the case.

4.4.2.2 Post-yield drop in stress

When the stress is large and viscosity is sharply decreasing, as in the collapse of the stress immediately post-yield in the experiment, the decrease in stress arises from a balancing of large r and d terms, which yields exponential decay in the stress:

$$\sigma(t) \sim e^{-r\,t/(d\,\tau)} \tag{4.4.9}$$

at a timescale proportional to the timescale $d\,\tau/r$. Thus the timescale that we observe in the post-yield stress collapse is proportional to the timescale, τ, in our model. How τ develops the experimentally observed $\dot{\gamma}$-dependencies seen in the post-yield stress collapse, ($\tau_{\text{collapse}} \sim \dot{\gamma}^{-1/2}$ for the high interstitial viscosity system and $\tau_{\text{collapse}} \sim \dot{\gamma}^{-1}$ for the low interstitial viscosity system) is external to this model and is probably the most interesting question arising from this work.

4.4.2.3 Stress growth and steady-state shear

The solid-like behavior at the startup of steady strain rate shear below the yield-stress assumes a substantial initial viscosity, η. A distinct solution exists for the case of the slow growth of stress starting from a small σ, small η starting point. Assuming the g-term dominates the a, r and d-terms and the growth is slow enough to neglect the solid response in the Maxwell model, predicts stress growth:

$$\eta(t) \approx G\sqrt{2\,g\,\tau\,t} \tag{4.4.10a}$$

$$\sigma(t) \approx G\,\dot{\gamma}\sqrt{2\,g\,\tau\,t} \tag{4.4.10b}$$

Thus we expect stress to grow as a power law, with the square-root of time, and to collapse when stress is scaled by $\dot{\gamma}^1$ and time is multiplied by τ. In Fig. 4.3 we see the data collapse when scaled this way except for curves that appear to beginning to plateau.

The plateau can be understood in the model as the approach to a steady-state solution balancing the growth and rejuvenation terms. Neglecting the a-term, the steady-state solution is:

$$\sigma_{\text{ss}} = G\left(\frac{d\,\tau\,\dot{\gamma}}{r}\right)^{1/3} \tag{4.4.11a}$$

$$\eta_{\text{ss}} = G\left(\frac{d\,\tau}{r\,\dot{\gamma}^2}\right)^{1/3}. \tag{4.4.11b}$$

Which sets the stress scaling expected for stress growth curves that plateau.

The shape of the approach to the long-term steady-state comes from expanding about the steady-state solution by substituting $\eta(t) = \eta_{\text{ss}}\,(1 - \xi(t))$,

$$g\,\tau\,\left((\xi-1)^3+1\right) = \left(\frac{g\,\tau}{r\,\dot{\gamma}^2}\right)^{\frac{2}{3}}\,(\xi-1)\,\dot{\xi}\;, \tag{4.4.12}$$

where $G = 1$. Discarding higher order terms to linearize,

$$\dot{\xi} = -3\,(g\,\tau\,r^2\,\dot{\gamma}^4)^{\frac{1}{3}}\,\xi \tag{4.4.13}$$

this has solution,

$$\xi(t) \sim \exp\left(-t\,/\,(3\,(g\,\tau\,r^2\,\dot{\gamma}^4)^{\frac{1}{3}})\right) \tag{4.4.14}$$

Incorporating the $\dot{\gamma}$-dependencies we have seen in τ, the timescales approaching steady state are thus $\tau_{\text{ss}} \sim \dot{\gamma}^{-7/6}$ for the high viscosity interstitial fluid where $\tau \sim \dot{\gamma}^{-1/2}$ and $\tau_{\text{ss}} \sim \dot{\gamma}^{-1}$ for the low viscosity fluid where $\tau \sim \dot{\gamma}^{-1}$. This provides the scaling expected to collapse the time axis of stress growth curves that plateau. In Fig. 4.3, the lower strain rates at the lowest volume fraction that do not collapse against the scaling predicted for the growth regime show promise of collapsing against these predictions for stress approaching steady-state.

4.4.2.4 Stress relaxation at constant stress

It is also possible to obtain an approximate solution for stress relaxation relevant to the relaxation at volume fractions $\phi \approx 0.58$ to 0.60. The small-stress solution where the g and d-terms are negligible, displays power-law relaxation,

$$\eta(t) = a\,G\,t + \eta(0) \tag{4.4.15a}$$

$$\sigma(t) = \sigma_0\,(1 + a\,G\,t/\eta_0)^{-1/a}\;. \tag{4.4.15b}$$

The data in Fig. 4.4 are consistent with power-law relaxation with $a \approx 1$. Thus in the absence of driving forces, the viscoelastic relaxation time in the system $\tau_{\text{visc}} = \eta/G$ is the age of the system.

Since the stress relaxation in Fig. 4.4 follows the stress growth regime, it is possible to predict the strain-rate scaling of the parameters in the model from the scaling of the growth phase. The parameters in this solution amount to the initial stress, σ_0, and the initial relaxation timescale, η_0/G. Since the strain ceases at $\Delta\gamma = \dot{\gamma}\, t$, $\sigma(t) \approx G\dot{\gamma}\sqrt{2\, g\, \tau\, t}$ during growth and $\tau \sim \dot{\gamma}^{-1/2}$ for the high interstitial viscosity system, it is possible to predict the strain-rate scaling of the final values of σ and η in the growth phase. Their final values are the initial values σ_0, η_0 in the relaxation phase, and are predicted to scale as $\sigma_0 \sim \dot{\gamma}^{1/4}$ and $\eta_0 \sim \dot{\gamma}^{-3/4}$. Indeed this is what we see in Fig. 4.4 with the only deviation occurring in the $\dot{\gamma}$-exponent of σ_0 which is somewhat larger than the predicted 1/4 at the higher rates where the small-σ assumption used to calculate Eq. 4.4.15b may be violated.

4.4.2.5 Limitations of Model

This model does, however, miss certain phenomena. Where the small-strain approximation is valid, Eq. 4.4.15b fits relaxation curves very well, however, the fits predict stress relaxation back to a new baseline value, σ_∞, that depends little on strain-rate. There is unquestionably a mode of evolution marked by the changing stress baseline that the model is missing at these volume fractions. The model also misses the upward swell in stress seen during relaxation at volume fractions near RLP. That this should be the case is not surprising: volume fraction does not enter our model, yet we know that settling occurs particularly at the lowest volume fractions when the packing is disturbed. A full understanding of this system would seem to require at the very least a coupling between σ and ϕ. Any evolution of the timescale $\tau(t)$ is also beyond the scope of this simple model.

4.4.3 Conclusion

Previous to our work, there were scant expectations for the mechanical response of sphere packings near RLP. Simulations had measured the compressive modulus but not attempted the shear modulus [85] and experiments in this regime had measured steady-state shear response [80, 60] and creep at constant stress [62]. But no prior work existed on the important case of short time response to constant strain rate shear.

To this body of work we have added experimental results concerning a number of phenomena which occur during the startup of steady-state shear including an initial stress peak ("yield stress"), the shape of the subsequent drop of the stress after failure and shape of stress growth as it recovers. We also present stress-relaxation data at fixed strain, filling in the last of the common modes of shear perturbation (i.e. constant stress, constant strain rate, constant strain).

We find that a simple lowest-order expansion of the viscous element in the 1d Maxwell model, Eq. 4.4.5, describes the rate-scaling of a great many of the features of the system. This approach succeeds in predicting the cube-root age and strain-rate scaling of the initial "yield-stress" stress-peak of Chapter 3 and the strain-rate scaling as well the shape of the square-root time growth of stress beyond the strain. It is also consistent with the collapse of stress immediately post-yield in packings near RLP, power-law stress relaxation at constant strain rate, as well as log-time creep at constant stress observed elsewhere [62].

This simple treatment introduces only a single scalar, τ, to represent an internal timescale in the system. For systems with a high-viscosity interstitial fluid, this timescale, which first emerges as the characteristic decay time of the stress after the yield-point is exceeded, is found to itself scale as a power-law with strain rate, $\tau \sim |\dot{\gamma}|^{-1/2}$. And this same τ reappears in the subsequent features of growth and relaxation. Our model which takes the Maxwell model of viscoelasticity, $\dot{\gamma} = \dot{\sigma} + \sigma/\eta$,

and expands the viscous element in stress, σ, and an unknown timescale, τ, to obtain, with $G = 1$, $\dot{\eta} \approx a - r\,\sigma^2 + g\,\tau/\eta - d\,\sigma\,\dot{\sigma}\,\tau$ thus provides the rationale for seeing the influence of a single timescale, τ, in three separate features of the mechanical response of the system where certain terms dominate allowing for closed form solutions. That the particular form $\tau \sim |\dot{\gamma}|^{-1/2}$ should develop in the high interstitial viscosity system is unexpected. We neither predicted it nor can offer an after-the-fact explanation even though dimensionally it begs for one.

The result that $\tau \sim |\dot{\gamma}|^{-1}$ in the lower viscosity interstitial fluid is surprising in that it amounts to a change in the exponent and not simply the prefactor, however, it is otherwise less surprising than the $\sim |\dot{\gamma}|^{-1/2}$. Up to an absolute value, having a timescale $\sim |\dot{\gamma}|^{-1}$ means that stress traces collapse not against time but against strain, $\gamma = t\,\dot{\gamma} = t/\dot{\gamma}^{-1}$. Since this is the timescale that appears in the system with the lower viscosity interstitial fluid, we can see that this system is behaving quasi-statically—following the same stress–strain curve regardless of $\dot{\gamma}$.

In motivating the expansion of η, we commented that a new timescale beyond η_0 and $\dot{\gamma}^{-1}$ had to be introduced to describe any $\dot{\gamma}$-dependence of the steady-state stress. Thus it should come as no surprise that plugging in $\tau \sim |\dot{\gamma}|^{-1}$ into the solution for steady-state stress yields a constant because $\tau = 1/|\dot{\gamma}|$ is not a new timescale at all. Thus the regime of behavior of this low viscosity interstitial fluid system appear to be in the quasi-static regime reported elsewhere at similar volume fractions [80, 60].

CHAPTER 5

STRUCTURE OF LOOSE PACKINGS

5.1 Introduction

In this chapter we turn our attention to the three dimensional structure of loose sphere packings. One important aim is simply to better characterize the system whose average mechanics we have explored in the previous two chapters. In much of the work to this point, we have assumed that the packing can be approximated as spatially homogeneous and rotationally isotropic. Yet the outer walls containing the packing are flat and smooth so it may be that crystalline order is induced by the walls. Further, the packing is not density matched so inhomogeneity in the vertical direction due to the weight of the packing is possible.

We address homogeneity by looking at the spatial variations in local volume fraction and crystalline order parameters. We find that there is layering near the walls but there is no sign of increased crystalline order and the layering actually suppresses the volume fraction over a short range. We see no vertical dependence of any of these measures suggesting that gravitational pressure is saturated and fully supported by the walls [47]. We address isotropy via distributions of bond-angles which are found to be isotropic away from the walls. Thus, we find no indication of deviations from homogeneity and isotropy in the bulk.

We also look at distributions of local volume. As mentioned in the introductory chapter, there are statistical theories substituting energy in equilibrium theories with free-volume [35]. These theories predict a Boltzmann distribution of free-volumes which can be tested against the local cell volumes when the packings are partitioned

into Voronoi and Delaunay diagrams. We find that volume distributions in both partitions are not fully exponential but do possess Boltzmann tails. There is, however, a significant discrepancy between the "granular temperatures" of the tails in the Delaunay and Voronoi partitions.

As described in the introductory chapter, prior work has been done on the form of the radial distributions function, $g(r)$, in similar materials. We measure $g(r)$ and, with a new approach to fitting the data, demonstrate a greater consistency with predictions of simulation [86, 85] and isostatic theory [1, 35] than had previously been reported in experiments on loose spheres [4, 5]. We also introduce a numerical method that uses the Ornstein-Zernicke equation [68] to show that the locations of longer ranged peaks in $g(r)$ follow as a consequence of sharp features in $g(r)$ observed at $r \approx d$.

Prior work has used Steinhard-Nelson crystalline order parameters [88] to look for signs of crystalline structure with the finding that only a small fraction of the spheres have a bond-structure with both q_4 and q_6 consistent with FCC or HCP order [3]. Since truly crystalline regions therefore do not appear to be present in loose sphere packings, we look at these "crystalline" order parameters, q_n, less with the aim of locating crystals and more as rotationally invariant measures of nth-degree structure and thus we are not constrained to $n = 4$ or 6. We measure these order parameters for $n = 2$ to 9 and conclude that maybe q_6 is special after all. We also perform Monte-Carlo simulation of the contacting neighbors of a single sphere to determine whether the observed q_4 and q_6 distributions follow solely from the number of neighbors and hard-sphere constraints and conclude that they do not: there is additional order present in the arrangement of neighbor bonds. We go on to explore spatial auto-correlations and cross-correlations of ϕ, q_4 and q_6, finding all auto-correlations and cross-correlations to be very short ranged but with significant negative correlation

coefficient at $r = 0$ between local volume fraction and q_4 and q_6 providing further evidence that high values of q_n do not mark crystalline regions, even locally.

5.2 Methods

The apparatus and protocols used in this chapter are the same as in Chapter 3 with the addition of volumetric imaging (see Fig. 5.1).

5.2.1 Three Dimensional Imaging

Volumetric imaging is accomplished using the higher viscosity fluid described in Sect. 3.3.1 composed of high-temperature silicone oil (Acros Organic) and mineral oil (Fisher Scientific) mixed in an 82.5:17.5 mass ratio and with 6×10^{-7} weight fraction Nile Red fluorescent dye. This fluid mixture is mixed to have a slightly higher refractive index than the acrylic spheres at room temperature. Because the index of refraction of the fluid decreases with temperature more quickly than the solid, enclosing the packing in a temperature-controlled container allows the index match to be tuned via temperature with the best match of refractive indices occurring at $31\,\mathrm{deg}\,C$. This fluid has dynamic viscosity, $\eta_f = 110\,\mathrm{mPa}\cdot\mathrm{s}$, and density, $\rho_f = 1.021(1)\,\mathrm{g/cm^3}$, both measured at 21 °C after mixing and degassing as described in Sect. 2.2. From our work in Chapter 2, we know that this mixture will not swell or damage the acrylic beads yet wets acrylic well enough to avoid the formation of nano-bubbles on the surface of the beads.

Close index-matching reduces scattering and lensing at interfaces between the spheres and the fluid allowing a laser-beam which has been spread into a sheet by a cylindrical lens to remain collimated as it passes through the packing. The small amount of fluorescent Nile-red dye dissolved in the fluid glows yellow when the green (532 nm) laser-sheet excites it. Since the beads do not fluoresce, images of the slices show beads as dark circles against a bright background.

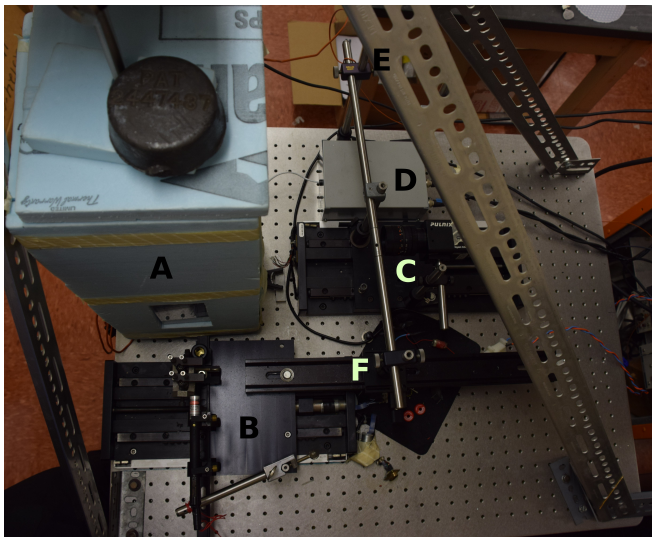

Figure 5.1: Photograph of the volumetric imaging setup taken from above: A) the shear apparatus sketched in the center of Fig. 3.1 is enclosed in an insulated, temperature-controlled box with acrylic windows, B) the green laser, slit and diverging lens are mounted on a computer-controlled motion stage, C) the camera is mounted on a passively sliding motion stage that moves a fixed fraction of the distance traveled by the laser. The stainless steel rod rotates about (D) and slides in mounts at (E) and (F). Perpendicular distances from E to D of 19.8 cm and D to F of 23.2 cm are used to keep the image of the laser slice in focus while the laser slice steps into the packing.

The laser and the diverging lens are mounted on a motion stage. Three dimensional raster images are generated by stepping the laser-sheet through the packing in steps of size comparable to the width of the sheet, about $1/10\,d$. To maintain the apparent size of the spheres as the laser slice steps into the packing despite the differences in refractive index between the packing in which the laser slice is moving and air through which the camera is moving, the camera is mounted on a sliding track with the distance of the camera from the packing mechanically coupled to the motion stage on which the laser is mounted (see Fig. 5.1). Because the refractive index of the packing, $n_{\mathrm{PMMA}} \approx 1.49$, is higher than that of air, light rays straighten out when they enter the packing increasing the distance to the focal plane over what it would have been in air. Thus we find that the image of the laser slice can be kept in focus by moving the camera forward a fixed fraction of the amount the laser slice was moved forward. This is accomplished mechanically with a rigid bar through points E, D and F in Fig. 5.1. The relative lengths of E to D and D to F were tuned to keep the image in focus and maintain the apparent size of objects in the image.

5.2.2 Sphere detection

Once we obtain 3-D images of the packing, the next step is to locate the bead centers. There are three broad strategies for detecting spherical particles in an image:

1. locate areas of correlation between the image, possibly after a derivative or edge-detection operation, and an ideal particle

2. identify morphological clusters and locate particles via the center-of-mass of the cluster

3. perform non-linear least-squares model fitting.

All of these methods have been used previously to locate particles. We employ a two-part strategy of 1. followed by 3., using cross correlation to give rough estimates of sphere centers then sharpening those locations via nonlinear least-squares fitting.

Both of our detection steps require the ability to generate an image kernel, that is a 3D image of an ideal particle. In the case of our image data where the voxels are wider along the step axis than in the in-plane axes, this kernel needs to be ellipsoidal, being bright (1) outside the ellipsoid where the fluorescent dye glows and dark (0) inside the ellipsoid. The simplest way is to generate an array with value 0 if the center of the voxel is inside the ellipsoid and 1 otherwise, however, the sharp edges of such a kernel do not shift smoothly: as the center of the ellipsoid moves voxels on the boundary jump between 0 and 1. This leads to sub-pixel bias in locating the centers via cross-correlation and discontinuities which are problematic for least-squares fitting algorithms. To mitigate these issues we generate "ideally downsampled" ellipsoidal kernels by integrating the volume of ellipsoid contained in each voxel. Such kernels are ideally downsampled in the sense that these are the kernels that would be obtained by averaging over bins of a much higher resolution kernel.

The initial cross-correlation detection strategy is to generate an ellipsoidal kernel centered at the origin with as near to the actual radii of the spheres in the image as possible (the x, y and z diameters are approximately 24.06, 12.15 and 24.06 voxels). The full volumetric image is too large for a discrete Fourier transform to be taken in a desktop computer's memory but the convolution kernel has finite extent so the cross-correlation can be computed in chunks so long as the chunks are larger than the ellipsoid. Choosing power-of-two sizes for speed, chunks of the image with sufficient boundary padding are pulled into memory and convolved with the kernel via Fourier convolution. Sphere centers are then detected as local maxima in the brightness of the convolved image. The locations of these maxima are corrected for the offset of the chunk and stored. To locate the local maxima to sub-pixel accuracy, we fit a

paraboloid to a 3x3x3–voxel volume surrounding the brightest voxel recording the eivenvalues of this fit as well as the location and brightness. This yields a list of locations of maxima which contains duplicates arising from particles lying near the boundary between two chunks and maxima which arise in the cross-correlation in the void space between 4 contacting spheres. Filtering out the duplicates is trivial as those locations are the same to numerical precision. Filtering out the spurious maxima detected at the center of the void region between 4-sphere contacts requires more care. However, these spurious maxima are characterized by being a somewhat lower maximum surrounded by four more strongly detected particles which overlap by approximately $d/2$, have a void in the image at their centers and have very different eigenvalues from true particles. There is a region at large step depth into the packing and where the laser slice has traveled deeply into the packing where detection accuracy is low enough that not all of these criteria agree for every detected maximum. We have discarded data from that region.

The second step in our particle detection is to sharpen the locations of the detected spheres by nonlinear least-squares fitting. Again, as the full volumetric image is relatively large ($\approx 1/2$GB), the computation is done by streaming chunks of the image about a given particle from disk. The full scheme is to maintain a list of approximate sphere centers which is continually updated as the neighborhood around each particle is pulled in and that particle fit. Explicitly, for a given particle, i, we pull in a portion of the volumetric image data just large enough to include the centers of the nearest neighbors of particle i. We then built a model function with three free parameters, x_i, y_i, z_i, the locations of the sphere, i, by drawing ideally downsampled spheres at the best known locations of all of i's neighbors whose centers fall within $1.5\,r$ of (x_i, y_i, z_i). With the locations of the neighbors fixed, we then perform a non-linear least squares fit to i's coordinates, x_i, y_i, z_i, by minimizing the least-squares difference between the model image and the portion of the volumetric image with particle i at its center.

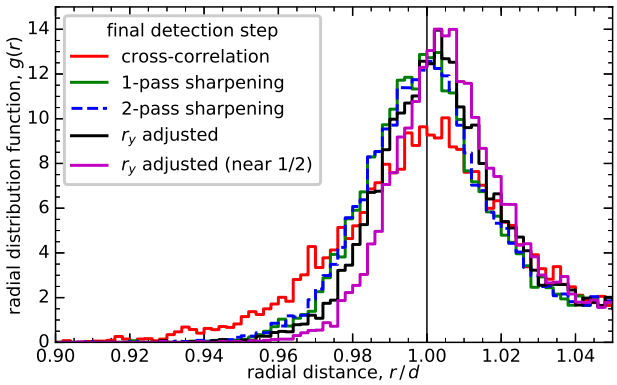

Figure 5.2: Peak at one diameter separation in the radial distribution function at the lowest volume fraction: The sharpness of the peak at $r \approx d$ is a useful measure of the detection accuracy. A single pass of the nonlinear least-squares fitting procedure to sharpen sphere locations yields an approximately 50% improvement in the sharpness of the peak. A second pass yields little further improvement. Adjusting the ellipsoidal radius of the step-axis has a small effect in the sharpness of the peak. The last curve shows the peak calculated from only the half of the image nearest to the camera. It is sharper than average demonstrating that detection accuracy decreases somewhat with depth, y.

The location list is then updated with the new estimate for i's location and this is repeated for another particle. As can be seen in Fig. 5.2, the corrections become small after a single pass of this sharpening procedure so, because it is a time-consuming calculation to run, all of the data presented subsequently in this chapter come from a single pass of the sharpening procedure.

5.3 Results

5.3.1 Spatial homogeneity and wall effects

In this section we test the assumptions of spatial homogeneity and angular isotropy made implicitly in the analysis of the previous chapters. We investigate homogeneity by looking at the spatial dependence of locally defined scalars such as volume fraction and crystalline order parameters. We investigate isotropy via the distributions of bond angles against coordinate axes.

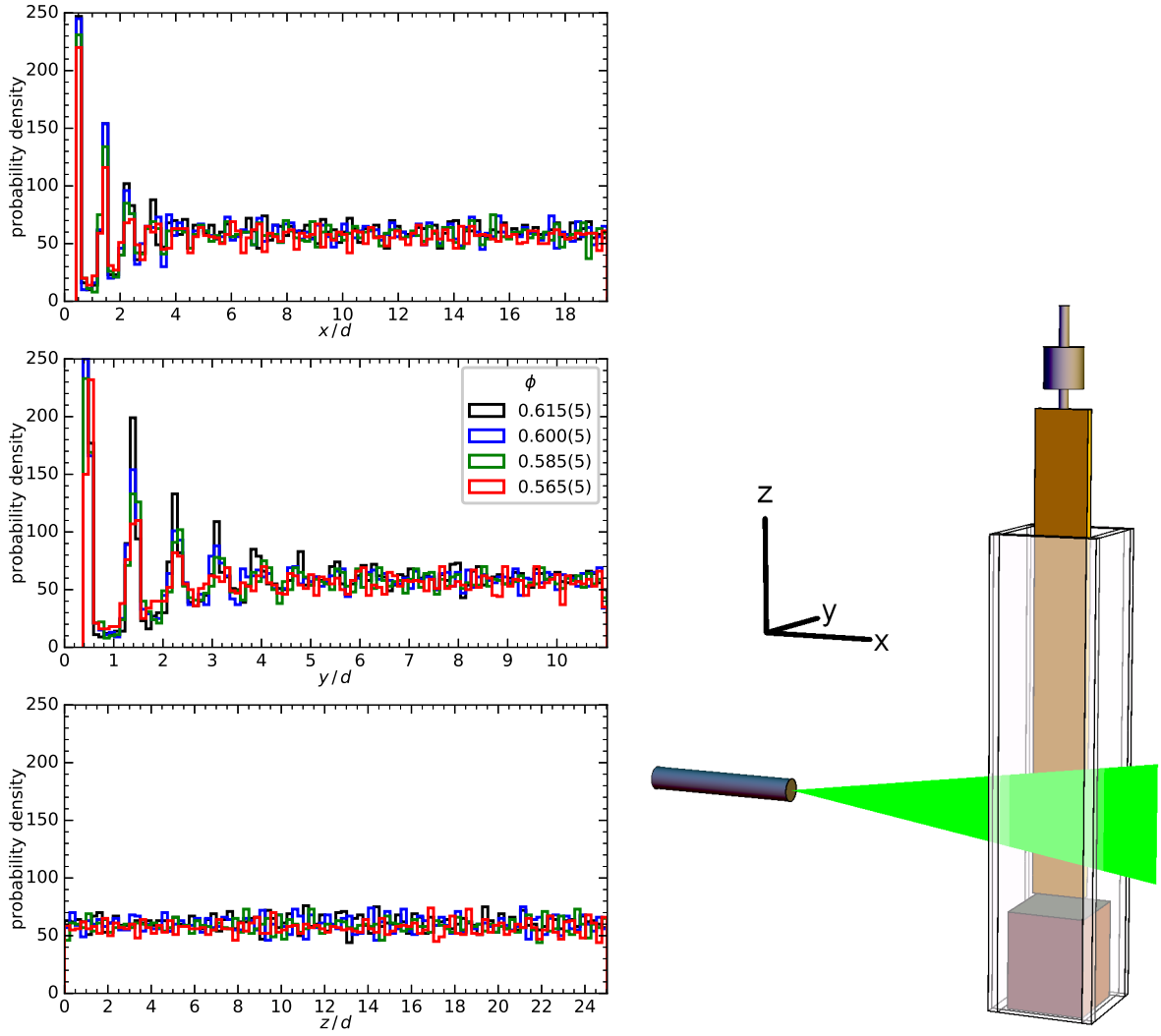

Figure 5.3: Distributions of sphere locations along coordinate axes: There is layering near the walls at $x = 0$ and $y = 0$ which persists 3 or 4 sphere diameters into the packing. No wall is visible in the 3D image in the vertical, z-direction.

The geometry of the packing (Fig. 5.3B) is such that the system is narrower along the horizontal y-axis than in either of the other imaged directions. Layering occurs near the walls at $x = 0$ and $y = 0$, but due to the geometry is more pronounced near the $y = 0$ wall. This layering can be seen directly via the distribution of y-coordinate values of the sphere centers as shown in Fig. 5.3(A) and is short-ranged, disappearing in 3 to 4 sphere diameters. The effects of layering are also present in the excess of bonds perpendicular to the y-axis seen in the left column of Fig. 5.4 which shows bond angles versus coordinate axes for the entire packing. Again, the layering is short ranged (Fig. 5.5) and the right column of Fig. 5.4 which excludes spheres within $4\,d$ of the walls does not display this excess.

Wall effects are also reflected in the local volume fraction near the walls, which, interestingly, is lower near the walls than in the bulk (Fig. 5.6). The influence of the walls on volume fraction is also short ranged, falling off over a characteristic length of approximately the sphere diameter, so that little influence remains 3 or $4\,d$ from the wall. There is no clear trend near the walls in the values of the crystalline order parameters q_4 and q_6 (defined and discussed in Sect. 5.3.5). So while there is evidence of layering at the walls, there is little indication that the structure is crystalline near the walls. The lower volume fractions near the walls reinforce this point: flat walls do not seem to drive order at these loose volume fractions the way they do near RCP.

Away from the walls the packing appears to be homogeneous and isotropic. There is no clear trend in the vertical direction (z) in ϕ or the crystalline order parameters nor is there deviation from an isotropic distribution of bond-angles with respect to the coordinate axes.

5.3.2 Radial distribution

Having established that the packing is isotropic and homogeneous, we now consider the radial distribution function, $g(r)$, which is the radial part of the autocorre-

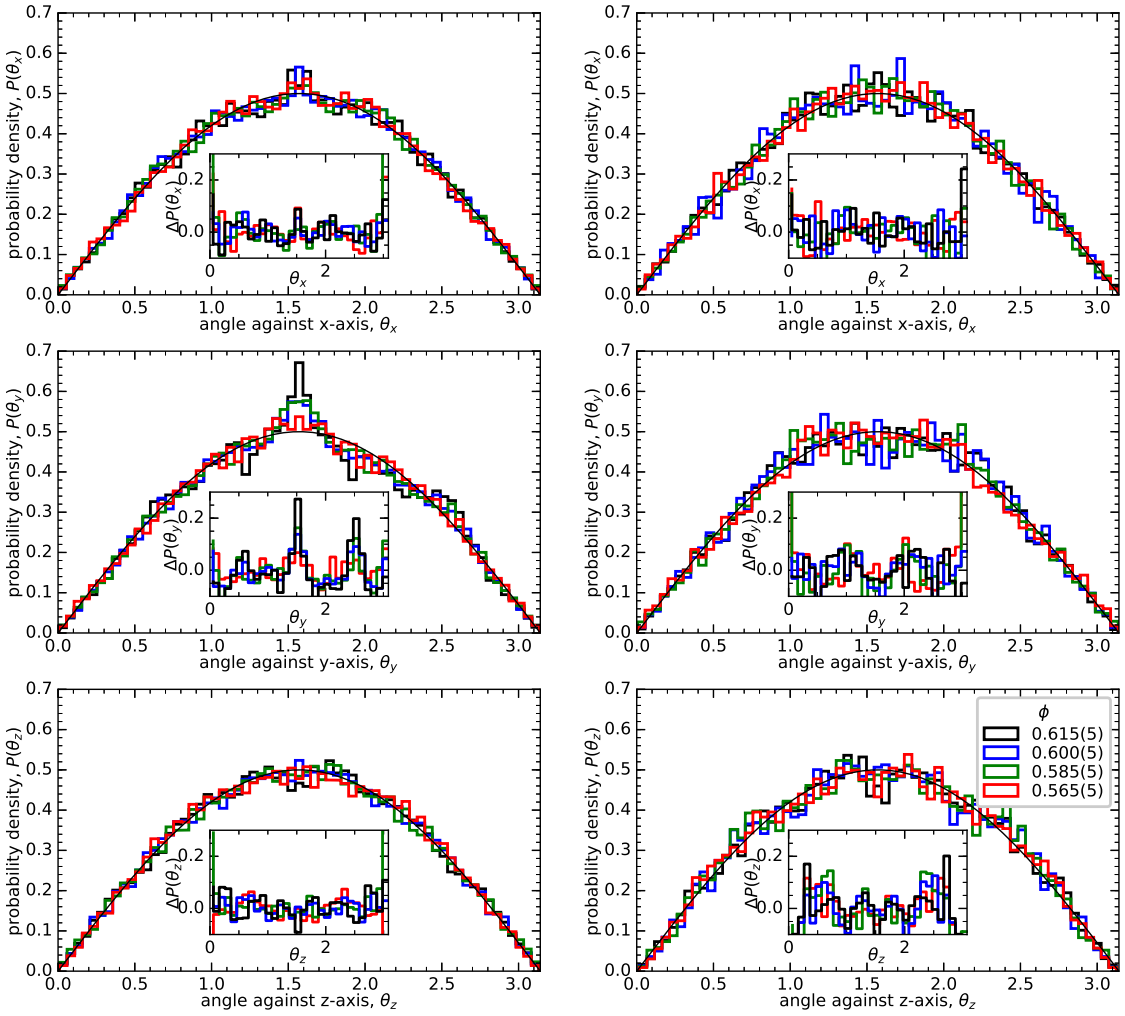

Figure 5.4: Distributions of bond-angles versus the three coordinate axes: Angles are calculated between nearest-neighbor bonds and a given coordinate axis. In these data neighbors are defined as lying within a maximum distance of $1.1\,d$. The left column shows the distribution for the entire packing and displays peaks relative to the distribution expected for an isotropic packing (black line). The insets show the relative difference between the distribution and the form expected for an isotropic material, $\Delta P(\theta_i) = P(\theta_i) \,/\, (\sin(x) \,/\, 2) - 1$. In the full packing (left column), we are seeing excess bonds located perpendicular to the two horizontal axes which happen also to be the coordinates which begin on walls. The right column shows the distributions for particles that are at least a distance $4\,d$ from the nearest wall and the peaks have disappeared. Thus this phenomenon disappears in the bulk: it is caused by the walls.

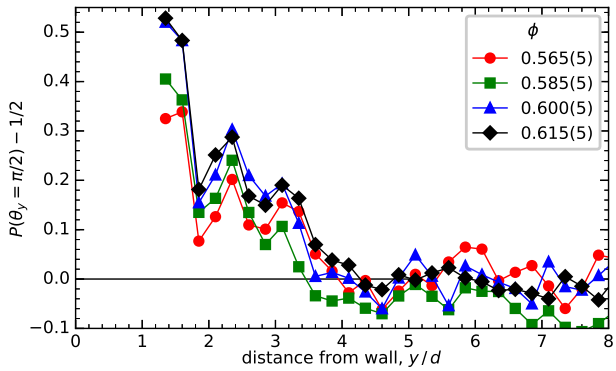

Figure 5.5: Amplitude of the excess in bond angles versus the distance from the wall at $y = 0$: The differences, $\Delta P(\theta_i) = P(\theta_i) \,/\, (\sin(x) \,/\, 2) - 1$, at $\theta_y = \pi/2$ from Fig. 5.4 are plotted at the four different volume fractions against the distance, y, from the front wall. The influence of the wall is seen to disappear in 3 or 4 sphere diameters into the packing and increases in amplitude with increasing volume fraction.

lation of number density. An intuitive way of thinking of $g(r)$ is if the origin is set at a particle's center, then $g(r)$ is the probability density of other particle centers lying within a thin shell at radius, r.

In ideal packings of monodisperse hard spheres of diameter, d, incompressibility of the spheres means that $g(r)$ is zero for r less than d. Then at $r = d$ it must jump from 0 to average number of contacts, Z, (also called the "coordination number") that lie at distance $r = d$. This implies that a discontinuous step exists in the number of spheres within radial distance, $N(r)$. Letting $d = 1$, the number of spheres within distance, r, can be written as an integral of $g(r)$,

$$N(r) = \int_0^r g(\tilde{r})\, 4\,\pi\, \tilde{r}^2\, d\tilde{r} \tag{5.3.1}$$

So the step in $N(r)$ marks a delta function in $g(r)$:

$$g(r) = Z/(4\,\pi)\, \delta(r - 1)\ . \tag{5.3.2}$$

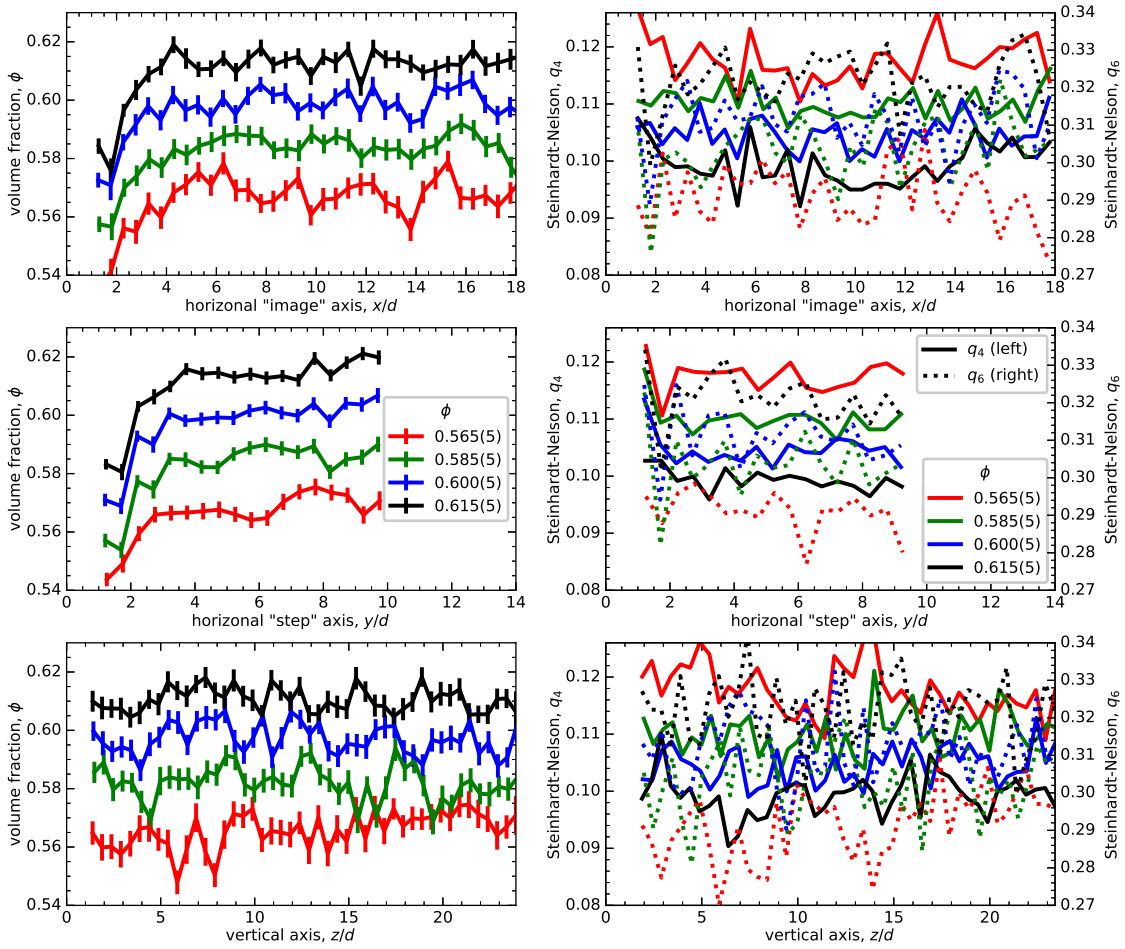

Figure 5.6: Average local values of volume fraction and Steinhardt-Nelson q_4 and q_6 crystalline order parameters along coordinate axes. Local values of volume fraction, ϕ, are calculated for individual Voronoi cells. Averages plotted are volume-weighted averages (volume-weighting makes a small but noticeable difference). q_4 and q_6 are calculated locally over the bonds to each sphere's Voronoi neighbors. Averages of the q_n are not weighted by the Voronoi cells volumes (volume-weighting does not make an appreciable difference when plotting at this resolution). Left column: the local volume fraction is plotted along the vertical (z) and two horizontal axes: x which lies in the focal plain of the camera increasing with increasing depth of the laser slice penetrating into the packing and y which measures depth away from the camera into the packing. The volume fraction can be seen to decrease close to walls at $x = 0$ and $y = 0$. There is no wall in the imaged section of the packing in the vertical direction. The volume fraction can be seen to reach bulk values a depth of 3 or 4 diameters away from the walls. q_4 increases somewhat approaching the walls over a similar range, however, the ranges of the q-parameters in these plots is quite narrow.

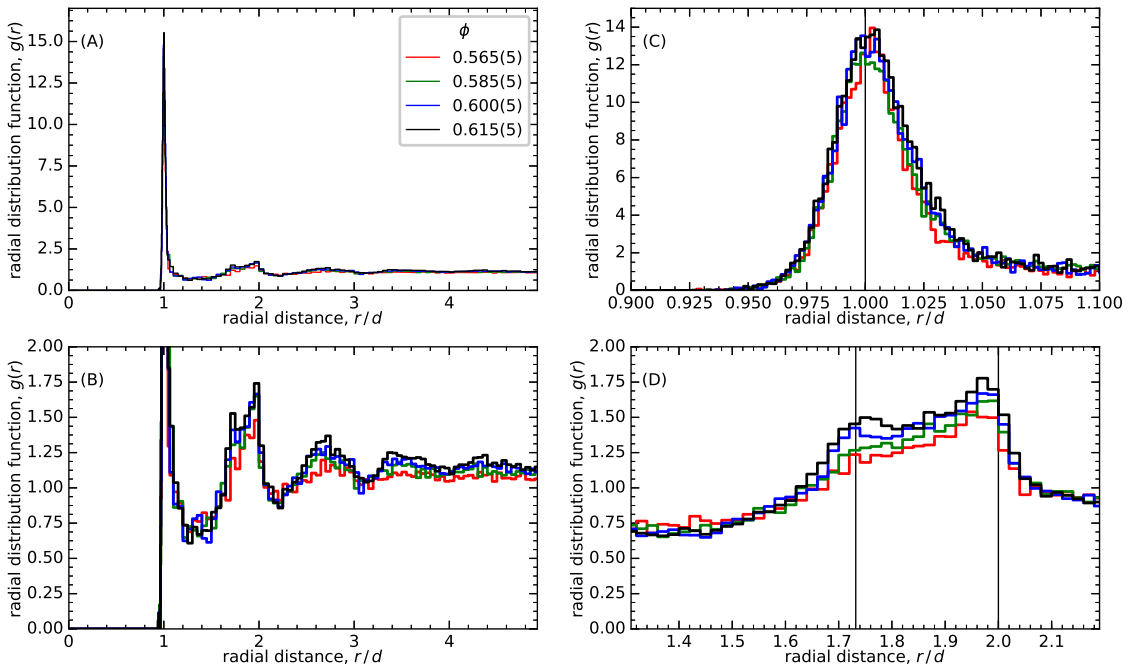

Figure 5.7: Radial distribution functions at all four volume fractions: The radial distribution function (A and B) possesses a sharp peak at the radial distance of one bead diameter. This peak (C) is comprised of contacting particles and near misses and changes little with volume fraction. (B): structure is seen to develop with increasing volume fraction. This change is most pronounced in the growth of a peak near $r = \sqrt{3}\,d$. (D) shows this peak and a peak that appears to fall just short of $r = 2\,d$.

The isostaticity argument (Sect. 1.5.1) predicts that $Z = 4$ for large friction and $Z = 6$ without friction.

One might suppose that this is all the structure that exists in a disordered sphere packing with $g(r)$ dropping immediately to the average number density, ρ, for $r > d$, however, previous work has found a number of non-trivial features in $g(r)$ including a prominent power-law after the $r = d$ peak [86], and smaller peaks near $\sqrt{3}\,d$ and $2\,d$, the former being observed to grow with volume fraction and both possibly possessing similar power-law tails [4, 5].

Fig. 5.7 displays the radial distribution function for the four volume fractions we studied. Fig. 5.7(A) confirms the presence of a sharp peak near $r = d$, however, it is

not infinite: evidently the delta function is being smoothed by some mechanism. In general we expect broadening of the delta function to arise from compression of the particles, polydispersity of the spheres themselves, and detection error. In this system average forces are small (although it is possible that stresses are concentrated on a few particles) and the beads are highly uniform so we expect that this broadening is due primarily to detection error. Left of the $r = d$ peak, $g(r)$ resembles a Gaussian with standard width $\sigma \approx 0.01\,d$ but with a heavier tail to the right. This first peak changes little with volume fraction, however, there is noticeable evolution in subsequent peaks with a peak developing at $r \approx \sqrt{3}\,d$ as volume fraction increases and subsequent oscillations growing in amplitude. This is in line with the findings of Aste et al. [4]. We note that the peak near $r = 2\,d$ falls slightly short of $2\,d$. Although they do not call attention to it, this also appears to be the case in [4, 5]. Given that the next two peaks fall far short of $3\,d$ and $4\,d$, we suspect that this is part of a trend of decreasing period with increasing distance.

The shape of the sharp peak near $r = d$ where contacts occur is of great importance in the understanding of the local structure of sphere packings. If this peak were simply a delta function, then one could integrate over it to obtain the average number of contacts and so test the isostaticity conjecture. It was first observed in simulation, however, that this is complicated by a large number of near contacts which follow a power-law for $r > d$, going like $g(r) \sim (r/d - 1)^{-\alpha}$ with $\alpha = 1/2$ [86, 65]. Subsequent simulations have found slightly lower value for this exponent $\alpha \approx 0.4$ [32] and Aste et al. report fits to experimental data giving a range of values in which increase with volume fraction from 0.3 to 0.45 for volume fractions from ≈ 0.58 to 0.64. Plotting $g(r)$ for our system on log-log axes (Fig. 5.8A), we see a range of about a decade in $r/d - 1$ where $g(r)$ is declining as a power-law with exponent $\sim -1/2$, however, when a power-law, $g(r) \sim (r/d - 1)^{-\alpha}$, is fit to this range, we see α increase with ϕ similarly to the trend reported by Aste et al. [4].

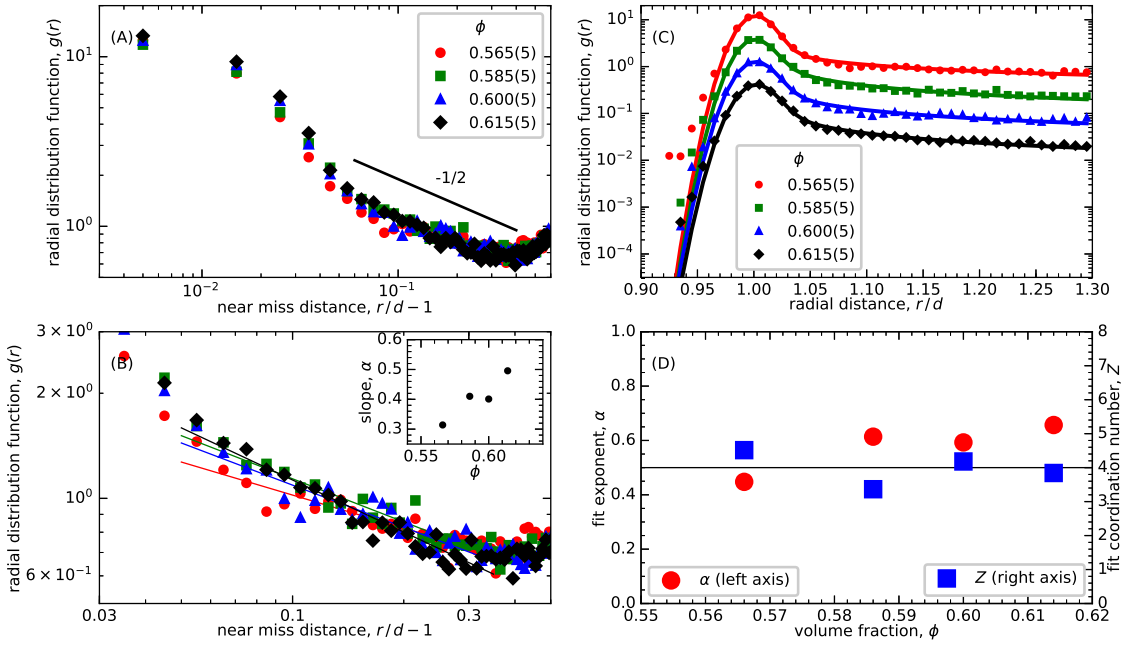

Figure 5.8: Analysis of the shape of the peak in the radial distribution function at $r = d$ for all four volume fractions: A: There is a region spanning roughly a decade where $g(r)$ drops as roughly a power-law of the near miss distance $r/d-1$. In (B) this region is fit to the power-law form $g(r) \sim (r/d-1)^{-\alpha}$. In the inset the magnitude of the fit exponent can be seen to increase with volume fraction. The right panel presents an alternative method of fitting these data where $g(r)$ is taken to have the form $Z/(4\,\pi)\,\delta(r/d-1) + B\,\theta(r/d-1)\,(r/d-1)^{-\alpha}$ convolved with a Gaussian of standard width σ. (C) displays least-squares fits of the first peak to this form. To make the fits discernible the lowest volume fraction series is plotted normally and each subsequent data series is shifted downward by half a decade. (D) shows the values of the exponent, α, and the average coordination number, Z, coming from the fit. There is no obvious trend in volume fraction but there is a clear interdependence of these estimates. The estimates of Z lie near the value of 4 predicted by isostaticity and seen in simulation at RLP at large friction coefficient. For the four volume fractions, parameter estimates are: Z=[4.5, 3.4, 4.1, 3.9], B=[0.39, 0.30 , 0.30 , 0.26], α=[0.45, 0.61, 0.59, 0.66] and σ=[0.014, 0.014, 0.014, 0.015] where $g(r)$ with bin width $\Delta r = 0.002\,d$ is fit up to $r = 1.3\,d$ and $g(r)$ is normalized as a number density (note that for viewability the bin width as plotted in (C) has been reduced to $\Delta r = 0.01\,d$).

The shape of this tail is important if we are to separate the average number of true contacts, Z, from the the apparently diverging probability of near-misses. We follow Aste et al.'s example of modeling the experimental $g(r)$ near $r = d$ as the convolution of an ideal radial distribution function, $\tilde{g}(r)$, with a Gaussian representing measurement error, $N_\sigma(r)$.

$$\tilde{g}(r) = Z/(4\,\pi)\,\delta(r-1) + B\,\theta(r-1)\,(r-1)^{-\alpha} \tag{5.3.3a}$$

$$N_\sigma(r) = \frac{1}{\sqrt{2\,\pi\,\sigma^2}}\,\exp\left(-r^2/(2\,\sigma^2)\right) \tag{5.3.3b}$$

where $\delta(r)$ is the Dirac-delta function and $\theta(r)$ is the Heaviside step function (0 for $r < 0$, 1 for $r > 0$) and r is expressed in units of d. Then the measured radial distribution function, $g(r)$, is the convolution of these:

$$g(r) = \int_0^\infty \tilde{g}(\rho)\,N_\sigma(r-\rho)\,d\rho \tag{5.3.4a}$$

$$= \frac{1}{\sqrt{2\,\pi\,\sigma^2}}\int_0^\infty \left[\frac{Z}{2\,\pi}\,\delta(\rho-1) + B\,\theta(\rho-1)\,(\rho-1)^{-\alpha}\right] e^{-\frac{r^2}{2\,\sigma^2}}\,d\rho \tag{5.3.4b}$$

Here we diverge from Aste et al.'s method of analysis noting that it is not strictly possible to obtain σ from fitting a normal distribution to $g(r)$ for $r < d$ because the convolution causes some of the number density from the power-law term to spill over to $r < d$. This in turn leads to a systematic overestimation of the height of the delta function and hence an overestimation of Z. Instead we go the direct route solving this integral numerically and fitting that solution directly to the $g(r)$ data to estimate parameters Z, B, α and σ. Fig. 5.8C shows that the $g(r)$ data are well fit by these equations at all volume fractions with none of the parameter estimates showing any meaningful dependence on volume fraction. If we average over the estimates at the four volume fractions and take the standard deviation as an estimate of the error, the fit estimates are $Z = 4.0(4)$, $B = 0.31(5)$, $\alpha = 0.58(8)$ and $\sigma = 0.0141(5)$. Note that

this analysis provides a meaningfully lower estimate of Z than the volume-dependent range 5.81 and 6.97 seen previously [5] and with corresponding differences in estimates for α. We believe that this difference is due to the differing analysis.

So $g(r)$ in this system is well fit by Eqs. 5.3.3 and 5.3.4 and is consistent with the high-friction isostaticity prediction that $Z = 4$ which has also been seen in simulations at RLP [85]. This analysis also shows the experimental $g(r)$ to be consistent with a power-law divergence of near misses with exponent $-1/2$. It is impossible to claim more than consistency here because there is a substantial interdependence of the parameter estimates, particularly between Z and α. This can be seen in Fig. 5.8 where higher than average estimates of α always pair with lower than average estimates of Z.

The high quality of this fit means that the local environment out past a distance $0.3\,d$ from a given sphere's surface is consistent with the following radial distribution function

$$g(r) = Z/(4\,\pi)\,\delta(r-1) + B\,\theta(r-1)\,(r-1)^{-\alpha}\ , \tag{5.3.5}$$

again letting $d = 1$. The local structure is thus composed of the sum of two extremely sharp distributions. Nowhere is the structure uniformly distributed at the average number density, $\rho = g_\infty$.

Surely this sharp local structure in $g(r)$ must have consequences for the shape of $g(r)$ beyond $r \approx 1.3\,d$. Neighbors after all also have the same sharply peaked $g(r)$ in their immediate neighborhood so there must be an echo of the first peak in $g(r)$ at larger r. In one-dimension the ringing of the sharply peaked feature at $r = d$ would logically occur at integer multiples of d, $r = 1\,d,\ 2\,d,\ 3\,d$.... The next question is whether we can predict the period of the ringing in 3D.

The Ornstein-Zernicke (OZ) equation provides a means to separate $g(r)$ into "direct," $c(r)$, and "indirect" terms [68]. Let $\bar{g}(r) = \frac{1}{\rho}\,(g(r) - \rho)$,

$$\bar{g}(r) = c(r) + \int c(|\boldsymbol{r} - \boldsymbol{r'}|)\, \rho\, \bar{g}(r')\, d\boldsymbol{r'} \tag{5.3.6}$$

where the integral is over all allowable positions $\boldsymbol{r'}$ of a third sphere. This equation defines the direct correlation, $c(r)$, which can be thought of as the direct influence of the sphere at the origin on the structure at r and the indirect term (the integral) can be thought of as the sum over indirect influences of the sphere at the origin on the structure at r mediated by a third particle at $\boldsymbol{r'}$. There are truncation methods to solve the OZ equation like the Percus-Yevick approximation [71] which has an analytic solution for hard spheres [93], however, we are interested in the consequences that the sharp initial peak has on $g(r)$ in a non-equilibrium granular packing rather than in the equilibrium solution.

Athermal hard-spheres only interact by contact, so we take the form of the direct correlation function to be from its contacting neighbors at $r = 1$ (again letting $d = 1$),

$$c(r) = Z/(4\,\pi)\, \delta(r - 1) \tag{5.3.7}$$

Having a form of the direct correlation function, the principle difficulty in solving the OZ equation is in confining the integral to run only over positions, $\boldsymbol{r'}$, that do not overlap the sphere at $r = 0$. This constraint can be written explicitly with a function, $T(r')$, that is 0 for $r' < d$ and 1 otherwise, allowing the equation to be written as a convolution and transformed to Fourier space:

$$\bar{g}(r) = c(r) + \int c(|\boldsymbol{r} - \boldsymbol{r'}|)\, \rho\, \bar{g}(r')\, T(r')\, d\boldsymbol{r'} \tag{5.3.8}$$

$$= c(r) + \rho\, \text{convolve}(c,\ \bar{g}\, T) \tag{5.3.9}$$

$$F\,[\bar{g}] = F\,[c] + \rho\, F\,[c]\ F\,[\bar{g}\, T] \tag{5.3.10}$$

Were $T = 1$, it would be straightforward to solve for the Fourier transform of $\bar{g}$,

$$F[\bar{g}] = F[c]/(1 - \rho F[c]) \ . \tag{5.3.11}$$

An approximate solution, however, can be obtained by approximating T as a spatial low-pass filter over distance, d, which transforms to a frequency-space cutoff of d/L where L is the length of system over which the transform is taken. In this approximation the Fourier transform of $\bar{g}$ is equal to $F[c]$ for frequencies below the cutoff and is given by Eq. 5.3.11 above the cutoff. This approximation should be expected to have significant errors for $r < d$ but be valid for $r >> d$ which is the region of interest where we which to see the consequences of sharp features at $r = d$. Indeed behavior for $r \gtrsim 1.5\,d$ are not sensitive to the value of the frequency cutoff (see Sect. C.1 in the appendix) but there are significant errors visible for $r < d$ including broadening of the delta function to the left of $r = d$ and a peak at the origin.

In Fig. 5.9 the OZ equation has been solved assuming the direct correlation comes only from true contacts. The only inputs into this model are the average number of contacts, Z, and the volume fraction, ϕ. The numerical solution for $Z = 4$ contacts captures the decreasing frequency of peaks and troughs, however, it underestimates the amplitude of the peaks and troughs. The numerical solution for $Z = 5$ matches the amplitude and period of the peaks and valleys and their growth with increasing volume fraction. A similar solution can be obtained with $Z = 4$ by including some of the distribution of near-misses near $r = d$ (see Fig. C.2 in Sect. C.1).

The oscillations in $g(r)$ after the first peak at $r = d$ thus are explained as a ringing of the sharp feature at $r = d$ echoing in the neighbors of neighbors and so forth. Nearly the entire shape of $g(r)$ appears to be a consequence of the local distributions of contacts and near-misses. This OZ solution does not, however, appear to capture the splitting of the $r \approx 2\,d$ peak with increasing volume fraction suggesting that this feature is not a consequence of local structure.

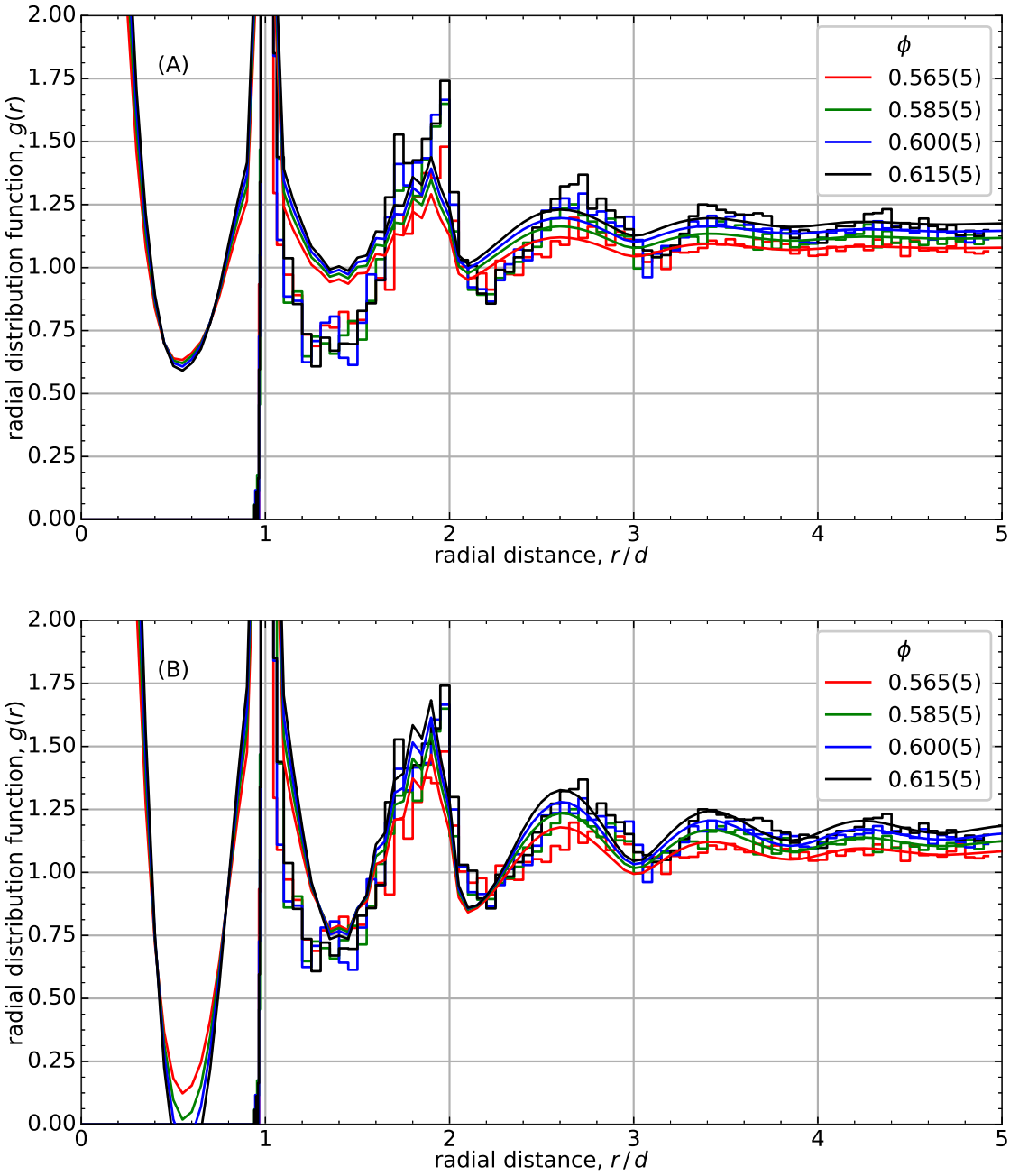

Figure 5.9: Radial distribution function data (binned plots) and numerics (smooth): Numerics are 3D numerical solutions of the Ornstein-Zernicke (OZ) equation assuming a direct correlation function coming solely from the contact number. The only input parameters are the volume fraction, ϕ, and the coordination number, Z, set to 4 in (A) and 5 in (B). Because of computational limits the granularity of the numerical solution ($0.025\,d$) is larger than the $0.014\,d$ smoothing found in the data. Solutions at both $Z = 4$ and 5 match the locations of peaks and troughs in the $g(r)$ data, however, the $Z = 5$ solutions is overall a much better match. Even the volume fraction dependence appears to be captured. Thus much of the structure of $g(r)$ appears to be dictated by the delta sharp peak at $r = d$.

It is also interesting to observe that the decreasing period in $g(r)$ appears to be linked to dimensionality as we have argued that it should simply be equal to d in 1-dimension, is lower in 2D (Fig. C.1) and still lower in 3D.

5.3.3 Voronoi and Delaunay partitions

As volume is the key property in loose packings, it is interesting to look at local measures of volume fraction. This is typically done via Delaunay and Voronoi partitions which can be computed efficiently with algorithms for finding convex hulls.

A "Delaunay tessellation" partitions space into simplices with vertices at the centers of nearest neighboring particles. In D-dimensions a simplex is a polygon with $D + 1$ vertices so in 2D the simplices are triangles and in 3D they are tetrahedra. Strictly, simplex vertices are chosen so that no other particle center lies within the circumcircle or circumsphere through the vertices of the simplex. Degeneracy where more than $D + 1$ particle centers lie on the same sphere occurs frequently in ideal periodic lattices but with probability zero in the presence of noise.

Voronoi diagrams share the same nearest-neighbor relationships with Delaunay tessellations but are typically thought of as the partition of space into regions around each particle. For a given particle, i, the Voronoi cell surrounding i is the set of all points $\vec{x}$ such that $\vec{x}$ is closer to i than to any other particle. Voronoi cells are generally thought of as a robust quantity, however, they inherit the ambiguity of defining neighbors when Delaunay tessellations are degenerate and often fail to form closed surfaces about particles near the boundary.

In Fig. 5.11 we show distributions of volumes of Delaunay tetrahedra and Voronoi cells that lie in the interior which we define to mean that the Voronoi cell does not intersect the boundary and is at least $3\,d$ away from a wall (increasing this distance farther does not have a noticeable effect on the shape of the distributions). Distributions consists of the "free volume" which is the volume not containing a sphere, the

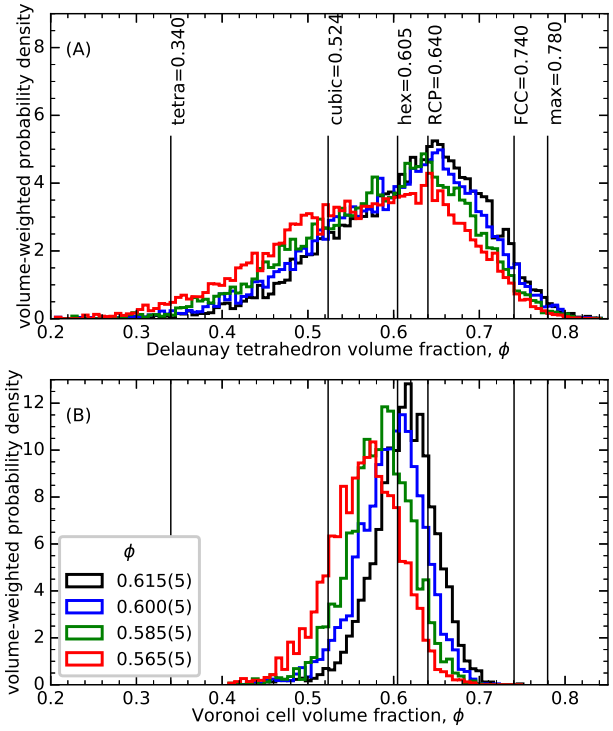

Figure 5.10: Volume-weighted distributions of local volume fraction from Delaunay and Voronoi partitions: included are interior cells that are at least a distance $3\,d$ from a wall. (A) contains the volume fractions of Delaunay tetrahedra and (B) the volume fractions of individual Voronoi cells. The range of volume fractions seen in Delaunay tetrahedra is very broad spanning the range of average volume fractions seen for common regular lattices from the tetrahedral-octahedral honeycomb lattice past close packed lattices such like FCC and right up to the maximum possible local volume fraction for a Delaunay tetrahedron of ≈ 0.78 on the inside of a tetrahedron of four mutually contacting spheres. The volume-weighting makes the means of these histograms equal to the mean volume fraction of the sample which come out to 0.566(5), 0.586(5), 0.600(5), 0.614(5) which, when rounded to the nearest 0.005 give the nominal volume fractions that quote in the figures. The errors are estimated from a sum of causes with systematic uncertainty of the sphere radii contributing 0.002, sensitivity to the distance excluded from the wall contributing an uncertainty of order 0.001 and an additional 0.001 to 0.002 coming from the statistical uncertainty of estimating the mean of these distributions which are comprised of 2930, 3041, 3132 and 3213 Voronoi cells and 10327, 10489, 10707 and 10877 Delaunay tetrahedra, respectively.

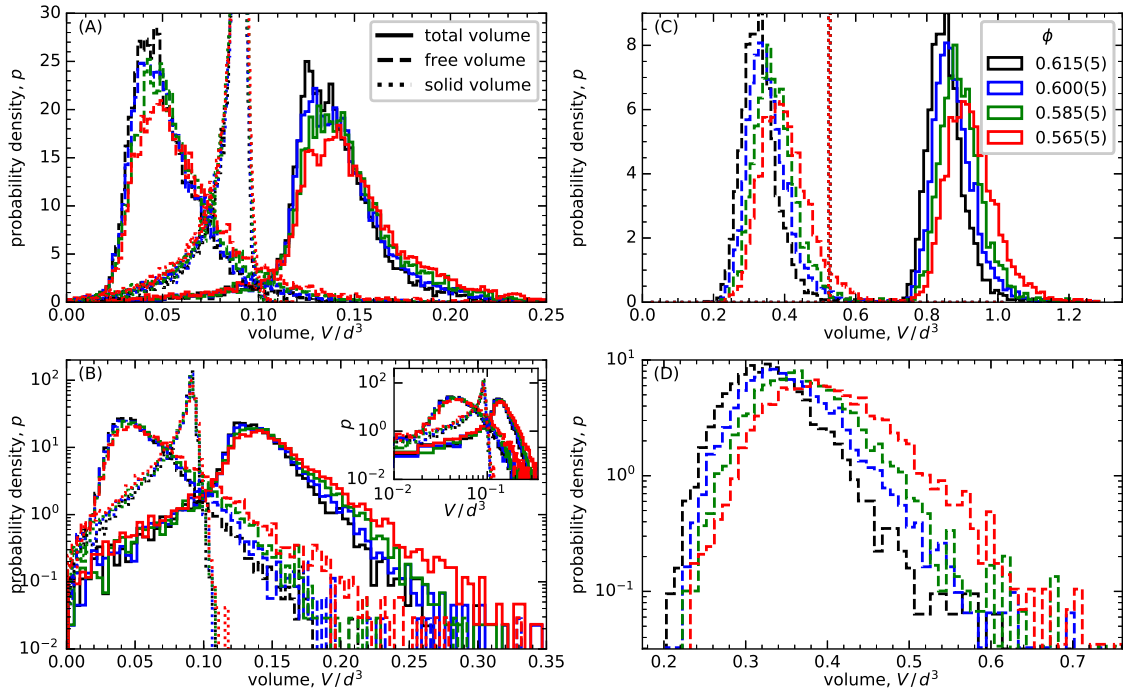

Figure 5.11: Distribution of local Delaunay volumes (left) and Voronoi volumes (right): Plotted are the distributions of the "free volume" of Delaunay tetrahedra and Voronoi cells which is the volume not containing a sphere, "solid volume" which is the volume of sphere within the cell and "total volume" which is the sum of these. For Delaunay tetrahedra these are three distinct distributions with the distribution of free volumes possessing exponential tails on both sides, the distribution of sphere volumes sharply peaked with a heavy tail at small V and a short tail to the right of its peak. The distribution of total volumes incorporates properties of both. meaning that the free volume and total volume distributions have distinct shapes in the Delaunay tessellation. The situation is simpler for Voronoi cells where the solid volume is constant—the volume of a single sphere—and thus has a delta function distribution. The distributions of volumes and free volumes have the same shape and are simply shifted relative to one another and so only the free volume distribution is plotted on the semi-log axes. All volume and free volume distributions have exponential tails consistent with $p(v) \sim \exp(-\beta v)$ at large-v.

"solid volume" which is the volume of sphere within the cell and the "total volume" which is the sum of these. In the Voronoi case, each Voronoi cell contains a single, whole particle and thus the solid volume is constant, $4/3\,\pi\,(1/2)^3$ (since $d = 1$), and the distributions of free volumes and total volumes therefore differ only by an offset. This is also the case for Delaunay volumes in two dimensions: the interior angles of a triangle always sum to π so the solid area in a Delaunay triangle is always half the area of a particle. This is not the case in three dimensions, however: the sum of the solid angles in a tetrahedron is not constant so the distribution of solid volumes in the Delaunay tessellation, although sharply peaked, is not guaranteed to be a delta function. Instead we find that it possesses a heavy small-v tail. This heavy small-v tail carries over to the total volume so whereas the distributions of free volumes in the Delaunay and Voronoi partitions look similar, the shapes of the total volume distributions differ qualitatively in the small-v tail.

The shape of volume distributions is of particular interest to theoretical Edwards volume distributions and related models which seek statistical mechanics descriptions with volume replacing the role of energy in equilibrium theory. The differences between distributions of volume and free volume in Delaunay tessellation in three dimensions may be of interest to such theories, however, of particular interest is the degree to which volume distributions resemble the Boltzmann distribution, $P(V) \sim \exp(-\beta\, v)$. As observed elsewhere in a similar system [3], none of these distributions as a whole follow this shape, however, the large-v tails do. We follow the lead of Aste [3] introducing the "complementary cumulative density function," ccdf, to quantify the shape of the large-v tails of these distributions. If $p(v)$ is the normalized probability density function, then the cumulative density function, $\mathrm{cdf}(v) = \int_{-\infty}^{v} p(v')\,dv'$, represents the accumulation of probability up to v. The complementary cumulative density function, $\mathrm{ccdf}(v) = 1 - \mathrm{cdf}(v)$, flips this over to highlight the large-v tail. For a probability distribution, $p(v)$, with an exponential tail at large-v, the ccdf will have

the same exponential tail, but it will be better suited to plotting on logarithmic axes far into the tail where the histogram of $p(v)$ encounters empty bins.

Fig. 5.12(A) shows the complementary cumulative probability distributions or "tail distributions" for volume distributions of Delaunay and Voronoi partitions with the mean volumes subtracted to allow better comparison of the tails. We observe that the tails appear quite linear for both Delaunay and Voronoi partitions consistent with the Boltzmann form $p(v) \sim \exp(-\beta\, v)$ seen in [3] and anticipated in Edwards volume-ensemble theories. The slopes of these tails vary with volume fractions (Fig. 5.12(B), inset) and differ by about a factor of two between the Delaunay and Voronoi partitions suggesting that the "granular temperature" in the Edwards volume-ensemble theory is significantly higher for the Voronoi partition than for the Delaunay partition. We are seeing a larger discrepancy than the roughly 20% difference reported by Aste. As he noted Ref. [3], this poses the question to volume-ensemble theories of which volume partition is the appropriate way to measure volume locally.

That these tails are Boltzmann-like at all remains encouraging for Edwards volume-ensemble theories. Wondering if such exponential tails are a predictable artifact of calculating Voronoi and Delaunay partitions on noisy data, we added pseudo-random Gaussian noise to our sphere location data then re-ran the Voronoi and Delaunay algorithms. The result is that adding small amounts of noise has little effect and that adding large amplitude noise makes the tails bend downward like the tails of a Gaussian distribution. Random point sets also produce volume distributions with Gaussian rather than Boltzmann tails. Thus whatever origin of the Boltzmann tails in the data, they do not appear to be an artifact of detection noise which we have reason to believe is Gaussian (Sect. 5.3.2).

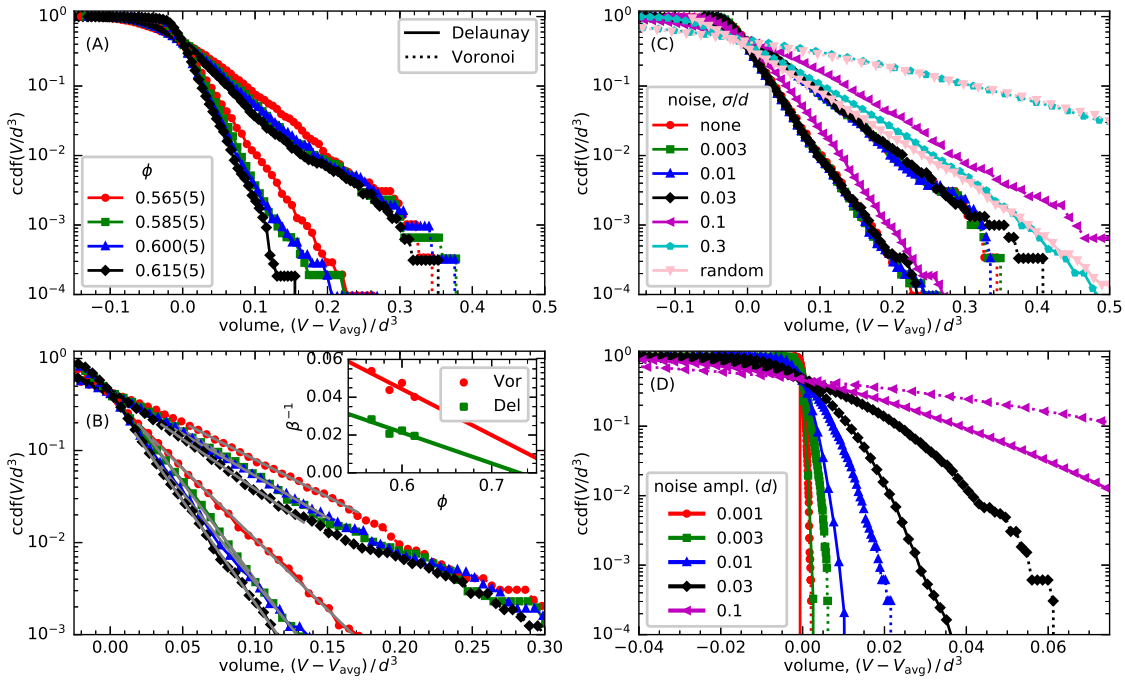

Figure 5.12: Delaunay and Voronoi volume tail distributions centered at the mean. (A) the complementary cumulative probability distribution, ccfd$(v) = 1 - \mathrm{cdf}(v)$, of the distribution of Delaunay volumes possesses an exponential or Boltzmann tail at all volume fractions, however, the tails of the distributions of Voronoi volumes become less linear with increasing volume fraction. In (B) the linear portions are magnified and least-squares fits to the probability distribution of form, $p(v) \sim \exp(-\beta\, v)$ at large-v where $v = (V - V_{\mathrm{mean}})/d^3$ are added in gray. The inset plots the reciprocal of the slope, β^{-1}, versus volume fraction and fails to reproduce the collapse seen in [5] with a linear trend extrapolating to volume fraction near ϕ_{RCP}. The right column explores the role of noise in shaping these distributions. (C) shows the ccdf for partitions computed after adding normally distributed noise to the sphere locations in the lowest volume fraction sample as well as the tails for a randomly generated point set of the same number density as (A). Small amounts of noise, even when larger than the $\sigma = 0.014\, d$ estimated from $g(r)$, have little effect on the tails large amounts make the tail less linear. (D) shows the tails for partitions computed for an FCC plus differing levels of normally distributed noise (note that hard-sphere constrains are violated here) In all of these cases, randomness appears to make the tails less linear by bending them down like the tails of a normal distribution which is opposite what is happening to the tails of the Voronoi volume distribution at higher volume fractions.

5.3.4 Hole size distribution

One quantity of interest that can be calculated from the Delaunay triangulation is the size of the voids in the material. Whereas Voronoi cells define the space nearest to a given sphere, a Delaunay tetrahedron encloses slices of four neighboring spheres and the void region between them. The size of voids can be obtained from the circumsphere through the centers of each Delaunay tetrahedron. The size of the largest sphere that can fit in the void can then be calculated by subtracting the d from the circumsphere's diameter. That no other spheres impinge on this void is guaranteed by the definition of the Delaunay partition which states that no other sphere's center can lie within the circumsphere.

Thus it is possible to calculate a maximal void diameter for each Delaunay cell, however, the statistics of this distribution are complicated by the fact that void spaces often overlap in the sense that multiple Delaunay simplices can surround the same void area. Thus there is a possible issue with over-counting certain voids. To show that over-counting is not a huge effect, in Fig. 5.13 we show distributions of hole sizes counted one per Delaunay tetrahedron and also weighted by the volume of the tetrahedron. These different weighings result in a minor but noticeable difference.

As volume fraction increases, the void size distributions shift to smaller d_{void} and become somewhat narrower. The narrowing of the distribution may reflect that it is beginning to push up against dense packing (e.g. FCC or HCP) where half of the voids are the smallest possible being inside four touching spheres with void diameter, $d_{\text{void}} \approx 0.225\,d$, and the other half have diameter: $\approx 0.414\,d$. The tails of the distribution are also interesting with the large-d_{void} tail appearing somewhat heavier than Gaussian, however, the trend would appear to steepen approaching the sphere diameter, d_{void}, as we do not detect any holes large enough to fit a sphere. The small d_{void} tail is also interesting and appears to approach the smallest possible void size, $d_{\text{tetra}} \approx 0.225\,d$, up to detection accuracy, as a power-law with exponent near 1.

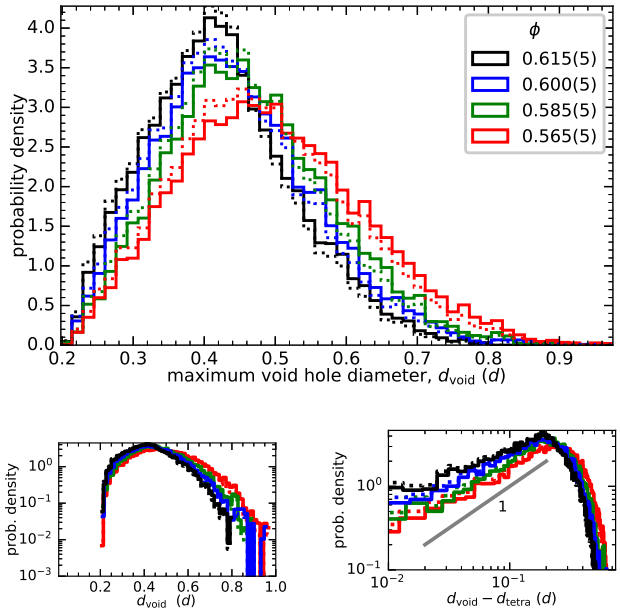

Figure 5.13: Sizes of voids: The largest sphere that can fit in a void space between particles can be computed from the circumsphere through the sphere centers in each tetrahedron in the Delaunay tessellation. The distributions plotted here show that voids large enough to fit a sphere ($d_{\text{void}} \geq d$) do not exist at any of the volume fractions scanned. Because multiple small Delaunay tetrahedra can possess the same circumsphere in degenerate Delaunay tessellations, we display the hole-diameter distribution counted per Delaunay tetrahedron (dashed lines) and weighted by the volume of the tetrahedron (solid lines). Bottom panel: The shape of the large-d_{void} tail in the distribution of hole sizes is not completely clear, yet even if it is no heavier than a normal distribution, the extrapolating the trend would predict that we should see some sphere-sized or larger holes, especially at the lowest volume fraction, yet none are detected in the bulk. In the bottom-right, the horizontal axis has been shifted by the smallest possible void diameter for uniform hard-spheres, corresponding to the void formed by four mutually contacting spheres, $d_{\text{tetra}} \approx 0.225\, d$. Above detection error, the shape of the tail is approximately that of a power-law with exponent one.

5.3.5 Crystalline order parameters

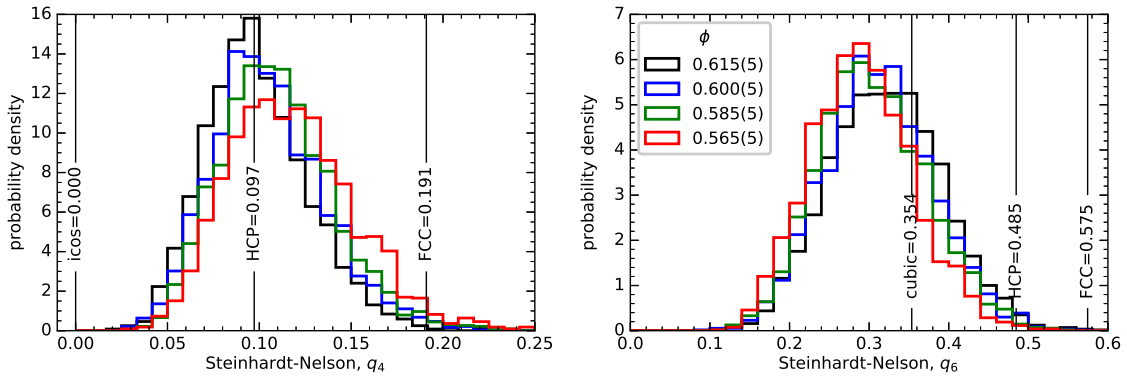

Figure 5.14: Distributions of local Steinhardt-Nelson order parameters calculated on Voronoi neighbor bonds: Order parameters are calculated only for Voronoi cells that are on the interior of the packing and at least $3\,d$ away from the nearest wall. The distribution of q_4 shifts toward zero with increasing volume fraction. The distribution of the q_6 is significantly more broad and shifts the opposite way.

One method for characterizing order which has proven particularly useful for measuring crystalline order is the set of q_n-crystalline order parameters of Steinhardt, Nelson and Ronchetti [88]. Many measures of crystalline structure rely on prior knowledge of the orientations of the crystalline axes. This poses difficulties when analyzing materials with many randomly aligned crystalline regions or materials lacking long range order such as liquids or glasses. One solution is to look for rotationally invariant measures of order.

In two dimensions one could imagine looking at the angles of the bonds surrounding a particle. The values of each angle depend on the orientation of the axes, however, a different choice of axes gives the same set of angles up to an additive constant (modulo $2\,\pi$). To quantify the pattern

$$f(\theta) = \sum_{j=1}^{n} \delta(\theta - \theta_j) \tag{5.3.12}$$

of these bonds to neighboring particles, $\{j\}$, one could take a discrete Fourier transform

$$\hat{f}_n = \int_0^{2\pi} e^{i\,n\,\theta}\, f(\theta)\, d\theta \tag{5.3.13}$$

to obtain Fourier coefficients, $\hat{f}_n$, which for $n > 1$ depend on the choice of axes only for their phase. Normalizing these a little differently and taking the absolute value,

$$f_n(i) = \frac{1}{N_i} \Big| \sum_{j=1}^{N_i} e^{i\,n\,\theta_{i\,j}} \Big| \tag{5.3.14}$$

yields a set of rotationally invariant order parameters, f_n, for $n > 1$ and we have informally introduced the Nelson-Halperin 2D crystalline order parameters [61]. It is immediately clear that these f_n will be useful for locating crystalline regions. A square lattice uniquely has $f_4 = 1$ and $f_{n\neq 4} = 0$ and a honeycomb lattice uniquely has $f_6 = 1$, $f_{n\neq 6} = 0$. So the f_n provide a means of detecting crystalline regions without needing to know the orientation of the crystalline axes as well as a sensitive way of differentiating between different crystalline lattices.

The Steinhardt-Nelson q-parameters generalize these crystalline bond-order parameters to three dimensions, providing a rotationally invariant way to measure crystalline order in an arrangement of three-dimensional bonds. In 3D the sum over bonds to neighbors, $\{j\}$, looks like:

$$f(\theta, \phi) = \sum_{j=1}^{n} \frac{1}{\sin\theta}\, \delta(\theta - \theta_j)\, \delta(\phi - \phi_j) \tag{5.3.15}$$

and can be expanded in terms of spherical harmonics,

$$f(\theta, \phi) = \sum_{\ell=1}^{\ell_{max}} \sum_{m=-\ell}^{\ell} \hat{f}_{\ell m}\, Y_{\ell m}(\theta, \phi) \tag{5.3.16}$$

with orthogonality allowing a solution for the coefficients,

$$\hat{f}_{\ell m} = \int_0^{2\,\pi} \int_0^{\pi} f(\theta, \phi)\, Y^*_{\ell m}(\theta, \phi) \sin(\theta)\, d\theta\, d\phi \tag{5.3.17}$$

These coefficients are analogous to those from a Fourier transform in the 2d case except for the presence of a second index, m, that runs from $-\ell$ to ℓ. All that remains is to convert these tensors into a rotationally invariant scalar. This can be done two ways to obtain order parameters q_n or w_n [88], the latter being less used. We will only consider the q_n which can be computed,

$$\bar{q}_{\ell\, m}(i) = \frac{1}{N_i} \sum_{j=1}^{N_i} Y_{\ell\, m}(\vec{r}_{i\, j}) \tag{5.3.18a}$$

$$q_n(i) = \sqrt{\frac{4\,\pi}{2\,n+1} \sum_{m=-n}^{n} |\bar{q}_{n,m}(i)|^2}\ , \tag{5.3.18b}$$

with the sum in the first equation running over the bonds from the i'th particle to its N_i neighbors, $\{j\}$.

As periodic lattices must have 2, 3, 4 or 6-fold symmetry, the q_n corresponding to these, and particularly q_4 and q_6, are typically the most used in identifying crystalline regions. The Fourier transform analogy holds, however, in that there is no reason that other q_n cannot be present and these can provide information about the local structure of disordered materials.

In order to calculate the local values of q_n from Eq. 5.3.18, one must first define nearest neighbor bonds over which to evaluate the sum. Probably the most meaningful way to do this in disordered packings would be to sum over contacts. Unfortunately experimental error and the divergence of near misses make this impossible to do experimentally from particle positions alone. Contacts not being known, one typical choice is to sum over Voronoi neighbors which, however, includes many neighbors that are relatively remote and obviously not contacts. The other option is to choose

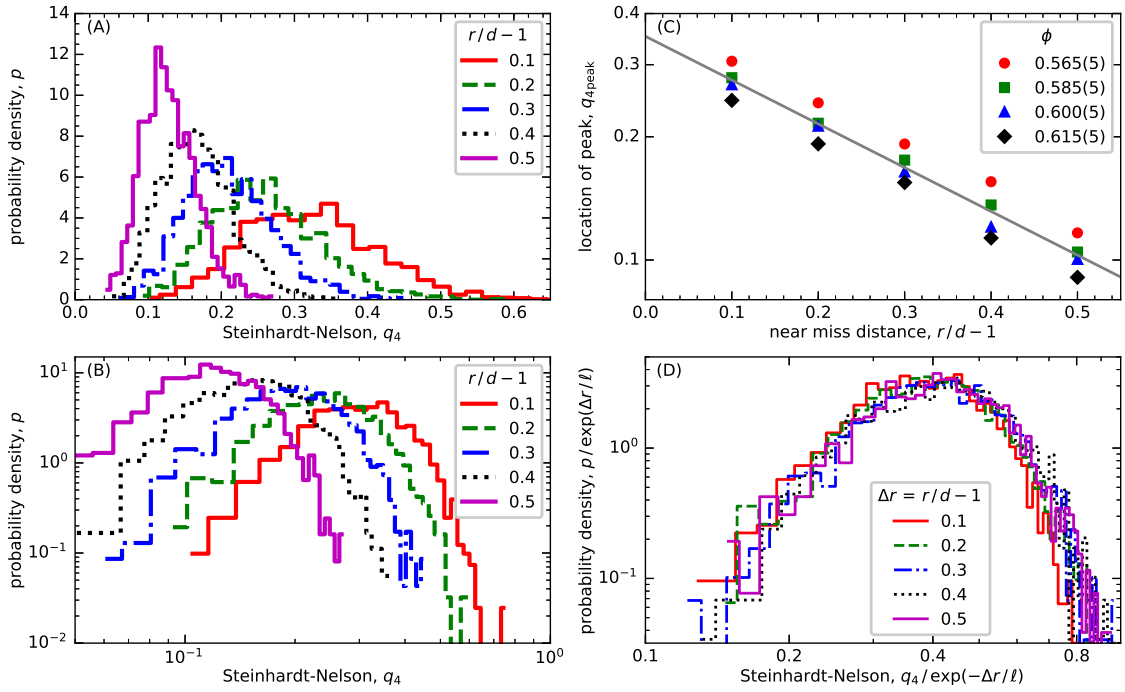

Figure 5.15: Distribution of q_4 order parameter calculated locally over bonds to neighbors within varying distances: (A) and (B) display the distributions q_4 calculated locally at the lowest volume fraction, $\phi \approx 0.565(5)$. (C) displays the location of the peak probability versus the distance over which bonds are included. This dependence is well fit by an exponential decay with characteristic distance $\ell = 0.41(3)\,d$. (D) shows the distributions at the lowest volume fraction collapsed by the fit in (C). The distributions appear to possess the shape of a log-normal distribution.

a distance slightly above the sphere diameter and sum over neighbors within that distance. As we will demonstrate, the results depend quite a bit on how the neighbors are chosen.

Fig. 5.14 shows distributions of q_4 and q_6 calculated over Voronoi neighbors. The q_4 distribution has a maximum at ≈ 0.1 and q_6 at ≈ 0.3 which makes them roughly equivalent to the distributions calculated out to a radial distance of $1.5\,d$ as shown in Figs. 5.15 and 5.16. The latter figures show that as the radius over which bonds are included increases, the peaks of the distributions decrease. The q_6 distribution largely maintains its shape and width while the distribution of q_4 changes as it collapses onto a single log-normal distribution. The trend of decreasing means with increasing radius

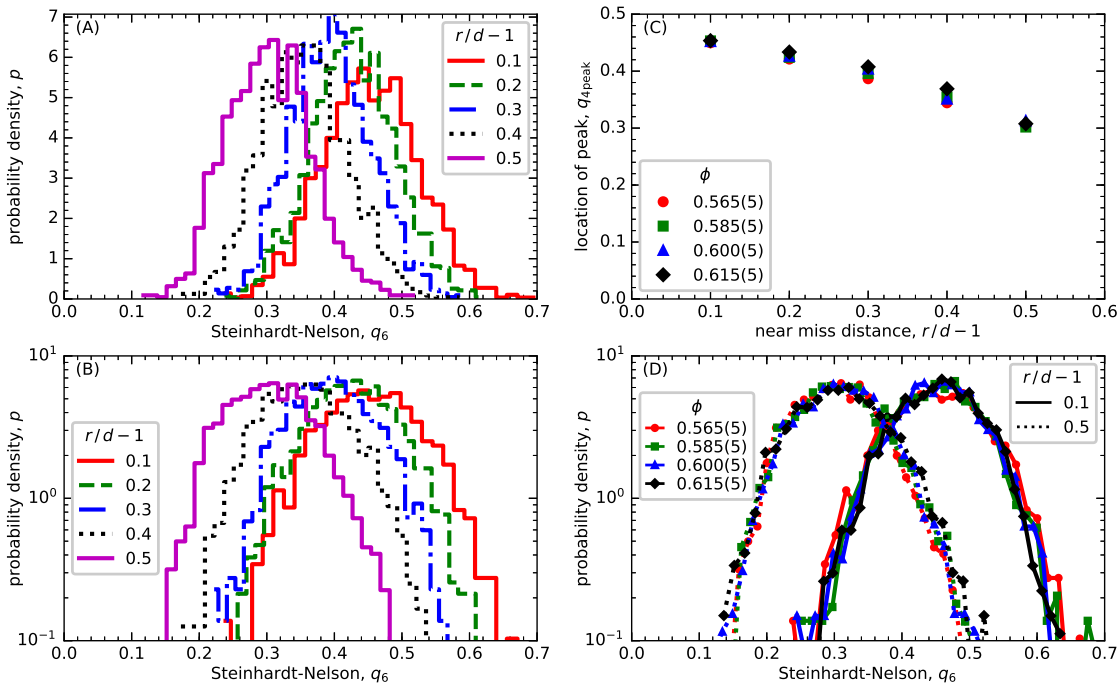

Figure 5.16: Distribution of q_6 order parameter calculated locally over bonds to neighbors within varying distances: (A) and (B) display the distributions q_6 calculated locally at the lowest volume fraction, $\phi \approx 0.565(5)$, (D) for the highest volume fraction, $\phi \approx 0.615(5)$. (C) displays the location of the peak probability versus the distance over which bonds are included. (D) shows the distributions at all volume fractions at two values of $r/d-1$. Unlike the q_4 distributions which appear to be log-normal, the q_6 distributions are all approximately normal distributions with the same widths.

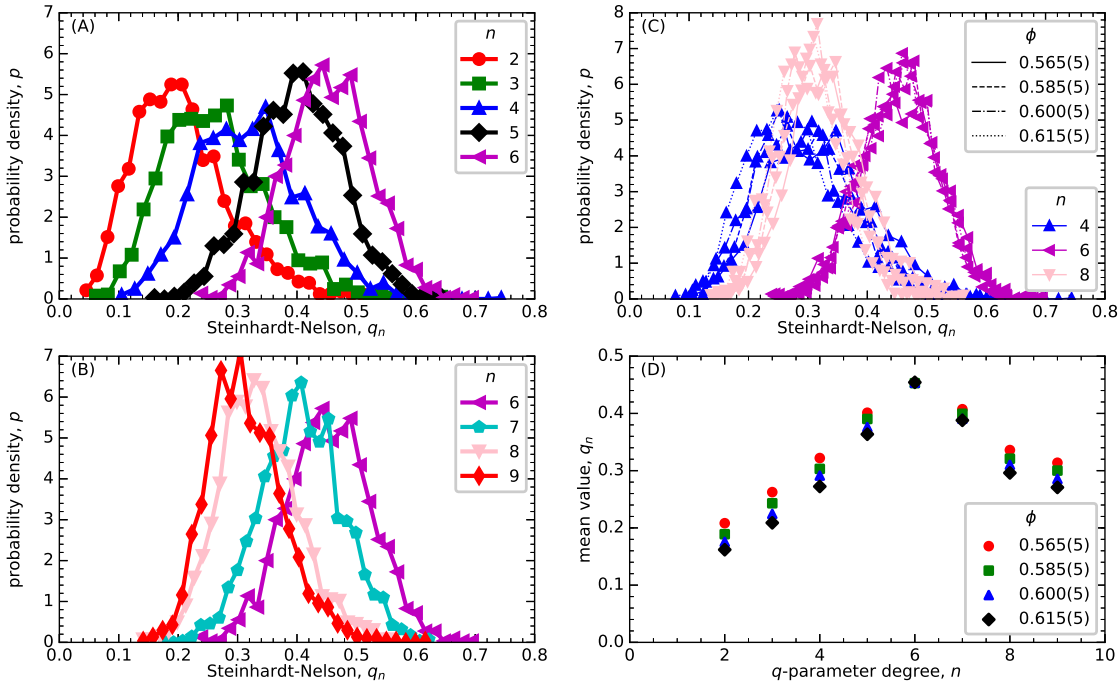

Figure 5.17: Distributions of Steinhardt-Nelson q_n-order parameters calculated locally over bonds to neighbors out to distance $1.1\,d$: (A) and (B) show the order parameters calculated at the lowest volume fraction, $\phi = 0.565(5)$. The means of these distribution increase with increasing n up to $n = 6$ and subsequently begin to decrease. (C) shows the distributions for three of these order parameters at all four volume fractions. (D) plots the means of these distributions versus the degree, n, of the order parameters. q_6 appears to be special as it is both the order parameter with the largest mean value and also the one that changes least with volume fraction.

is in the expected direction. Including ever more distant bonds should ultimately make the q-parameters tend toward zero if the material is isotropic.

It is possible to calculate the q_n at any integer value of n and while only certain values are consistent with periodic lattices, all of these values denote n-degree symmetry locally in a disordered packing. Fig. 5.17 plots the distributions of the q_n from $n = 2$ to 9, summing over neighbors out to $1.1d$. Among these order parameters q_6 is special: it is both the distribution with the highest mean and the distribution that shifts least with volume fraction. q_4, by contrast, looks simply like the intermediate step between q_3 and q_5.

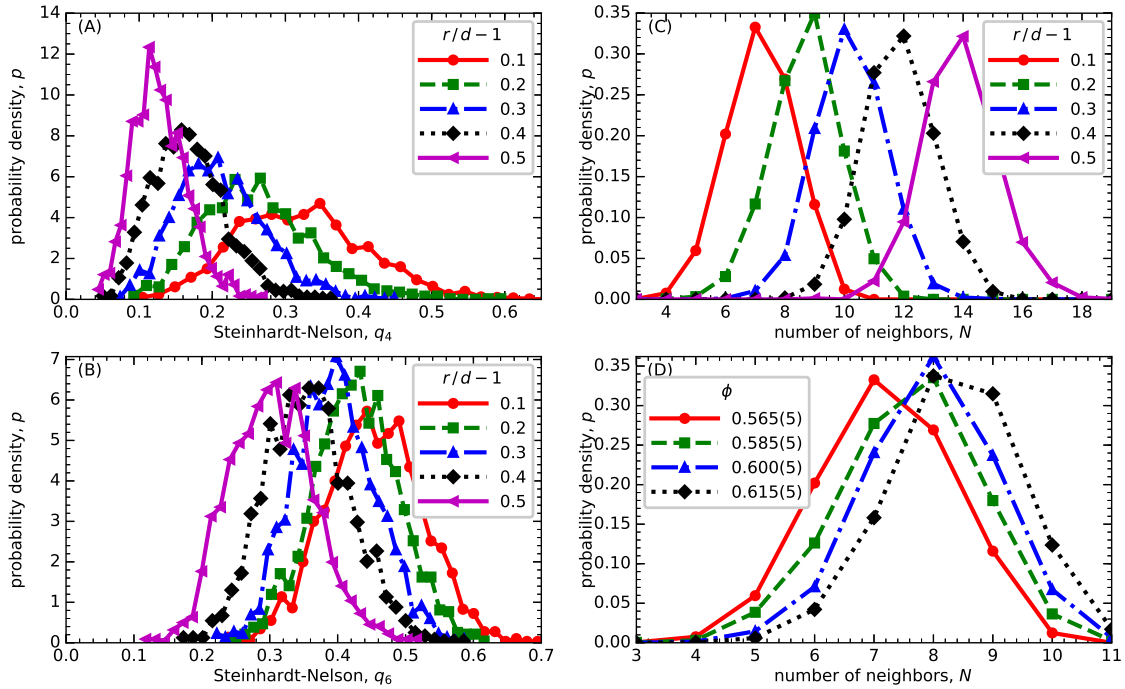

Figure 5.18: Distributions of local Steinhardt-Nelson order parameters and the number of neighbors out to maximum radial distances, r: (A) shows q_4 calculated over bonds to various distances and (B) shows the distributions of q_6. (C) shows the number of neighbors within these distances at the lowest volume fraction, $\phi \approx 0.565$. (D) shows the dependence of volume fraction at for neighbors counted out to $r = 1.1\,d$.

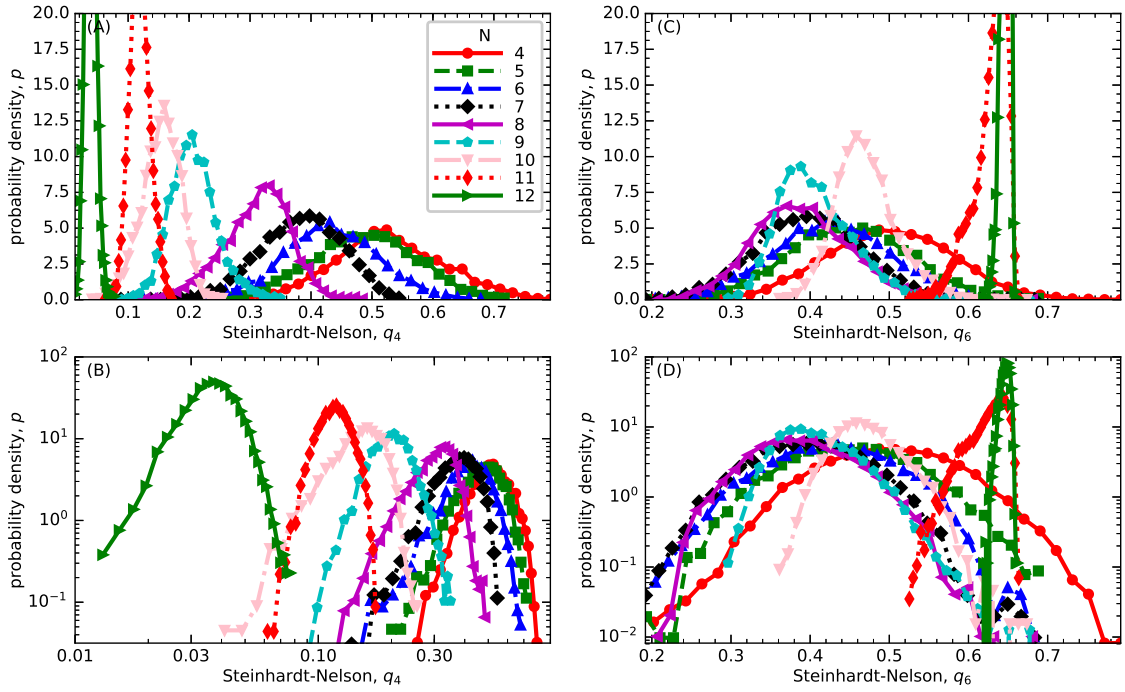

Figure 5.19: Distributions of Steinhardt-Nelson order parameters from Monte-Carlo simulation of a single sphere with N contacting neighbors: The left column shows q_4 with the distributions having the log-normal shape seen in the data. The right column shows q_6 with the distributions for $N < 11$ having approximately the normal distributions seen in the data.

To see if the local structure captured by the crystalline order parameters follows simply from hard-sphere constraints between neighboring spheres, we performed Monte-Carlo calculations where a single sphere is surrounded by a cloud of N contacts (see Sect. C.2 for the details of the simulation). Calculating the local bond-order parameters from the Monte-Carlo, we obtain distributions of q_4 and q_6 for fixed N (Fig. 5.19). We know the distribution of the number of neighbors in the data from Fig. 5.18, so it is possible to sample the fixed N Monte-Carlo results according to the experimental distribution of N. The predictions this gives are shown in the left column of Fig. 5.20. The distribution of q_4 in the data at the lowest volume fraction where the average of N is 7.2 resembles a combination of the Monte-Carlo distributions at $N = 7$ and 8 which is reasonable. Further, the low-q_4 tail matches the

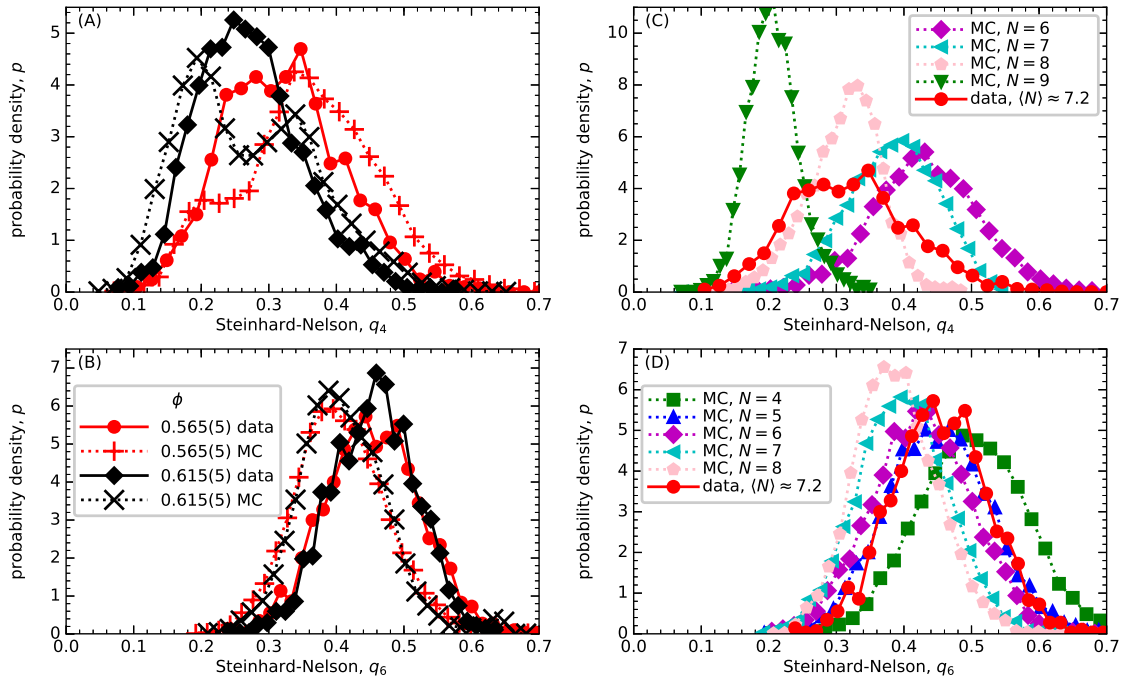

Figure 5.20: Comparison of distribution of q_4 and q_6 with those generated by Monte-Carlo: The left column shows the data (solid lines) for the lowest and highest volume fraction and the distributions of order parameters when the constant-N Monte-Carlo distributions (Fig. 5.19) states are sampled according to distribution of N measured in the data (Fig. 5.18). In the data shown here the q_n and the number of neighbors are calculated out to radius $1.1\,d$. The Monte-Carlo captures the low-q_4 tail of the q_4 distribution but misses significantly otherwise is offset relative to the observed q_6 distribution. The right column plots the distribution at the lowest volume fraction alongside Monte-Carlo distributions at surrounding values of N. The average number of neighbors within $1.1\,d$ in the data is 7.2 at the lowest volume fraction (it is 7.6, 8.0, 8.4 at the higher volume fractions) and we see that the low-q_4 tail in the data matches the low-q_4 tail in the Monte-Carlo at $N = 8$ which is reasonable. The shape of the experimental q_4 distribution could reasonably be seen to arise from a sum of the $N = 7$ and $N = 8$ distributions alone without evidence of the $N = 6$ and $N = 9$ distributions which were included in (A). The correspondence is less good for q_6 with the experimental distribution best resembling the Monte-Carlo at $N = 5$. The q_6 structure these does not seem to follow solely from the number of neighbors and hard-sphere constraints.

Monte-Carlo at $N = 8$, but when we weight by the frequency of these N's in the data, the result (Fig. 5.20(A)) seems to incorporate too much of the $N = 8$ and 9 distributions. Thus it is conceivable that certain parts of the q_4 structure such as the low-q_4 tail are captured by the Monte-Carlo and therefore determined simply by hard-sphere constraints and the number of neighbors.

The distribution of q_6 is less well reproduced by the Monte Carlo. At the lowest volume fraction the experimental distribution which has $< N >= 7.2$ best matches the Monte-Carlo at $N = 5$ and this correspondence gets worse with increasing volume fraction since $< N >$ increases while the q_6 distribution changes little. The structure signified by q_6 seems not to follow solely from the number of neighbors, hard-sphere constraints and the assumption that all else is random.

5.3.6 Spatial correlations on the Voronoi Partition

We have looked at distributions of scalars defined locally and spatial dependence of these. Now we explore spatial correlations between scalars that can be defined locally on the Voronoi diagram, focusing on the volume fraction of Voronoi cells, ϕ, and the crystalline order parameters q_4 and q_6.

To compute spatial correlations, we first compute the Voronoi partition. Volume fractions are computed for the Voronoi cells about each sphere and q_4 and q_6 are computed for bonds about that sphere, as before either summing over Voronoi neighbors or neighbors within a set radius. Then, defining the values of scalars $\phi(\boldsymbol{r})$, $q_4(\boldsymbol{r})$ and $q_6(\boldsymbol{r})$ to be constant in each Voronoi cell, the spatial dependencies of these scalars are digitized onto a $0.2\,d \times 0.2\,d \times 0.2\,d$ spaced grid without any smoothing or interpolation. Spatial cross-correlations are computed and the average radial component extracted.

The ranges of the autocorrelations computed this way are very short, falling essentially to zero by a distance of $2\,d$ (Fig. 5.21). The autocorrelation length of ϕ

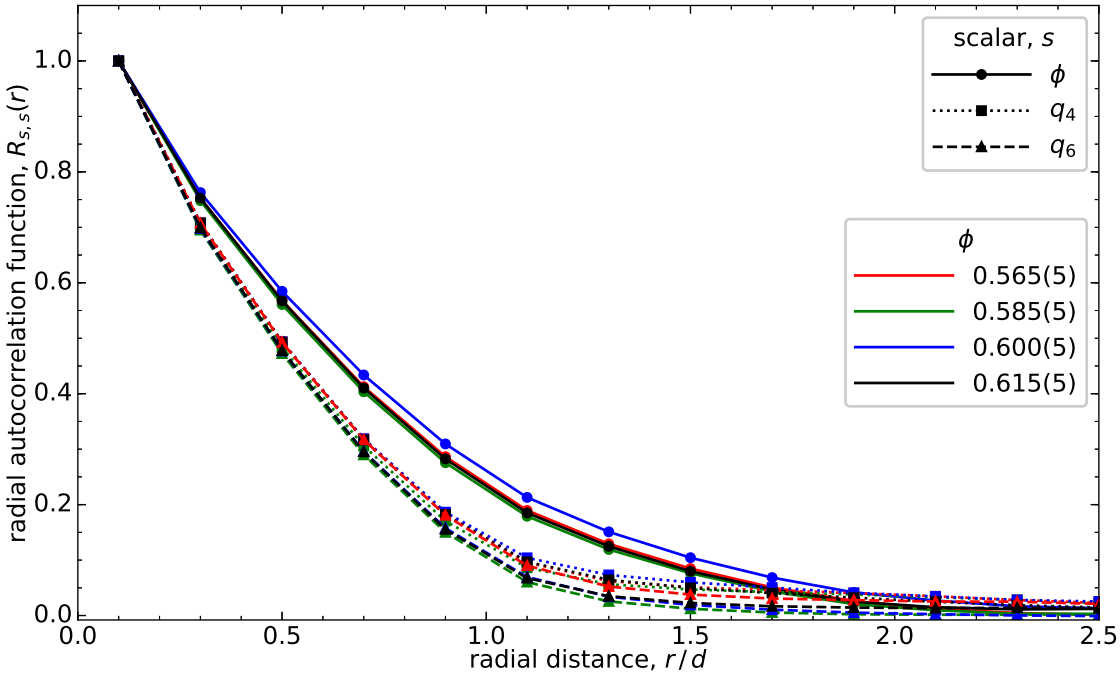

Figure 5.21: Spatial auto-correlations of scalars defined on the Voronoi partition digitized onto a $0.2\,d \times 0.2\,d \times 0.2\,d$ spaced grid. The autocorrelation lengths are short for all three scalars, the autocorrelation length of ϕ being somewhat longer than those of the crystalline order parameters. There is little change with volume fraction.

is somewhat longer than for q_4 and q_6, showing little variation with average volume fraction.

Cross-correlations contain more features (Fig. 5.22). Even the values of the correlation coefficient at $r = 0$ are non-trivial with there being a significant positive correlation between ϕ and q_6 and a smaller negative correlation between ϕ and q_4 (Fig. 5.22). The shapes of the cross-correlation in Fig. 5.22(A) in which q_4 and q_6 are summed over Voronoi neighbors are also interesting with the cross-correlation between q_4 and q_6 changing sign from $r = 0$ to $r \approx d$. All of these features, however, appear to depend on the region over which the q_n are calculated and choosing the Voronoi cell as that region seems to give results that are not in line with any region defined by a radius. This being true, there is a trend toward negative cross-correlation between ϕ and both q_4 and q_6 at $r = 0$ as the radius over which bonds the q_n are summed goes to d. This is interesting because it is the opposite of what one would expect if the q's where signaling crystalline order which would be expected to increase volume fraction.

5.4 Discussion

The first function of the structural analysis in this chapter is to assess the plausibility of the working assumptions of homogeneity and isotropy made in the previous chapters. To address homogeneity we look at the spatial dependence of local volume fraction and the Steinhardt-Nelson crystalline order parameters which are found to be uniform in the bulk. The absence of a measurable dependence on height suggests that the imaged portion of the packing is deep enough that any vertical dependence has saturated [47]. The distribution of bond angles relative to coordinate axes was also found to be consistent with expectations for an isotropic material. We did see signs of layering near the walls, however, it is short ranged and is not accompanied by a measurable increase in crystalline order parameters suggesting that the pres-

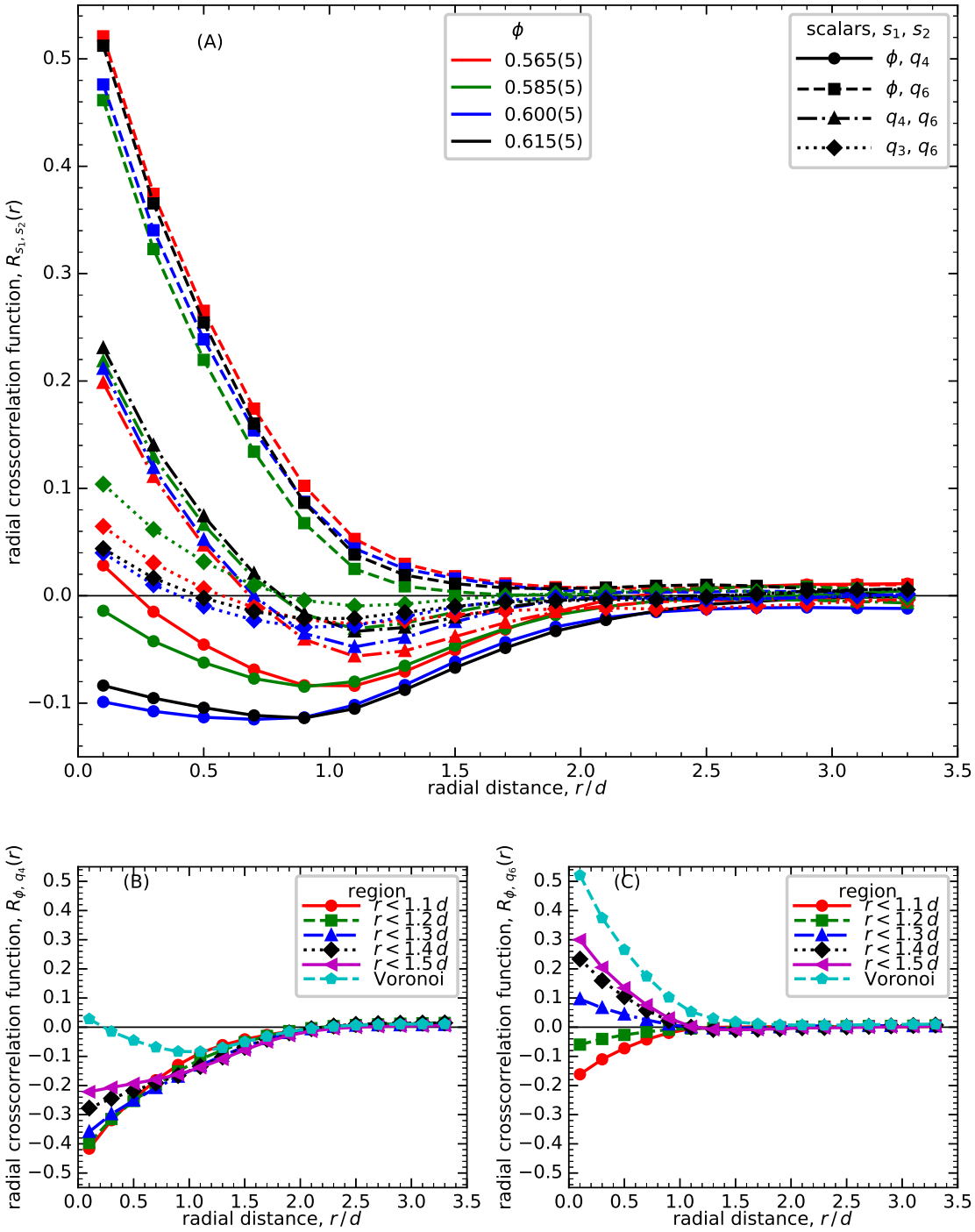

Figure 5.22: Spatial cross-correlations on the Voronoi partition at all four volume fractions: (A) shows the cross-correlations calculated between these scalars when q_4 and q_6 are calculated over bonds to Voronoi neighbors. In (B) cross-correlation of ϕ and q_4 where q_4 is calculated over different sets of neighbors within varying radii for the lowest volume fraction sample. (C) shows the equivalent cross-correlation for ϕ and q_6. The local correlation between volume fraction and bond order parameters depends qualitatively on the region over which bond order is calculated, changing in both magnitude and sign.

ence of layering does not imply that the structure is crystalline near the walls. The walls were, however, found to have a short ranged negative influence on the volume fraction. This is counter to the expectations from denser packings where walls tend to act as templates for crystalline regions. Thus the walls do not appear to be driving crystalline order and while they do induce layering, that effect is relatively short ranged (3 to 4 sphere diameters), leaving the packing homogeneous in the bulk.

Partitioning the packing into Voronoi and Delaunay diagrams, we observe that free-volume distributions have Boltzmann tails as predicted for Edwards free-volume distributions [35], however, with even more distinct slopes for Delaunay and Voronoi free-volume distributions than has been reported previously [5]. We demonstrate that these exponential tails are real in the sense that they are not artifacts of computing Voronoi and Delaunay partitions on noisy data. This would seem to be promising for free-volume theories, however, it does demand an explanation of why these two volume partitions appear to possess different "granular temperatures."

Through the Delaunay partition we also obtain the distribution of maximum void sizes. We find that none of the voids are large enough to fit a particle which is of relevance to grand-canonical ensemble versions of free-volume theories: the insertion probability may be very small.

We also look at properties of the Steinhard-Nelson q-crystalline order parameters finding that the distributions of these order parameters have different shapes with q_4's being log-normal and q_6's approximately normal. Both shift depending on the distance over which bonds to neighbors are included in the sums calculating their parameters. Comparing these to a broader range of q_n distributions, we see that q_6 is special in two ways as it has the largest mean and changes the least with bulk volume fraction. In fact the plot of the mean value of q_n versus n resembles a resonance with peak at $n = 6$, making six-fold symmetry a dominant mode of sorts. That six-fold structure should also be the structure that changes least with volume fraction is

puzzling. At the very least this argues against the formation of face-centered cubic crystals being the primary means of compaction, since that would be expected to increase q_6 more than other modes.

To try to understand the origins of the structure of neighbor locations encoded in the q_4 and q_6 distributions, we perform Monte-Carlo simulation of single spheres. These simulations which calculate q_4 and q_6 distributions assuming N contracts arranged randomly subject to hard sphere constraints, reproduce some of the features of the q_4 distribution but fail to match the q_6 distribution. Thus the q_6 distribution is signaling the presence of structure in the arrangement of neighbors that does not follow solely from the number of neighbors and hard-sphere constraints.

We also explore spatial correlations of local volume fraction, q_4 and q_6, finding all auto-correlations and cross-correlations to be short ranged, falling off completely after a distance of 1 or 2 particles. There are interesting correlation coefficients at $r = 0$, revealing an anti-correlation between local volume fraction and the values of crystalline order parameters q_4 and q_6. The anti-correlation with volume fraction together with the lack of crystal growth at the walls and the lack of change in q_6 with the volume fraction of the system, point toward the conclusion that crystalline regions, however small, are not apt to form in loose packings and their growth is not the mechanism by which volume fraction increases either locally or globally.

We also look at structure via the radial distribution function, and by directly fitting $g(r)$ near the peak at $r \approx d$ find better agreement with predictions of the isostaticity hypothesis and simulations [86] than had previously been seen in experimental data [4, 5]. The quality of the fits in Fig. 5.8 to Eq. 5.3.4 suggest that locally $g(r)$ is composed of only two distributions, that of true contacts at $r = d$ and divergent power-law distribution of near-misses. Both of these distributions are sharply peaked at $r = d$ so there is nowhere locally where structure is even remotely uniform at the average number density. Such a sharply peaked feature at $r = d$ must have

consequences for the longer ranged shape of $g(r)$. The Ornstein-Zernicke (OZ) equation provides a means to split $g(r)$ into direct and indirect components. We show numerically that the presence of a sharp peak at $r = d$ predicts the decreasing period of peaks and troughs at larger r and their growth with volume fraction. The local distributions of contacts and near misses therefore determine much of the overall radial distribution—that is the entirety of structure in an isotropic material to the level of two-particle correlations. The numerics from the OZ equation do not appear to reproduce the splitting of the peak at $r \approx 2$. Thus the growth of the $\sqrt{3}\,d$ peak in $g(r)$ appears to be the only feature of radial structure that does not arise as a direct consequence of very short ranged order.

CHAPTER 6

CONCLUSION

We began the work presented in this dissertation addressing the question of uniqueness of Onoda and Liniger's [67] random loose packing limit of $\phi_{\mathrm{RLP}} \approx 0.555$ which they obtained in the limit of neutral buoyancy and whether their limit of neutral buoyancy should be understood as the limit where particle weight drops below cohesive force scales or whether it could be interpreted as the limit of slowing dynamics freezing the packing in a fragile state.

We found that such a limit did exist but that it was not unique in the sense that different material spheres went to different limits. Thus in the work described in Chapter 2 we were the first to closely characterize the spherical grains used in granular packing experiments. Likely the details of grains had been neglected previously because the surface of the spheres matters little at RCP: ϕ_{RCP} is the same at infinite friction as it is at zero friction [85]. It turns out that these details do matter in looser packing and we showed that surface properties manifest as a friction coefficient and spheres with higher friction coefficients formed looser RLP packings. So we had answered uniqueness: ϕ_{RLP} was not uniquely 0.555 because that exact number depends on friction.

The second question remained: was the limit of neutral buoyancy a comparison with a force scale or was it part of a dynamic parameter? We measured upper bounds on the interparticle cohesive forces then chose fluids such that the weight of the spheres was never comparable to those forces. Subject to that constraint we varied the density and dynamic viscosity of the interstitial fluids and found that we could

collapse sedimented volume fractions against a single parameter combination: Stokes number. This was the parameter we had suspected would control the dynamics of packing since it could be written as the ratio of the kinetic and gravitational energy scales of a sedimenting sphere. The surprise was that we were obtaining a loose packing limit too early: low volume fractions were obtained at $St \approx 10$. Interpreted as the ratio of kinetic energy to potential energy that seemed like quite enough energy to disrupt a fragile state. It turns out that we had guessed the right parameter but for the wrong reason. The Stokes number also controls the restitution coefficient [28] and that is the dynamic parameter that mattered.

To return to the uniqueness question: we showed that RLP is not unique because it depends on friction but is it a unique function of friction? Specifically, is it unique if one were to decouple the two roles of Stokes number? Is the RLP limit achieved by taking the restitution coefficient to zero at constant deposition energy the same as the limit of zero deposition energy at constant restitution coefficient?

This is a question that we were not able to experimentally address. The next section lays out a conjecture we were not able to test regarding the radial distribution function and the final section lays out what we do and do not understand about the rheology of loose grains.

6.1 Radial Structure

Short ranges are a theme in our investigation of structure. Auto-correlation and cross-correlation lengths are very short and even the effect of walls suppressing volume fraction is found to be short ranged.

The importance of short ranges is perhaps most striking in the radial distribution function. By directly fitting $g(r)$ near the peak at $r \approx d$ we found better agreement with predictions of the isostaticity hypothesis and simulations [86] than had previously been seen in experimental data [4, 5]. We demonstrated that for radial distances

near the sphere diameter, $g(r)$ can be decomposed into two contributions coming from contacts and near-misses, both of these distributions sharply peaked right at the surface of the central sphere. We then showed with a numerical solution of the Ornstein-Zernicke equation that these sharply peaked local structures determine much of the behavior of the radial distribution function at all distances.

A hypothesis of ours that we did not have occasion to test experimentally relates to the local picture of structure. $g(r)$ comes from two distributions near $r = d$, both peaked at $r = d$: the distribution of contacts and the distribution of near-misses. The near-miss distribution has form $(r - d)^{-\alpha}$ for $r > d$ with values seen in simulation of $\alpha \approx 1/2$ [86, 65] and ≈ 0.4 [32]. Our data are consistent with $\alpha = 1/2$. Where does this fractional exponent come from and how does the near-miss distribution "know" to peak so sharply (divergently in fact) at the sphere diameter? Our suspicion is that the near-miss distribution is comprised of former contacts. Loose packings are a dissipative highly damped system: the Stokes number is low (much less than ten) so spheres do not bounce after collisions. Further, the spheres are cohesionless so that tension is not supported. All these factors point toward contacts failing primarily by sliding apart along the tangent plane at the point of contact rather than by being pulled apart. If one assumes that contacts break by sliding a random distance along their common tangent plane and that this random distance is from a broad enough distribution to be flat about zero, the reciprocal square-root shape of the near-miss distribution $\sim 1/\sqrt{r - d}$ follows immediately (see Appendix Section C.3).

If true, this broken-contacts explanation of the near-miss distribution would be important because the distribution of near-misses is thought to relate to the coordination number scaling of Eq. 1.5.1 [65]. It would also mean that nearly all of the radial structure at RLP follows from isostaticity and some assumptions about the history of packing formation. Isostaticity would give the delta function at $r = d$ and the broken-contacts hypothesis would give the divergent near-miss distribution. Since

these sharply peaked distributions are sufficient to make up the radial distribution at small separation and the sharp feature near $r = d$ largely controls the structure at larger separations via the self-consistency enforced by the Ornstein-Zernicke equation, much of the radial distribution would be explained. It is not until volume fraction increases above RLP and a peak appears at $r \approx \sqrt{3}\,d$ that there would be signals of structure that is not a direct consequence of the local environment of the spheres.

6.2 Mechanics of Loose Packings

In Chapter 3 we presented mechanical responses of loose sphere packings displaying a number of unanticipated scalings, including the cube-root scaling of the yield stress with both strain-rate and the age of the packing. Together with our observation of power-law stress-relaxation at constant strain in the same system and the observation of logarithmic creep at constant stress elsewhere in a similar system [62], these responses to the three common modes of linear mechanical perturbation,

$$\sigma_y \sim (\dot{\gamma}\,T)^{1/3} \qquad \text{at constant strain-rate} \tag{6.2.1}$$

$$\sigma \sim t^{-1} \qquad \text{at constant strain} \tag{6.2.2}$$

$$\gamma \sim \log(t) \qquad \text{at constant stress} \tag{6.2.3}$$

describe a new mechanical phenomenology which we find can be unified by an extremely simple rheological model.

Since this material creeps at small steady stresses yet reacts like a solid at higher frequencies, the simplest rheology is that of a Maxwell fluid—a viscous element in series with an elastic element. Quantitatively this is all wrong though: creep should go like t not $\log t$ and what of the cube-root or the role of age, T? And the phenomenology of 6.2.1 does not just creep, it also ages. All of these questions are resolved if the

viscosity is understood to evolve. Expanded to lowest order in applied stress, σ, consistent with σ being a tensor and η a scalar,

$$\dot{\eta} \approx a + r\,\sigma^2, \tag{6.2.4}$$

(this is Eq. 4.4.3b where we let $G = 1$), all of the phenomena in Eq. 6.2.1 are accounted for. Thus we describe in a very general way a material that exhibits logarithmic creep, heavy-tailed relaxation and cube-root strain-rate-scaling of the yield stress. It is not hard to find other instances in the literature where very different systems exhibit similar scalings including similar cube-root strain-rate yield-stress scaling in polymers [74] and in a colloidal paste [31]. It may be that the rheological model of Eq. 3.5.7 of Chapter 2 arises quite commonly as a slow evolution regime in yield stress fluids and the cube-root may often be mistaken for a semi-log, $\sigma_0 + \sigma_1 \log \dot{\gamma}$.

It is not difficult to imagine adding additional terms to the expansion of $\dot{\eta}$. Finding that the symmetry between age and strain-rate breaks down abruptly after the yield point is passed, we introduce into the expansion a new timescale, τ, attempting now to expand the evolution of $\dot{\eta}$ to lowest order in τ and σ. We find that τ appears in the strain-rate dependence of multiple features, all related by the simple expansion in Eq. 4.4.5. We make no claim that these expansions are sufficient for every case: indeed, these equations only closely fit our data near extreme features where only a few terms are significant. One possibility is that the phenomenon is so complicated that every term consistent with symmetry is present and will be important in certain parameter regimes. It may be that in general it is useful to treat the elastic shear modulus, G, as evolving as well, however, we have not identified any phenomena that clearly demonstrate that this is happening.

Despite the successes of our rheological models, Eq. 3.5.7 and Eq. 4.4.5, much is not understood about this system. We have not identified the mechanisms of aging and rejuvenation represented by a and r terms, nor, do we understand the

origin of the strain-rate dependence of the timescale τ which becomes relevant beyond the yield point. To make matters worse, τ scales to different exponents in systems with different viscosities of the interstitial fluid. In the lower viscosity interstitial fluid system it displays $\tau \sim |\dot{\gamma}|^{-1}$ as would be expected in a quasi-static or rate-independent regime. Yet in the system with a higher viscosity interstitial fluid, τ is not scaled proportionally to the change in interstitial viscosities, instead it exhibits an altogether different exponent, $\tau \sim |\dot{\gamma}|^{-1/2}$, which itself demands a dimensional explanation. At present we have none to offer. Investigation of the origins of τ as well as the mechanisms behind aging and rejuvenation in this material are among the most pressing questions for future work.

APPENDIX A

FRICTION COEFFICIENT CALCULATION

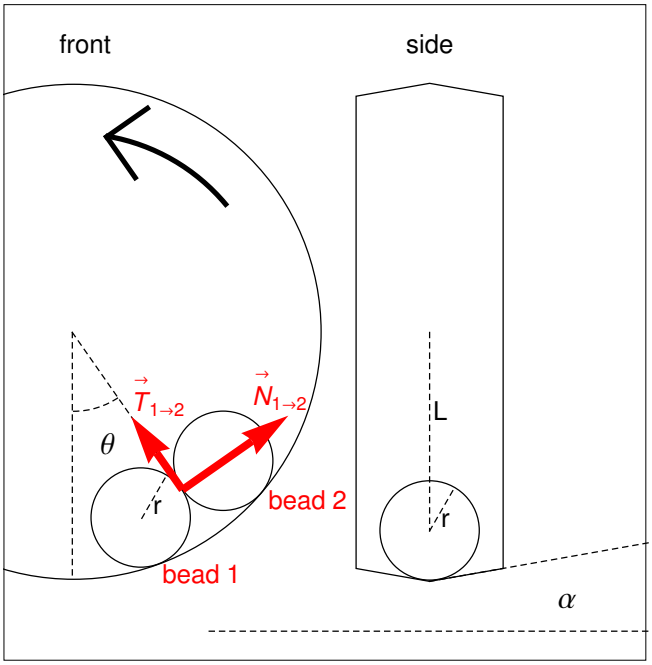

Figure A.1: Geometry of the apparatus used in the friction measurement (scale: bead radius $r = 1.59\,mm$).

In the limit of where we can ignore fluid effects and static rolling resistance, the friction measurement described in Chapter 3 might be described as a textbook problem on Lagrangian mechanics: "Two spheres of radius r roll without slipping in a vertical circular track of radius L. What is the maximum angle of stability of the two spheres if the coefficient of static friction between them is μ and the angle of the v-groove in the track is α." See Fig. A.1 for the diagram of the problem.

For convenience, define the following:

$$f \equiv r/L \tag{A.0.1}$$

$$s = r\ \cos\alpha \tag{A.0.2}$$

$$\theta_1 \equiv \theta - \sin^{-1} f \tag{A.0.3}$$

$$\theta_2 \equiv \theta + \sin^{-1} f \tag{A.0.4}$$

where the θ_i are the angle of the spheres individually in terms of the angle of the sphere–sphere contact point, θ. The parameter s is the length of the level–arm between the rotational axis of the spheres and the line on the v-groove of the cylindrical track where the spheres make contact.

We can write the θ_i in terms of the angles of rotation of the beads about their centers, γ_i:

$$\theta_i = \frac{s}{L+s}\,\gamma_i \tag{A.0.5}$$

Now let us write the two constraints at the point of contact between spheres. Constraint 1) impenetrability implies spheres move the same amount:

$$d\theta_2 - d\theta_1 = 0 \tag{A.0.6}$$

$$\theta_2 - \theta_1 = \text{const} \tag{A.0.7}$$

$$\frac{s}{L+s}\,(\gamma_2 - \gamma_1) = c_1 \tag{A.0.8}$$

Constraint 2) no slipping between beads implies average position is constant:

$$\gamma_2 + \gamma_1 = \text{const} \tag{A.0.9}$$

Since we are interested in the friction force applied tangent to the surface at radial distance r (lever arm of length r), we write:

$$r(\gamma_2 + \gamma_1) = c_2 \tag{A.0.10}$$

so that the Lagrange multiplier will be the force, F, tangent to the surface.

Let us now write the Lagrangian, $\mathcal{L}$:

$$\mathcal{L} = m\,g\,L\,(\cos\theta_2 + \cos\theta_1) \tag{A.0.11}$$

$$= m\,g\,L\,\left(\cos\left[\frac{r}{r+L}\gamma_2\right] + \cos\left[\frac{r}{r+L}\gamma_1\right]\right) \tag{A.0.12}$$

The Euler–Lagrange equations are:

$$-\frac{\partial\mathcal{L}}{\partial\gamma_i} = \tau\,\frac{\partial}{\partial\gamma_i}\,\frac{s}{L+s}(\gamma_2 - \gamma_1) + F\,\frac{\partial}{\partial\gamma_i}\,r(\gamma_2 + \gamma_1) \tag{A.0.13}$$

Where Lagrange multipliers τ and F represent torque about the center of the cylinder and the frictional force btween spheres, respectively. Expanding the Euler–Lagrange equations, we have:

$$\frac{m\,g\,L\,r}{L+r}\sin\theta_1 = \frac{-s}{L+s} + F\,r \tag{A.0.14}$$

$$\frac{m\,g\,L\,r}{L+r}\sin\theta_2 = \frac{s}{L+s} + F\,r \tag{A.0.15}$$

Solving for the Lagrange multipliers,

$$F = \frac{m\,g\,L}{2(L+r)}(\sin\theta_2 + \sin\theta_1) \tag{A.0.16}$$

$$\tau = \frac{m\,g\,L\,r\,(L+s)}{2(L+r)s}(\sin\theta_2 - \sin\theta_1) \tag{A.0.17}$$

It will be convenient later to reexpress these in terms of θ, substituting $\theta_1 \to \theta - \sin^{-1} f$ and $\theta_2 \to \theta + \sin^{-1} f$ and making use of obscure trigonometric identities, we have

$$F = \frac{\sqrt{1-f^2}\, g\, m\, s}{f\,(L+s)}\, \sin\theta \tag{A.0.18}$$

$$\tau = L\, f\, g\, m\, \cos\theta \tag{A.0.19}$$

The Langrange multiplier τ which we interpret as a torque about the center of the cylinder is related to the normal force, N, between spheres by a lever–arm of length, a (Note that $a < L$).

$$a = L\, \cos\sin^{-1} f = \sqrt{1-f^2}\, L \tag{A.0.20}$$

$$\tau = a\, N \tag{A.0.21}$$

We are now in a position to solve for the coefficient of friction, μ.

$$\mu = F/N = a\, F/\tau = \sqrt{1-f^2}\, L\, F/\tau \tag{A.0.22}$$

$$= -\frac{(f^2-1)s\, \tan\theta}{f^2\,(L+s)} \tag{A.0.23}$$

$$= \frac{(L/r)^2 - 1}{L/s+1}\, \tan\theta \tag{A.0.24}$$

APPENDIX B

EXTENDED MAXWELL MODEL CALCULATIONS AND NUMERICS

B.1 Analytic Results

B.1.1 Yield-stress Scaling Calculation

Our modification of the Maxwell model of viscoelasticity to describe the solid regime of loose sphere packings relates the evolution of viscosity to stress history:

$$\dot{\gamma} = \frac{\dot{\sigma}}{G} + \frac{\sigma}{\eta} \tag{B.1.1a}$$

$$\frac{\dot{\eta}}{G} = a - r\left(\frac{\sigma}{G}\right)^2 \tag{B.1.1b}$$

where dimensionless constants a and r tune the respective strengths of aging and shear-rejuvenation in the material.

In this section we carry the analysis of the location of the stress maxima presented in Sect. 3.5 to higher order to obtain an estimate of the error associated with the scalings of Eq. 3.5.12. We follow the same general approach of obtaining approximate solutions for $\sigma(t)$ and $\eta(t)$ valid at small-t, then solving for the time, t_y, when they satify

$$\sigma(t_y) = \dot{\gamma}\,\eta(t_y) \tag{B.1.2}$$

which must be true at the peak (see argument for Eq. 3.5.10).

Seeking power-series solutions to Eq. B.1.1 consistent with initial conditions, $\sigma(0) = 0$ and $\eta(t) = a\,G\,T$ (Eq. 3.5.3b), we obtain

$$\sigma(t)/G \approx \dot{\gamma}\,t - \frac{\dot{\gamma}}{2\,a\,T}\,t^2 + \frac{(1+2\,a)\,\dot{\gamma}}{6\,a^2\,T^2}\,t^3 - \frac{\dot{\gamma}\,(1+5\,a+6\,a^2)}{24\,a^3\,T^3}\,t^4 \tag{B.1.3a}$$

$$\eta(t)/G \approx a\,T + a\,t - \frac{r\,\dot{\gamma}^2}{3}\,t^3 + \frac{r\,\dot{\gamma}^2}{4\,a\,T}\,t^4\ . \tag{B.1.3b}$$

Plugging the power-series solutions into the relation at the peak, $\sigma(t_y) = \dot{\gamma}\,\eta(t_y)$, produces a relation for the yield time, t_y:

$$\begin{aligned} 0 = 24\,a^4 + 24\,(a^4 - a^3)\,(t_y/T) + 12\,a^2\,(t_y/T)^2 - (4\,a + 8\,a^2 + 8\,a^3\,r\,T^2\,\dot{\gamma}^2)\,(t_y/T)^3 \\ +(1 + 5\,a + 6\,a^2 + 6\,a^2\,r\,T^2\,\dot{\gamma}^2)\,(t_y/T)^4 \end{aligned} \tag{B.1.4}$$

If t_y/T is small, then the 0'th-order term and the last part of the 3rd-order term dominate and we are left with the same relation for yield time, t_y as before:

$$0 = 24\,a^4 - 8\,a^3\,r\,T^2\,\dot{\gamma}^2\,(t_y/T)^3\ . \tag{B.1.5}$$

We can self-consistently judge how large the discarded terms are relative to the 3rd-order term using the scaling for t_y (Eq. B.1.6). If $a \sim 1$, all turn out to be higher order in $t_y/T \sim (r\,\dot{\gamma}^2\,T^2)^{-1/3}$.

The scaling of t_y follows from Eq. B.1.5,

$$t_y \approx \left(\frac{3\,a\,T}{r\,\dot{\gamma}^2}\right)^{1/3}\ . \tag{B.1.6}$$

Cube-root scaling of the yield strain follows from this and the constant strain rate ($\gamma_y = \dot{\gamma}\,t_y$),

$$\gamma_y \approx \left(\frac{3\,a\,T\,\dot{\gamma}}{r}\right)^{1/3}\ . \tag{B.1.7}$$

The yield-stress scaling requires a first order approximation of $\sigma(t)$ from Eq. B.1.3, i.e. $\sigma(t) \approx G\,\dot{\gamma}\,t$,

$$\sigma_y \approx G\left(\frac{3\,a\,T\,\dot{\gamma}}{r}\right)^{1/3} \tag{B.1.8}$$

Including the 2nd-order term in the power-series for $\sigma(t)$ adds another term to σ_y

$$G\left(\frac{3^2}{2\,a\;r^2\,T\,\dot{\gamma}}\right)^{1/3} \tag{B.1.9}$$

which is also small when $\sqrt{r}\,\dot{\gamma}\,T$ is large or t_y/T is small.

An interesting reciprocal-square-root dependence on t_y emerges when we eliminate $\dot{\gamma}$:

$$\sigma_y \approx G\left(\frac{3\,a\,T}{r\,t_y}\right)^{1/2} \tag{B.1.10a}$$

$$\gamma_y \approx \left(\frac{3\,a\,T}{r\,t_y}\right)^{1/2}\ . \tag{B.1.10b}$$

B.1.2 Generalized Maxwell Model for Arbitrary Power-Law Potential

In the standard 1-dimensional Maxwell model, viscoelastic response is modeled as a solid which responds to stress as a Hookean spring in series with a viscous fluid modeled as a viscous damper dashpot:

$$\dot{\gamma} = \frac{\dot{\sigma}}{G} + \frac{\sigma}{\eta}\ . \tag{B.1.11}$$

We wish to generalize this equation to cases where elastic response is not necessarily Hookean but instead follows from an arbitrary power law potential

$$U(\gamma) = \frac{1}{\alpha}\,G\,|\gamma|^{\alpha}\ . \tag{B.1.12}$$

As in the standard Maxwell model, we assume the elements are in series. Thus shear stress in both elements is equal to net stress, σ, and strains are additive:

$$\dot{\gamma} = \dot{\gamma}_U + \dot{\gamma}_\eta \ . \tag{B.1.13}$$

The behavior of the liquid element is viscous so $\sigma = \dot{\gamma}_\eta \cdot \eta$ and

$$\dot{\gamma}_\eta = \sigma/\eta \ . \tag{B.1.14}$$

For the solid element, in place of the standard Hookean spring, we use stress from the potential in Equ. B.1.12:

$$\sigma = \frac{d}{d\gamma} U(\gamma_U) = G\,|\gamma_U|^{\alpha-1}\ \mathrm{sgn}\,(\gamma_U) \tag{B.1.15}$$

$$= G\,|\dot{\gamma}_U\,t|^{\alpha-1}\ \mathrm{sgn}\,(\dot{\gamma}_U\,t) \tag{B.1.16}$$

$$= G\,t^{\alpha-1}\,|\dot{\gamma}_U|^{\alpha-1}\ \mathrm{sgn}\,(\dot{\gamma}_U) \tag{B.1.17}$$

$$\dot{\sigma} = (\alpha-1)\,G\,t^{\alpha-2}\,|\dot{\gamma}_U|^{\alpha-1}\ \mathrm{sgn}\,(\dot{\gamma}_U) \tag{B.1.18}$$

where the $\mathrm{sgn}(x)$ function is 1 for positive x and -1 for negative x and we have made use of the fact that t is positive. Since everything on the right hand side of Equ. B.1.18 is always positive except $\mathrm{sgn}(\dot{\gamma}_U)$, $\mathrm{sgn}(\dot{\gamma}_U) = \mathrm{sgn}(\dot{\sigma})$, thus

$$\dot{\sigma} = (\alpha-1)\,G\,t^{\alpha-2}\,|\dot{\gamma}_U|^{\alpha-1}\ \mathrm{sgn}\,(\dot{\sigma}) \tag{B.1.19}$$

$$|\dot{\gamma}_U| = \left(\frac{\dot{\sigma}\ \mathrm{sgn}(\dot{\sigma})}{(\alpha-1)\,G\,t^{\alpha-2}}\right)^{\frac{1}{\alpha-1}} \tag{B.1.20}$$

$$\dot{\gamma}_U\ \mathrm{sgn}(\dot{\gamma}_U) = \left(\frac{|\dot{\sigma}|}{(\alpha-1)\,G\,t^{\alpha-2}}\right)^{\frac{1}{\alpha-1}} \tag{B.1.21}$$

$$\dot{\gamma}_U = \mathrm{sgn}(\dot{\sigma})\ \left(\frac{|\dot{\sigma}|}{(\alpha-1)\,G\,t^{\alpha-2}}\right)^{\frac{1}{\alpha-1}} \tag{B.1.22}$$

Putting everything together (i.e. plugging Equ. B.1.14 and Equ. B.1.22 into Equ. B.1.13), we obtain the general formula for the rheology of the Maxwell model where the solid element has power law potential with exponent α,

$$\dot{\gamma} = \mathrm{sgn}(\dot{\sigma}) \left(\frac{|\dot{\sigma}|}{(\alpha - 1)\, G\, t^{\alpha-2}} \right)^{\frac{1}{\alpha-1}} + \frac{\sigma}{\eta}. \tag{B.1.23}$$

B.1.3 Yield-stress Scaling Calculation with Arbitrary Power-law Potential

It's possible to generalize the calculation of the scaling of the static yield stress in Sect. B.1.1 to the case of a Maxwell-like model where the elastic element follows an arbitrary power law potential. Combining a Maxwell model generalized in this way (see Sect. B.1.2) with the stress-history dependence of viscosity from our model, we have:

$$\dot{\gamma} = \mathrm{sgn}(\dot{\sigma}) \left(\frac{|\dot{\sigma}|}{(\alpha - 1)\, G\, t^{\alpha-2}} \right)^{\frac{1}{\alpha-1}} + \frac{\sigma}{\eta} \tag{B.1.24a}$$

$$\frac{\dot{\eta}}{G} = a - r \left(\frac{\sigma}{G} \right)^2 \tag{B.1.24b}$$

where $\mathrm{sgn}(x)$ is 1 for $x > 0$ and -1 for $x < 0$.

The calculation of the peaks follows the procedure used for the harmonic case. We approximate stress at small time then use that to solve for an approximate viscosity at small time. We then assume these approximations hold up to the peak where $\dot{\sigma} = 0$ and solve Eq. B.1.24a for the time at the peak, t_y.

In the present case, instead of approximating the early stress as linear in time, we use the following form:

$$\sigma(t) \approx G\, \dot{\gamma}^{\alpha-1}\, t^{\alpha-1} \tag{B.1.25}$$

Plugging this back into B.1.24b gives a differential equation for η,

$$\dot{\eta}/G = a - r(\dot{\gamma}\,t)^{2\,(\alpha-1)} \tag{B.1.26a}$$

$$\eta(t)/G = a\,(t+T) + r\,\dot{\gamma}^{2\,(\alpha-1)}\,t^{2\,\alpha-1}/(2\,\alpha-1) \tag{B.1.26b}$$

where we have used $\eta(0) = G\,a\,T$ as derived in Equ. 3.5.3b.

We now look at behavior at the stress peak. Evaluating Equ. B.1.24a at the peak, $t = t_y$, where $\dot{\sigma}(t = t_y) = 0$ and using the approximation of η from Equ. B.1.26b,

$$\sigma(t_y) = \dot{\gamma}\,\eta(t_y) \tag{B.1.27a}$$

$$\tag{B.1.27b}$$

Plugging small-time solutions for $\sigma(t)$ (Eq. B.1.25) and $\eta(t)$ (Eq. B.1.26b) into this gives a relation for t_y,

$$T = -t_y + \frac{\dot{\gamma}^{\alpha-2}\,t_y^{\alpha-1}}{a} + \frac{r\,\dot{\gamma}^{2\,(\alpha+1)}\,t_y^{2\,\alpha-1}}{a(2\,\alpha-1)} \tag{B.1.28}$$

In the case where $\dot{\gamma}\,t_y$ and r are large, only the highest term in t_y contributes and we have

$$T \approx \frac{r\,\dot{\gamma}^{2\,(\alpha+1)}\,t_y^{2\,\alpha-1}}{a(2\,\alpha-1)} \tag{B.1.29a}$$

$$t_y \approx \left(\frac{a\,(2\,\alpha-1)\,T}{r\,\dot{\gamma}^{2\,(\alpha-1)}}\right)^{\frac{1}{2\,\alpha-1}} \tag{B.1.29b}$$

$$\gamma_y \approx \left(\frac{a\,(2\,\alpha-1)\,\dot{\gamma}\,T}{r}\right)^{\frac{1}{2\,\alpha-1}} \tag{B.1.29c}$$

$$\sigma_y \approx G\,\left(\frac{a\,(2\,\alpha-1)\,\dot{\gamma}\,T}{r}\right)^{\frac{\alpha-1}{2\,\alpha-1}} \tag{B.1.29d}$$

Where we have used $\gamma_y = \dot{\gamma}\,t_y$ and Equ. B.1.25. These scalings reduce to the cube-root power law when the potential is harmonic and give σ_y depending on $\dot{\gamma}\,T$ to

exponents of 3/8 for Hertzian, 2/5 for cubic and 3/7 for quartic potentials suggesting that higher-order elasticity terms may explain exponents from ~ 0.33 to ~ 0.43.

Interestingly, the reciprocal square root scaling of yield stress with yield time (see Equ. 3.5.13a),

$$\sigma_y \approx G \left(\frac{(2\,\alpha - 1)\,a\,T}{r\,t_y} \right)^{\frac{1}{2}} \tag{B.1.30a}$$

$$\gamma_y \approx \left(\frac{(2\,\alpha - 1)\,a\,T}{r\,t_y} \right)^{\frac{1}{2(\alpha-1)}} \quad , \tag{B.1.30b}$$

is independent of the degree, α, of the potential.

B.2 Numerical Solutions for Yielding of Solid

Fig. B.1 shows numerical solutions under constant strain rate conditions to the model of Nguyen et al. (they use fluidity, $f = G/\eta$) [62],

$$\dot{\gamma} = \frac{\dot{\sigma}}{G} + \frac{\sigma}{\eta} \tag{B.2.1a}$$

$$\frac{\dot{\eta}}{G} = a - r \left(\frac{\dot{\gamma}\,\eta}{G} \right)^2 \quad , \tag{B.2.1b}$$

and our model,

$$\dot{\gamma} = \frac{\dot{\sigma}}{G} + \frac{\sigma}{\eta} \tag{B.2.2a}$$

$$\frac{\dot{\eta}}{G} = a - r \left(\frac{\sigma}{G} \right)^2 + d \left(\frac{\dot{\sigma}}{G\,\dot{\gamma}} \right)^2 \quad , \tag{B.2.2b}$$

to which we've added a damping term for numerical reasons to prevent stiffness of the differential equation during the stress-collapse after the yield stress. Solutions plotted here use the small value of $d = 1 \times 10^{-6}$ and are not sensitive to its value, in fact the yield stress scaling figure is very little changed if d is increased to 1.

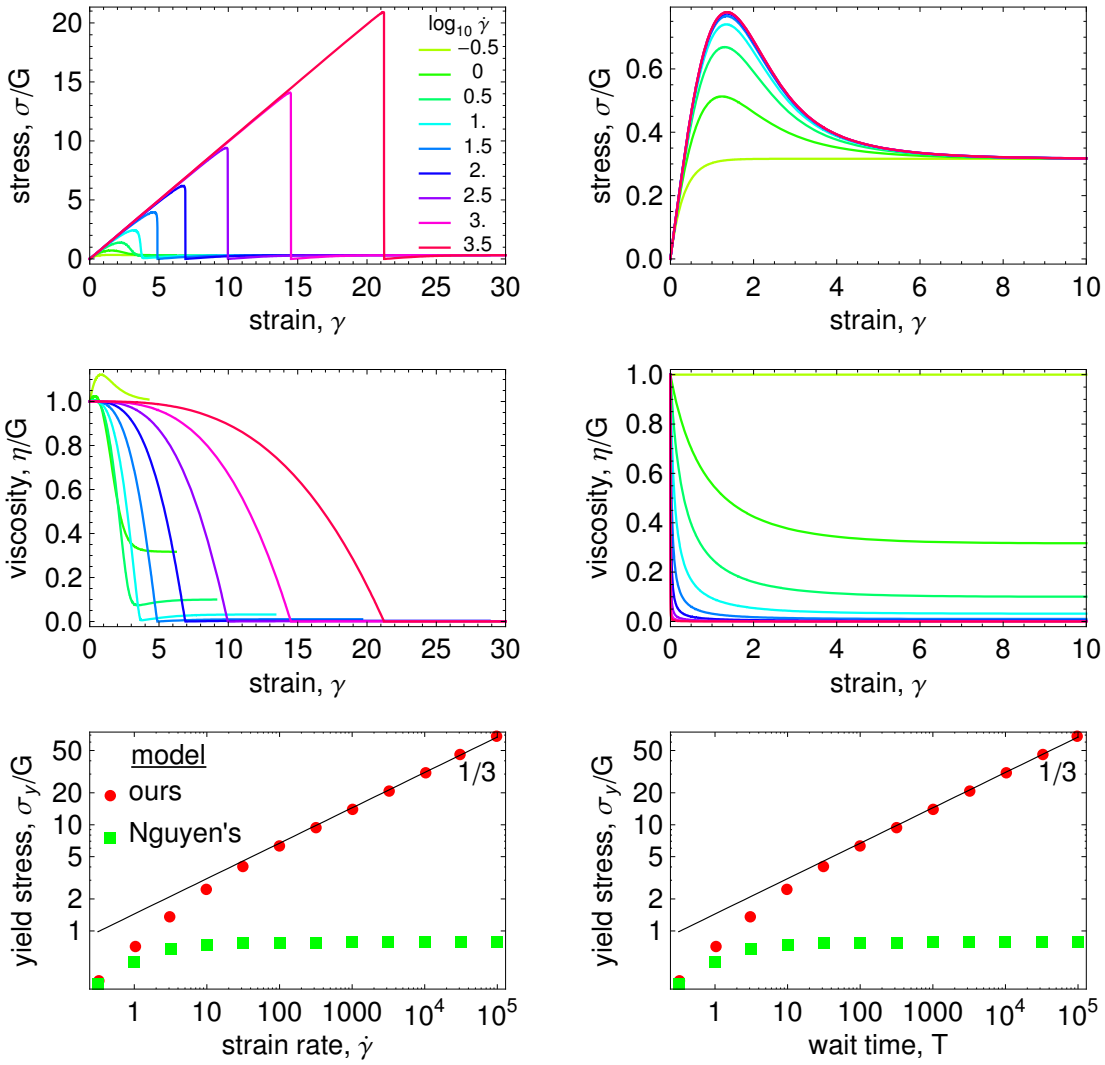

Figure B.1: Numerical solutions for our model (left column) and Nguyen et al.'s model [62] (right column). The top four figures show numerical solutions for different rates, $\dot{\gamma}$ and the bottom row shows numerical solutions for the scaling of the height of the stress maxima, σ_y, versus strain rate, $\dot{\gamma}$, for our model (red circles) and Nguyen et al.'s model (green squares). The values of the fixed parameters are $a = 0.1$, $r = G = 1$, $T = \dot{\gamma} = 10$, $d = 1 \times 10^{-6}$. The extreme similarity between the rate and age-scaling subfigures is not a mistake: in constant strain rate solutions of both models, the shape of stress-strain curves depend only on the product of $\dot{\gamma}\,T$. The numerical solutions to our model match the approximate scaling of Eq. 3.5.12c (black lines) when $\dot{\gamma}\,T$ is large.

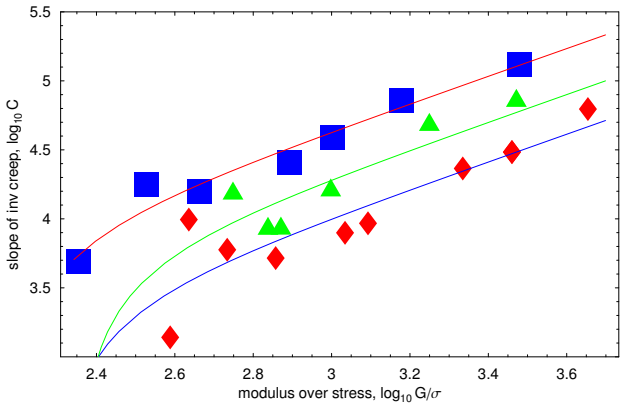

Figure B.2: This is data from Ref. [62] Fig.3b replotted an log-log axes. Series correspond to volume fraction of 0.60 (blue squares), 0.614 (green trianges), 0.623 (red diamonds). The fits are to the functional form $C = a\,G/\sigma + r\,\sigma/G$ with results $\{a = 10 \pm 2,\ r = 4 \cdot 10^5 \pm 6 \cdot 10^5\}$, $\{a = 20 \pm 6,\ r = 1 \cdot 10^6 \pm 3 \cdot 10^6\}$ and $\{a = 43 \pm 5,\ r = 10 \cdot 10^5 \pm 4 \cdot 10^5\}$.

The bottom row displays the scaling of the yield stress versus strain rate and wait time. When $\dot{\gamma}\,T$ is large, our model exhibits cube-root scaling in both $\dot{\gamma}$ and T and well matches the approximate solution given in Eq. 3.5.12c. Nguyen et al.'s model (Eq. B.2.1) however, does not exhibit similar scaling in this parameter regime, or any other that was investigated. It does not seem to be possible to separate values of a and r from data in reported in [62] (see Fig. B.2) so we are unable to show numerical solutions to the experimental regime.

APPENDIX C

STRUCTURE OF LOOSE PACKINGS

C.1 Numerical Solutions of Ornstein-Zernicke Equation

In Fig. C.1(B) we that even numerical solutions in two dimensions reproduce many of the features of $g(r)$ in the data including the gross shape of the peak at $r \approx 2\,d$, subsequent shortening of the period of oscillation and the growth of the more distant peaks with increasing volume fraction. We suspect the discrepancy in the locations of more distant peaks arises from the difference in dimensionality.

Numerical solutions of the Ornstein-Zernicke equation as described in Sect. 5.3.2 are computationally very expensive in three dimensions so we explore some of the properties in 2D. Fig. C.1(B) we that even numerical solutions in two dimensions reproduce many of the features of $g(r)$ in the data including the gross shape of the peak at $r \approx 2\,d$, subsequent shortening of the period of oscillation and the growth of the more distant peaks with increasing volume fraction. The discrepancy in the locations of more distant peaks appears to arise from the difference in dimensionality as the 3D solution captures the positions of the peaks (Fig. 5.9).

This OZ solution does not, however, appear to capture the splitting of the $r \approx 2\,d$ with increasing volume fraction suggesting that the $\sqrt{3}\,d$ cannot be explained as a consequence of sharp local features.

C.2 Monte-Carlo Simulation of Sphere and Contacts

To see determine whether local structure is determined solely by hard-sphere constraints and the number of neighbors, we perform Monte-Carlo simulations of the

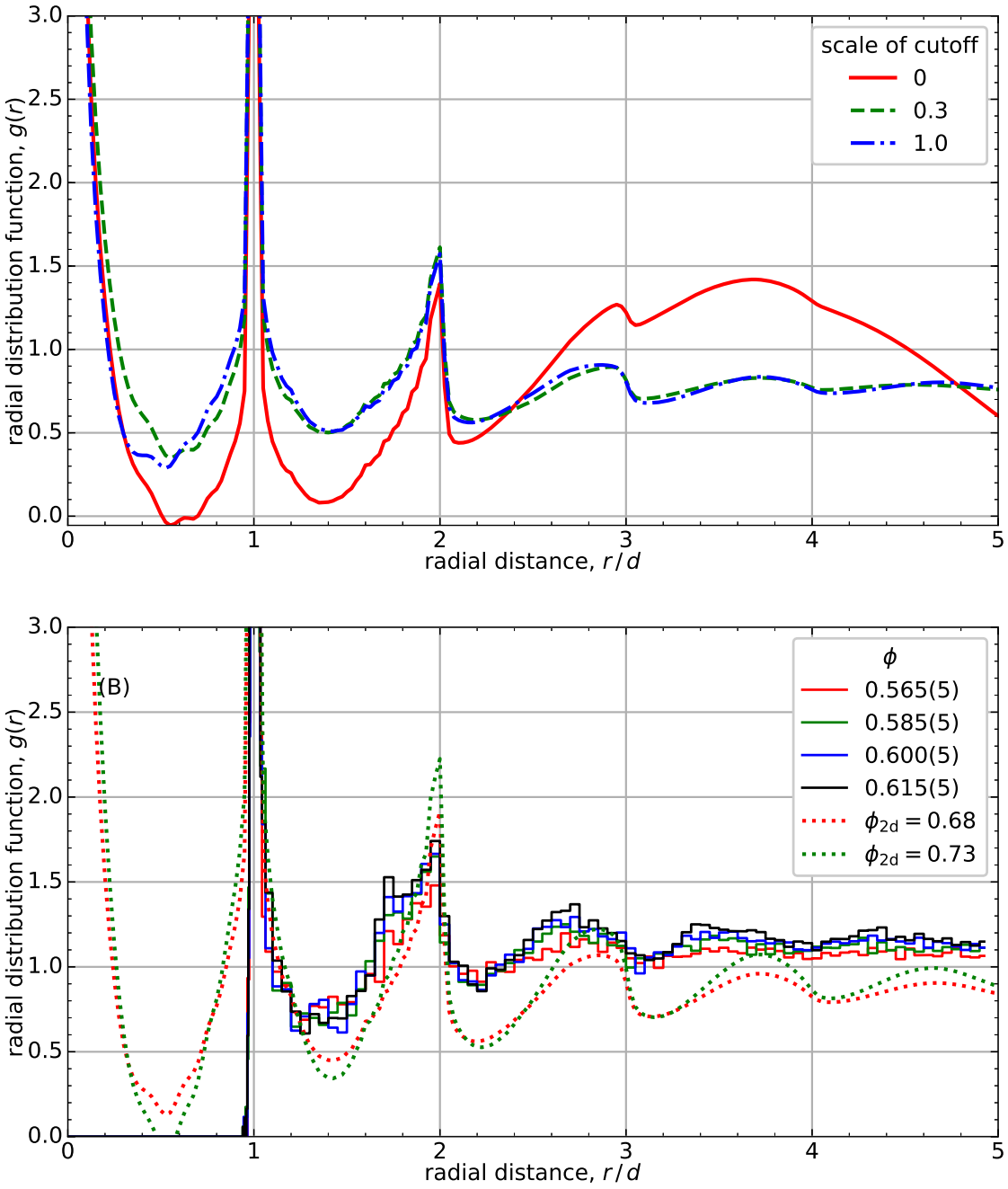

Figure C.1: Radial distribution data from our 3-dimensional experiment plotted alongside 2D numerical solutions of the Ornstein-Zernicke (OZ) equation assuming a direct correlation function that comes solely from the isostatic number of contacts. The numerical solutions are in 2D with $Z = 3$ and smoothing ($\sigma \approx 0.014\,d$) matching the value measured in the experiment. (A): The numerical solutions are not sensitive small changes in the cutoff frequency, however, a cutoff is necessary. (B): The 2D numerical solutions to the OZ equation (dashed curves) match many of the features of $g(r)$ in the data including the gross shape of the peak at $r \approx 2\,d$, growth of subsequent peaks with volume fraction and shortening of the period of oscillions although the predicted period is slighly too long.

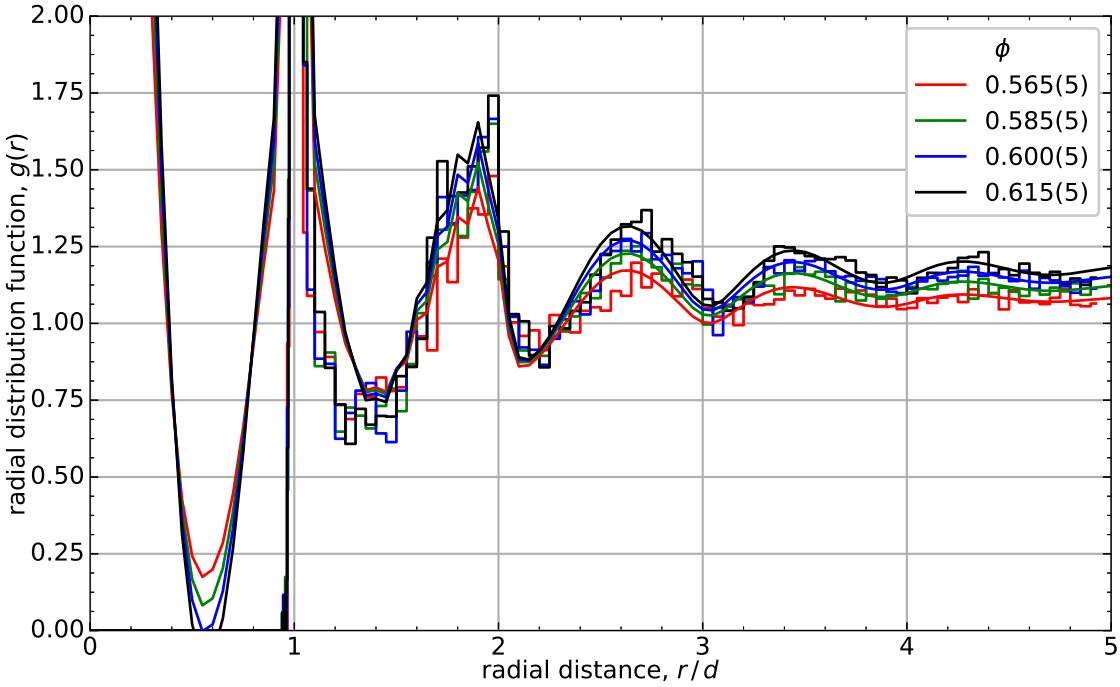

Figure C.2: Radial distribution function data (binned plots) and numerics (smooth): Numerics are 3D numerical solutions of the Ornstein-Zernicke (OZ) equation assuming a direct correlation function coming from the isostatic contact number at large friction, $Z = 4$, and the near miss distribution cut off at distance $1.1\,d$: The correspondence between the numerical solutions and $g(r)$ data is comparable to the numerics for $Z = 5$ in Fig. 5.9.

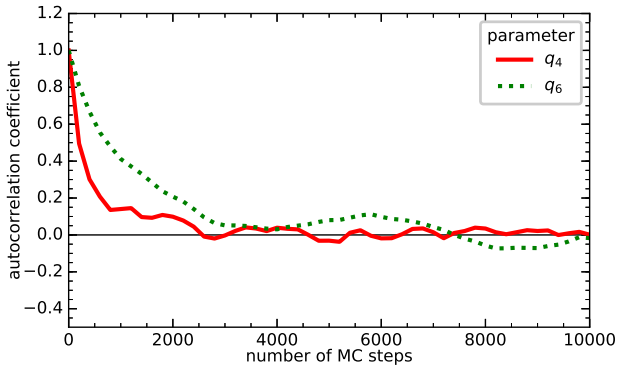

Figure C.3: Auto-correlation functions of at the most challenging particle number, $N = 11$, where the neighbor cloud is in a icosahedral shape with a single hole. The autocorrelation lengths of the q_n are of order 10^3 steps. We observe that the hole collapses and reforms somewhere else in the neighbor cloud after the order of 10^5 of these steps. Computations are all N are run for 5×10^5 steps to be certain states are being sampled in the Monte Carlo.

angular locations of N contacting particles. This problem we are simulating could be thought of as gas of hard circles with opening angle $\pi/3$ on the surface of the unit sphere. One can generate states with N particles in such a system in a completely sequentially independent way by generating N points on the unit sphere then rejecting those that violate the hard-sphere constraints. The rejection rate grows with N, however, making this algorithm inefficient by $N = 6$ and unworkable for $N > 7$. Instead we employ a Metropolis-style algorithm where the proposed states are generated by picking one of the spheres at random and proposing to shift it by a random distance (from a normal distribution with width $= 0.05$) in a random direction. The proposal is accepted if it does not overlap another sphere, otherwise it is rejected.

Initial states with N contacts are seeded by placing 12 spheres at the verticles of regular icosahedron then randomly removing $12 - N$ of them. One concern is that particularly for larger values of N, the system will stick in the neighborhood its initial state and the holes will always remain in the relative positions. We observe, however, that at $N = 11$ the hole collapses and reforms elsewhere in the course of $\approx 10^5$ of

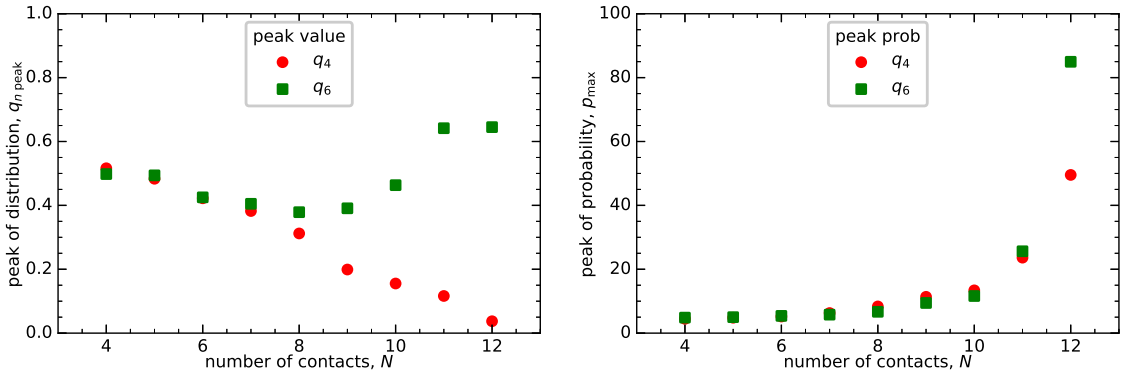

Figure C.4: Peaks of q_4 and q_6 distributions from Monte-Carlo at fixed N from Fig. 5.19 versus N. In (A) the distributions of q_4 and q_6 are seen to shift slowly downward together with increasing number of contacts, N, until about $N \approx 8$ where they split. This is Monte Carlo simulation of the angular positions of contacts subject only to hard-sphere constraints. It seems that above 8 contacts q_6 is beginning to pick up icosahedral order above $N \approx 8$.

these Monte-Carlo steps. This is much longer than autocorrelation time of the q_4 and q_6 cystalline order parameters that we measure (Fig. C.3) which is of order 10^3 steps. Surely collapse of the hole at $N = 11$ is the longest timescale we will encounter so we run all simulations for 5×10^5 to ensure averaging over even the longest timescale in the system.

Calculating the local bond-order parameters for the states generate by this Monte-Carlo simulation, we obtain a distribution for fixed N (Fig. 5.19) we compare directly to the experimental distributions of q_4 and q_6 and via weighted sampling over the measured number of neighbors (Fig. 5.20).

C.3 Divergence of Near-misses from Broken Contacts

A new simple hypothesis that explains the divergent distribution of near-misses is that the near misses are former contacts broken during the evolution of the packing. Cohesionless packings are always under pressure and cannot support tension so one might suppose that when contacts fail, they fail by sliding tangentially rather than

by pulling apart. If we assume that the distribution of the displacements of these tangential failures is broad, that is to say, that it is flat around the origin, then a near miss probability density of the following form follows

$$p(r) \sim (r-d)^{-1/2} \ . \tag{C.3.1}$$

To see this, let $d = 1$ and suppose that contacts break by sliding a distance, x, along the tangent plane at their point of contact. Let $p_x(x) = const$ be the flat probability distribution from which x is sampled. Let $p_r(r)$ be the unknown probability distribution of radial separations of pairs of spheres that have broken contact in this way. Since x is tangential to the original point of contact,

$$r = \sqrt{1+x^2} \approx 1 + \frac{1}{2}\,x^2 \ . \tag{C.3.2}$$

Solving this for x and taking a derivative that we will use later,

$$x \approx \sqrt{2}\,\sqrt{r-1} \tag{C.3.3}$$

$$\frac{dx}{dr} = \frac{\sqrt{2}}{2}\,(r-1)^{-1/2} \ . \tag{C.3.4}$$

Since x and r parameterize the same relative motion, their probability distributions must integrate to the same probability over a given interval:

$$\int_{x(r_1)}^{x(r_2)} p_x(x)\,dx = \int_{r_1}^{r_2} p_r(r)\,dr \tag{C.3.5}$$

and the probability distribution for radial separations follows:

$$p_x(x)\,dx = p_r(r)\,dr \tag{C.3.6}$$

$$p_r(r) = p_x(x)\,\frac{dx}{dr} \tag{C.3.7}$$

$$= \frac{\sqrt{2}}{2}\,p_x(x)\,(r-1)^{-1/2} \tag{C.3.8}$$

$$\sim (r-1)^{-1/2} \tag{C.3.9}$$

where we have made use of C.3.4 and the assumption that the $p_x(x)$ is constant.

BIBLIOGRAPHY

[1] Shlomo Alexander. Amorphous solids: their structure, lattice dynamics and elasticity. *Physics Reports*, 296(2-4):65 – 236, 1998. ISSN 0370-1573.

[2] SS Ashwin, Jerzy Blawzdziewicz, Corey S O'Hern, and Mark D Shattuck. Calculations of the structure of basin volumes for mechanically stable packings. *Phys. Rev. E*, 85(6):061307, 2012.

[3] T Aste. Variations around disordered close packing. *J. Phys. Condens. Matter*, 17(24):S2361, 2005.

[4] T. Aste, M. Saadatfar, A. Sakellariou, and T. J. Senden. Investigating the geometrical structure of disordered sphere packings. *Physica A*, 339(1-2):16 – 23, 2004. ISSN 0378-4371. Proceedings of the International Conference New Materials and Complexity.

[5] T. Aste, M. Saadatfar, and T. J. Senden. Geometrical structure of disordered sphere packings. *Phys. Rev. E*, 71(6):061302, Jun 2005.

[6] Phil Attard, Michael P Moody, and James WG Tyrrell. Nanobubbles: the big picture. *Physica A*, 314(1-4):696–705, 2002.

[7] P. Ballesta and G. Petekidis. Creep and aging of hard-sphere glasses under constant stress. *Phys. Rev. E*, 93:042613, Apr 2016.

[8] T. Baumberger, P. Berthoud, and C. Caroli. Physical analysis of the state- and rate-dependent friction law. ii. dynamic friction. *Phys. Rev. B*, 60:3928–3939, Aug 1999.

[9] J. D. Bernal. The bakerian lecture, 1962. the structure of liquids. *Proc. R. Soc. A*, 280(1382):299–322, 1964. ISSN 00804630.

[10] J D Bernal and J Mason. Packing of spheres: Co-ordination of randomly packed spheres. *Nature*, 188:910–911, 1960.

[11] John D Bernal. A geometrical approach to the structure of liquids. *Nature*, 183 (4655):141–147, 1959.

[12] P. Berthoud, T. Baumberger, C. G'Sell, and J.-M. Hiver. Physical analysis of the state-and rate-dependent friction law: Static friction. *Phys. Rev. B*, 59: 14313–14327, Jun 1999.

[13] Bram M. Borkent, Stephan M. Dammer, Holger Schönherr, G. Julius Vancso, and Detlef Lohse. Superstability of surface nanobubbles. *Phys. Rev. Lett.*, 98 (20):204502, 2007.

[14] Mehdi Bouzid, Martin Trulsson, Philippe Claudin, Eric Clément, and Bruno Andreotti. Nonlocal rheology of granular flows across yield conditions. *Phys. Rev. Lett.*, 111(23):238301, 2013.

[15] Lionel Bureau, Tristan Baumberger, Christiane Caroli, and Oliver Ronsin. Low-velocity friction between macroscopic solids. *C.R. Acad. Sci., Ser. IV: Phys.*, 2 (5):699 – 707, 2001.

[16] Philip Crosbie Carman. Fluid flow through granular beds. *Trans. Inst. Chem. Eng.*, 15:150–166, 1937.

[17] BM Carpenter, MJ Ikari, and C Marone. Laboratory observations of time-dependent frictional strengthening and stress relaxation in natural and synthetic fault gouges. *J. Geophys. Res. Solid Earth*, 121(2):1183–1201, 2016.

[18] Antonio Castellanos. Is there a lower bound for solid volume fraction in random loose packing of noncohesive rigid spheres? In *Proceedings of XL International Summer School–Conference APM*, Bolshoy pr. V.O., 61, St. Petersburg, 199178, Russia, 2012. Institute for Problems in Mechanical Engineering RAS.

[19] Patrick Charbonneau, Eric I Corwin, Giorgio Parisi, and Francesco Zamponi. Universal microstructure and mechanical stability of jammed packings. *Phys. Rev. Lett.*, 109(20):205501, 2012.

[20] Patrick Charbonneau, Jorge Kurchan, Giorgio Parisi, Pierfrancesco Urbani, and Francesco Zamponi. Glass and jamming transitions: From exact results to finite-dimensional descriptions. *Annu. Rev. Condens. Matter Phys.*, 8:265–288, 2017.

[21] Pinaki Chaudhuri, Ludovic Berthier, and Srikanth Sastry. Jamming transitions in amorphous packings of frictionless spheres occur over a continuous range of volume fractions. *Phys. Rev. Lett.*, 104(16):165701, Apr 2010.

[22] Massimo Pica Ciamarra and Antonio Coniglio. Random very loose packings. *Phys. Rev. Lett.*, 101(12):128001, 2008.

[23] Massimo Pica Ciamarra, Raffaele Pastore, Mario Nicodemi, and Antonio Coniglio. Jamming phase diagram for frictional particles. *Phys. Rev. E*, 84: 041308, Oct 2011.

[24] Massimo Pica Ciamarra, Patrick Richard, Matthias Schroter, and Brian P. Tighe. Statistical mechanics for static granular media: open questions. *Soft Matter*, 8: 9731–9737, 2012.

[25] Sylvain Courrech du Pont, Philippe Gondret, Bernard Perrin, and Marc Rabaud. Granular avalanches in fluids. *Phys. Rev. Lett.*, 90(4):044301, Jan 2003.

[26] Frédéric da Cruz, Sacha Emam, Michaël Prochnow, Jean-Noël Roux, and Fran çois Chevoir. Rheophysics of dense granular materials: Discrete simulation of plane shear flows. *Phys. Rev. E*, 72:021309, Aug 2005.

[27] Simon Dagois-Bohy, Brian P. Tighe, Johannes Simon, Silke Henkes, and Martin van Hecke. Soft-sphere packings at finite pressure but unstable to shear. *Phys. Rev. Lett.*, 109:095703, Aug 2012.

[28] Robert H Davis, Jean-Marc Serayssol, and EJ Hinch. The elastohydrodynamic collision of two spheres. *J. Fluid Mech.*, 163:479–497, 1986.

[29] JD Dent. The dynamic friction characteristics of a rapidly sheared granular material applied to the motion of snow avalanches. *ANN GLACIOL*, 18(1): 215–220, 1993.

[30] C Derec, A Ajdari, and F Lequeux. Rheology and aging: A simple approach. *Eur. Phys. J. E*, 4(3):355–361, MAR 2001. ISSN 1292-8941.

[31] Caroline Derec, Guylaine Ducouret, Armand Ajdari, and Fran çois Lequeux. Aging and nonlinear rheology in suspensions of polyethylene oxide˘protected silica particles. *Phys. Rev. E*, 67:061403, Jun 2003.

[32] Aleksandar Donev, Salvatore Torquato, and Frank H Stillinger. Pair correlation function characteristics of nearly jammed disordered and ordered hard-sphere packings. *Phys. Rev. E*, 71(1):011105, 2005.

[33] Aleksandar Donev, Robert Connelly, Frank H. Stillinger, and Salvatore Torquato. Underconstrained jammed packings of nonspherical hard particles: Ellipses and ellipsoids. *Phys. Rev. E*, 75(5):051304, May 2007.

[34] K. J. Dong, R. Y. Yang, R. P. Zou, and A. B. Yu. Role of interparticle forces in the formation of random loose packing. *Phys. Rev. Lett.*, 96(14):145505, 2006.

[35] S.F Edwards. The equations of stress in a granular material. *Physica A*, 249 (1-4):226 – 231, 1998. ISSN 0378-4371.

[36] Greg R. Farrell, K. Michael Martini, and Narayanan Menon. Loose packings of frictional spheres. *Soft Matter*, 6:2925–2930, 2010.

[37] L Fejes. Über die dichteste kugellagerung. *Mathematische Zeitschrift*, 48(1): 676–684, 1942.

[38] Guo-Jie Gao, Jerzy Bławzdziewicz, and Corey S. O'Hern. Frequency distribution of mechanically stable disk packings. *Phys. Rev. E*, 74(6):061304, Dec 2006.

[39] Guo-Jie Gao, Jerzy Blawzdziewicz, and Corey S. O'Hern. Geometrical families of mechanically stable granular packings. *Phys. Rev. E*, 80(6):061303, Dec 2009.

[40] Guo-Jie Gao, Jerzy Blawzdziewicz, Corey S. O'Hern, and Mark Shattuck. Experimental demonstration of nonuniform frequency distributions of granular packings. *Phys. Rev. E*, 80(6):061304, Dec 2009.

[41] P. Gondret, M. Lance, and L. Petit. Bouncing motion of spherical particles in fluids. *Phys. Fluids*, 14(2):643–652, 2002.

[42] TC Hales. A proof of the Kepler conjecture. *Annals of Mathematics*, 162:1065–1185, 2005.

[43] RR Hartley and RP Behringer. Logarithmic rate dependence of force networks in sheared granular materials. *Nature*, 421(6926):928–931, 2003.

[44] Takahiro Hatano. Rheology of a dense granular material. *J. Phys. Conf. Ser.*, 89(1):012015, 2007.

[45] Silke Henkes and Bulbul Chakraborty. Statistical mechanics framework for static granular matter. *Phys. Rev. E*, 79(6):061301, Jun 2009.

[46] Payman Jalali and Mo Li. An estimate of random close packing density in monodisperse hard spheres. *J. Chem. Phys.*, 120(2):1138–1139, 2004.

[47] H A Janssen. Experiments on corn pressure in silo cells. *Zeitschr. d. Vereines deutscher Ingenieure*, 39(1045), 1895.

[48] Melissa Jerkins, Matthias Schröter, Harry L. Swinney, Tim J. Senden, Mohammad Saadatfar, and Tomaso Aste. Onset of mechanical stability in random packings of frictional spheres. *Phys. Rev. Lett.*, 101(1):018301, Jul 2008.

[49] Randall D. Kamien and Andrea J. Liu. Why is random close packing reproducible? *Phys. Rev. Lett.*, 99(15):155501, Oct 2007.

[50] Stephen L Karner and Chris Marone. The effect of shear load on frictional healing in simulated fault gouge. *Geophys. Res. Lett.*, 25(24):4561–4564, 1998.

[51] M. G. Kleinhans, H. Markies, S. J. de Vet, A. C. in 't Veld, and F. N. Postema. Static and dynamic angles of repose in loose granular materials under reduced gravity. *J. Geophys. Res. Planets*, 116(E11):n/a–n/a, 2011. ISSN 2156-2202. E11004.

[52] Rémi Lespiat, Sylvie Cohen-Addad, and Reinhard Höhler. Jamming and flow of random-close-packed spherical bubbles: An analogy with granular materials. *Phys. Rev. Lett.*, 106(14):148302, 2011.

[53] Shir R. Liber, Shai Borohovich, Alexander V. Butenko, Andrew B. Schofield, and Eli Sloutskin. Dense colloidal fluids form denser amorphous sediments. *Proc. Natl. Acad. Sci. U.S.A. of the United States of America*, 110(15):5769–5773, 2013. ISSN 00278424.

[54] David R. Lide, editor. *CRC Handbook of chemistry and physics*. CRC Press, Boca Raton, 80 edition, 1999.

[55] W. Losert, J.-C. Géminard, S. Nasuno, and J. P. Gollub. Mechanisms for slow strengthening in granular materials. *Phys. Rev. E*, 61(4):4060–4068, Apr 2000.

[56] J C Macrae and W A Gray. Significance of the properties of materials in the packing of real spherical particles. *Br. J. Appl. Phys*, 12(4):164–172, 1961.

[57] A K Majumder and J P Barnwal. A computational method to predict particles free terminal settling velocity. *IE (I) Journal-M*, 85:17–19, 2004.

[58] G Mason. Radial distribution functions from small packings of spheres. *Nature*, 217(5130):733, 1968.

[59] James Clerk Maxwell et al. Iv. on the dynamical theory of gases. *Philos. Trans. Royal Soc.*, 157:49–88, 1867.

[60] J-F Métayer, Donald J Suntrup III, Charles Radin, Harry L Swinney, and Matthias Schröter. Shearing of frictional sphere packings. *Europhys. Lett.*, 93 (6):64003, 2011.

[61] David R. Nelson and B. I. Halperin. Dislocation-mediated melting in two dimensions. *Phys. Rev. B*, 19:2457–2484, Mar 1979.

[62] Van Bau Nguyen, Thierry Darnige, Ary Bruand, and Eric Clement. Creep and fluidity of a real granular packing near jamming. *Phys. Rev. Lett.*, 107:138303, Sep 2011.

[63] Edmund R. Nowak, James B. Knight, Eli Ben-Naim, Heinrich M. Jaeger, and Sidney R. Nagel. Density fluctuations in vibrated granular materials. *Phys. Rev. E*, 57(2):1971–1982, Feb 1998.

[64] Corey S. O'Hern, Stephen A. Langer, Andrea J. Liu, and Sidney R. Nagel. Random packings of frictionless particles. *Phys. Rev. Lett.*, 88(7):075507, Jan 2002.

[65] Corey S. OHern, Leonardo E. Silbert, Andrea J. Liu, and Sidney R. Nagel. Jamming at zero temperature and zero applied stress: The epitome of disorder. *Phys. Rev. E*, 68(1):011306, Jul 2003.

[66] R Ojha, N Menon, and DJ Durian. Hysteresis and packing in gas-fluidized beds. *Phys. Rev. E*, 62(3):4442, 2000.

[67] George Y. Onoda and Eric G. Liniger. Random loose packings of uniform spheres and the dilatancy onset. *Phys. Rev. Lett.*, 64(22):2727–2730, May 1990.

[68] Lo So Ornstein. Accidental deviations of density and opalescence at the critical point of a single substance. *Proc. Akad. Sci.*, 17:793, 1914.

[69] Guillaume Ovarlez, Evelyne Kolb, and Eric Clément. Rheology of a confined granular material. *Phys. Rev. E*, 64:060302, Nov 2001.

[70] JL Parker, PM Claesson, and P Attard. Bubbles, cavities, and the long-ranged attraction between hydrophobic surfaces. *J. Phys. Chem.*, 98(34):8468–8480, Aug 25 1994. ISSN 0022-3654.

[71] Jerome K Percus and George J Yevick. Analysis of classical statistical mechanics by means of collective coordinates. *Phys. Rev.*, 110(1):1, 1958.

[72] J.C. Lopera Perez, C.Y. Kwok, C. O'Sullivan, X. Huang, and K.J. Hanley. Assessing the quasi-static conditions for shearing in granular media within the critical state soil mechanics framework. *SOILS FOUND*, 56(1):152 – 159, 2016. ISSN 0038-0806.

[73] Pierre-Emmanuel Peyneau and Jean-Noël Roux. Frictionless bead packs have macroscopic friction, but no dilatancy. *Phys. Rev. E*, 78:011307, Jul 2008.

[74] Sham Ravindranath and Shi-Qing Wang. Universal scaling characteristics of stress overshoot in startup shear of entangled polymer solutions. *J. Rheol.*, 52 (3):681–695, 2008.

[75] Osborne Reynolds. Lvii. on the dilatancy of media composed of rigid particles in contact. with experimental illustrations. *Philos. Mag.*, 20(127):469–481, 1885.

[76] J. R. Rice and A. L. Ruina. Stability of steady frictional slipping. *J. Appl. Mech.*, 50:343–349, 1983.

[77] R Rutgers. Packing of spheres. *Nature*, 193:465–466, 1962.

[78] Carl F. Schreck, Thibault Bertrand, Corey S. O'Hern, and M. D. Shattuck. Repulsive contact interactions make jammed particulate systems inherently nonharmonic. *Phys. Rev. Lett.*, 107:078301, Aug 2011.

[79] Carl F. Schreck, Robert S. Hoy, Mark D. Shattuck, and Corey S. O'Hern. Particle-scale reversibility in athermal particulate media below jamming. *Phys. Rev. E*, 88:052205, Nov 2013.

[80] Matthias Schröter, Sibylle Nägle, Charles Radin, and Harry L. Swinney. Phase transition in a static granular system. *Europhys. Lett.*, 78(4):44004, 2007.

[81] Schröter, Matthias. A local view on the role of friction and shape. *EPJ Web Conf.*, 140:01008, 2017.

[82] G D Scott. Packing of spheres: Packing of equal spheres. *Nature*, 188:908–909, 1960.

[83] G D Scott and D M Kilgour. The density of random close packing of spheres. *J. Phys. D: Appl. Phys.*, 2(6):863–866, 1969.

[84] G David Scott. Radial distribution of the random close packing of equal spheres. *Nature*, 194:956–957, 1962.

[85] Leonardo E. Silbert. Jamming of frictional spheres and random loose packing. *Soft Matter*, 6:2918–2924, 2010.

[86] Leonardo E. Silbert, Deniz Ertaş, Gary S. Grest, Thomas C. Halsey, and Dov Levine. Geometry of frictionless and frictional sphere packings. *Phys. Rev. E*, 65(3):031304, Feb 2002.

[87] Chaoming Song, Ping Wang, and Hernán A Makse. A phase diagram for jammed matter. *Nature*, 453(7195):629, 2008.

[88] Paul J. Steinhardt, David R. Nelson, and Marco Ronchetti. Bond-orientational order in liquids and glasses. *Phys. Rev. B*, 28(2):784–805, Jul 1983.

[89] D Weaire T Aste. *The Pursuit of Perfect Packing*. CRC Press, Taylor & Francis, Boca Raton, FL, 80 edition, 2008.

[90] S. Torquato, T. M. Truskett, and P. G. Debenedetti. Is random close packing of spheres well defined? *Phys. Rev. Lett.*, 84(10):2064–2067, Mar 2000.

[91] Sonia Utermann, Philipp Aurin, Markus Benderoth, Cornelius Fischer, and Matthias Schröter. Tailoring the frictional properties of granular media. *Phys. Rev. E*, 84:031306, Sep 2011.

[92] D. A. Weitz and M. Oliveria. Fractal structures formed by kinetic aggregation of aqueous gold colloids. *Phys. Rev. Lett.*, 52(16):1433–1436, Apr 1984.

[93] MS Wertheim. Exact solution of the percus-yevick integral equation for hard spheres. *Phys. Rev. Lett.*, 10(8):321, 1963.

[94] Ning Xu and Corey S. O'Hern. Measurements of the yield stress in frictionless granular systems. *Phys. Rev. E*, 73(6):061303, Jun 2006.

[95] Ning Xu, Jerzy Blawzdziewicz, and Corey S. O'Hern. Random close packing revisited: Ways to pack frictionless disks. *Phys. Rev. E*, 71(6):061306, Jun 2005.

[96] Zhiping Yang, H. P. Zhang, and M. Marder. Dynamics of static friction between steel and silicon. *Proc. Natl. Acad. Sci. U.S.A.*, 105(36):13264–13268, 2008.

[97] Z. P. Zhang, L. F. Liu, Y. D. Yuan, and A. B. Yu. A simulation study of the effects of dynamic variables on the packing of spheres. *Powder Technol.*, 116(1): 23 – 32, 2001. ISSN 0032-5910.